The Dissertation Committee for Justin Thomas Harris Certifies that this is the approved version of the following dissertation:

Nanostructuring Silicon and Germanium for High Capacity Anodes in Lithium Ion Batteries

Committee:

Brian A. Korgel, Supervisor

John G. Ekerdt

Gyeong S. Hwang

C. Buddie Mullins

Keith A. Stevenson

Nanostructuring Silicon and Germanium for High Capacity Anodes in Lithium Ion Batteries

by

Justin Thomas Harris, B.S. Chemistry; B.S Chem Eng

Dissertation

Presented to the Faculty of the Graduate School of

The University of Texas at Austin

in Partial Fulfillment

of the Requirements

for the Degree of

Doctor of Philosophy

The University of Texas at Austin

December 2012

Dedication

Dedicated to my always supportive parents and my loving fiancée

Acknowledgements

After filling 22 years of my life with school, I can not believe this is finally the end; it all culminates with this. Though I wish I could mention everyone who has touched my life along the way, I would like to focus on those who have helped make these past 5 years at UT Austin a success.

First, I would like to thank all my fellow group members, past and present, for providing an open, collaborative, and entertaining research environment. Specifically, thanks to Andrew Heitsch for all the help and guidance he gave me when I first joined the group; everything I know about nanocrystal synthesis started with him. Also, much thanks to Aaron Chockla for our many collaborations, discussions, and debates as the lone pioneers into lithium ion batteries within our group. Special thanks to Timothy Bogart, Chet Steinhagen, Colin Hessel, and Vince Holmberg; without them the lab would have been a much duller place. Thanks to Matt Panthani, Vahid Akhavan, Danielle Smith, Reken Patel, Kate Shipman, Jackson Stolle, Taylor Harvey, Mike Rasch, Xiaotang Lu, and Yixuan Yu for always being available for discussion or to lend a helping hand. Also, I would like to thank the Stevenson Group, specifically Sankaran Murugesan and Kjell Schroder, for our collaborations and the hours you spent keeping Raman running.

Speaking of instrumentation, I would like to thank the many unsung heroes that keep the labs running; Dr. J.P. Zhou on the HRTEM, Dr. Dwight Romanovicz on TEM/SEM, Dr. Vince Lynch on XRD, and all of the Chemical Engineering Department staff. Without all of you our labs would grind to a halt.

Neverending thanks to Dr. Brian Korgel for accepting me into his group and guiding my research along the way. His passion for science and unending knowledge

were crucial to my success. None of this would be possible without him. Likewise, thank you to Dr. Keith Stevenson; our EFRC meetings and collaborations truly helped me look at problems with a multidisciplinary approach. Thank you to Dr. Buddie Mullins for allowing me access to his lab space before we had battery equipment of our own and for letting me participate in battery subgroup discussions; without that assistance my progress would have certainly slowed. Deepest gratitude to Dr. Gyeong Hwang and Dr. John Ekerdt for offering their time and insight by serving on my committee.

Without my friends here in Austin, I do not know that I would have made it to the end; Douglas French, James Carmer, Peter Frailie, James Knight, Robert Tsai, and Aimie Faucett made the good times great and the tough times seem a lot easier. To all my friends from the world of kickball, thank you for making Thursdays the best night of the week.

Finally, I thank my wonderful fiancée, Liz Gruenwald, for always being by my side and keeping my priorities in line Your love and encouragement have made these last 2 years a breeze. Last, but certainly not least, I thank my parents, Jeff and Debbie Harris, and my brother, Morgan Harris, for making me into the man I am today. They have always been there to lift up and encourage me when I am down or knock me back down a notch if I get out of line. They taught me that competition is never a bad thing and that you should never be too scared of losing to try. They always pushed me to push myself, and I owe everything I have achieved to them.

Nanostructuring Silicon and Germanium for High Capacity Anodes in Lithium Ion Batteries

Justin Thomas Harris, Ph.D.

The University of Texas at Austin, 2012

Supervisor: Brian A. Korgel

Colloidally synthesized silicon (Si) and germanium (Ge) were explored as high capacity anode materials in lithium ion batteries. a-Si:H particles were synthesized through the thermal decomposition of trisilane in supercritical n-hexane. Precise control over particle size and hydrogen content was demonstrated. Particles ranged in size from 240-1500 nm with hydrogen contents from 10-60 atomic%. Particles with low hydrogen content had some degree of local ordering and were easily crystallized during Raman spectroscopy. The as-synthesized particles did not perform well as an anode material due to low conductivity. Increasing surface conductivity led to enhanced lithiation potential.

Cu nanoparticles were deposited on the surface of the a-Si:H particles through a hydrogen facilitated reduction of Cu salts. The resulting Cu coated particles had a lithiation capacity seven times that of pristine a-Si:H particles. Monophenylsilane (MPS) grown Si nanowire paper was annealed under forming gas to reduce a polyphenylsilane shell into conductive carbon. The resulting paper required no binder or carbon additive and achieved capacities of 804 mA h/g vs 8 mA h/g for unannealed wires.

Si and Ge heterostructures were explored to take advantage of the higher inherent conductivity of Ge. Ge nanowires were successfully coated with a-Si by thermal

decomposition of trisilane on their surface, forming Ge@a-Si core shell structures. The capacity increased with increasing Si loading. The peak lithiation capacity was 1850 mA h/g after 20 cycles – higher than the theoretical capacity of pure Ge. MPS additives created a thin amorphous shell on the wire surfaces. By incubating the wires after MPS addition the shell was partially reduced, conductivity increased, and a 75% increase in lithiation capacity was observed for the nanowire paper.

The syntheses of Bi and Au nanoparticles were also explored. Highly monodisperse Bi nanocrystals were produced with size control from 6-18 nm. The Bi was utilized as seeds for the SLS synthesis of Ge nanorods and copper indium diselenide (CuInSe$_2$) nanowires. Sub 2 nm Au nanocrystals were synthesized. A SQUID magnetometer probed their magnetic behavior. Though bulk Au is diamagnetic, the Au particles were paramagnetic. Magnetic susceptibility increased with decreasing particle diameter.

Table of Contents

List of Tables

List of Figures

List of Illustrations

Chapter 1: Introduction

Nanomaterials have been used for millennia, largely unchanged, even if the people using them had no idea what gave them their unique properties.[1,2] Over the past few decades, everything changed. Technological advancements in materials characterization at the nanoscale, such as electron microscopy, have given a more complete picture of nanomaterials. Numerous synthetic techniques have been developed that produce monodisperse nanoscale materials in a controllable, tunable, and most importantly reproducible manner. This can be accomplished by two separate approaches: top-down and bottom-up. Top-down, the approach currently employed in the semiconductor industry, utilizes tools to machine device features of desired size and location into bulk materials.[3] As smaller feature sizes are required, the precision required increases and thus the cost of the tools increases exponentially. Bottom-up, on the other hand, builds device features by using nanoscale building blocks and assembling them into desired formations. A cheap, scalable method of creating these building blocks is colloidal synthesis.

Colloidal, or solution-based, synthetic methods have been reported for numerous inorganic compounds.[4-7] Colloidal synthesis is highly tunable. Size, shape, composition, and crystallinity of the desired product can be targeted based on adjustments in the synthetic methodology.[8,9] This is important because nanomaterials often display size or shape dependent magnetic, optical, and electronic properties different than those of their bulk or molecular counterparts.[10-13] Similarly, their small size allows nanomaterials to undergo significantly more stress and strain than bulk materials without fracturing. This dissertation focuses on controlling the growth and structure of colloidally grown nanomaterials to tune their properties for maximum benefit in device structures.

1.1 NANOSTRUCTURING SILICON AND GERMANIUM

1.2.1 Amorphous Silicon

Hydrogenated amorphous silicon (a-Si:H) has a wide variety of uses, including memory switching devices,[14,15] light-emitting diodes,[16] thin film transistors,[17] and solar cells.[18] For these applications, layers of a-Si:H are usually vapor-deposited on substrates. A number of other applications, including hydrogen fuel cells and lithium ion batteries, would benefit from the availability of large quantities of a-Si particles. Though c-Si has a higher long-range conductivity and faster Li-ion insertion than a-Si, a-Si has potential advantages as Li-ion battery anodes for a number of reasons. a-Si has shorter Li-ion diffusion lengths, smaller charge transfer resistance, and a predicted smaller and more isotropic volume expansion than c-Si.[19] Further, the electrochemical lithiation/delithiation cycles amorphize c-Si after a few cycles. Once this amorphous phase is established, further capacity loss is low because additional pulverization is minimal.[20] The aforementioned CVD grown thin films exploit these attributes for high capacities and high cyclability.[21-23] a-Si also lithiates at a higher voltage than c-Si. Using this knowledge, Cui, et al found that c-Si nanowires coated with a-Si have capacities above 1000 mA h/g with 90% retention over 100 cycles when cycled in such a way to only lithiate the a-Si shell while leaving the core intact.[19,24]. These processes are all expensive, difficult to scale up, and require modified electrochemical cycling to maintain structural integrity.

The Korgel group specializes in synthesis of large quantities of colloidal nanostructures. A few years ago, we demonstrated the synthesis of colloidal a-Si particles by decomposition of trisilane (Si_3H_8) in supercritical n-hexane (sc-hexane) at high

temperature.[25,26] By pressurizing the solvent above its critical point, colloidal solution-phase particle synthesis can be carried out at relatively high temperature. The particles are spherical, relatively monodisperse, and easily dispersed in organic solvents. These particles can be used as anodes for LIBs, but have displayed lower capacities than anticipated due to low particle-to-particle conductivities. By modifying the surface of the particles conductivity can be increased, thereby increasing lithiation capacity.

1.2.2 Semiconductor Nanowires

Nanostructures come in many shapes and forms. At the most basic level, the structures can be separated by their level of quantum confinement and dimensionality. 2-D structures, such as thin films or platelets, are only confined in one direction. 0-D structures, or quantum dots, are quantum confined in all directions. 1-D structures, such as nanowires and nanorods, are confined in two directions and only have freedom on one axis. These structures have been known to exist for centuries,[27] but it was not until the 1950s that researchers began to understand the fundamental mechanisms responsible for their formation though initially only studied at the micrometer level. These mechanisms still apply at the nanoscale: (1) strain-driven wire growth from surfaces;[28] (2) whisker crystallization from the vapor or liquid phase induced by axial screw dislocations;[29,30] and (3) precipitation from a metal seed particle.[31,32] The third mechanism, seeded growth, creates highly reproducible single-crystalline nanowires. Semiconductor nanowires in particular are interesting due to their long lengths and high aspect ratios.[33,34] This trait makes them prime candidates to replace traditional, top-down designed lithographically defined nanostructures. Their value as photodetectors, memory devices, and logic gates has previously been demonstrated;[33,35,36] the added benefit of flexibility allows for devices to be made on cheap, flexible substrates for niche applications such as the

3

backplanes of flexible displays.[37] For these applications, single nanowires are all that are required for proof of principle. Nanowires can be incorporated into polymers, fabrics, or dropcast into self-supporting meshes and used as absorber layers for photovoltaics, scaffolds for catalytic particles, or as anodes for lithium ion batteries.[38,39] For these applications, large quantities of high quality material are necessary for any potential commercialization.

1.2.2.1 Seeded Growth of Nanowires

Vapor-liquid-solid (VLS) growth of nanowires from metallic seeds was first proposed by Wagner *et al.*[31] In their work, a substrate was coated with a thin film of Au. Si was then deposited by chemical vapor deposition (CVD) onto the substrate at high temperatures. The Si preferentially dissolves into the Au, forming Au:Si alloy droplets at temperatures above their eutectic point. When the Au:Si liquid droplet saturates, the solid crystalline Si precipitates and forms a single-crystalline wire. Figure 1.1 shows a schematic of the nanowire growth mechanism. In region I, Si diffuses into Au forming an equilibrium between solid Au and liquid Au:Si alloy. After enough Si is dissolved, the Au:Si alloy becomes completely liquid (region II). As excess Si dissolves, solid Si precipitates out forming an equilibrium between liquid Au:Si alloy and the solid Si nanowire.
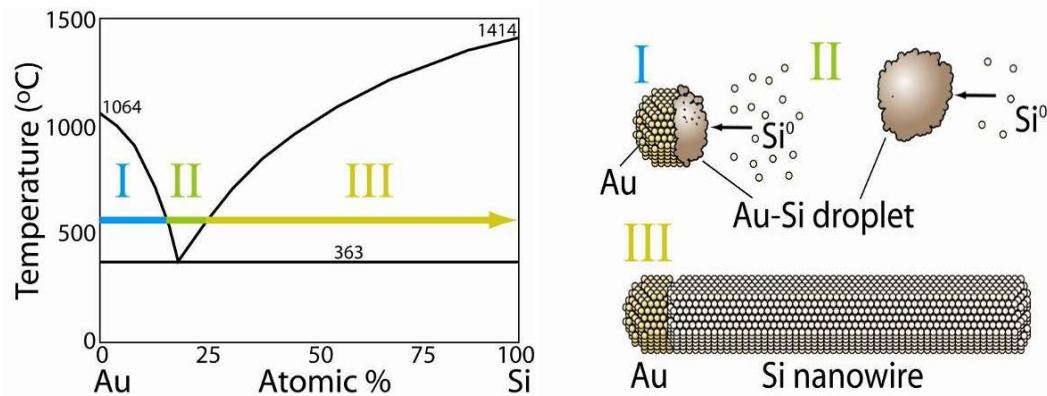
Figure 1.1: Nanowire growth mechanism.[40] The arrow tracks the composition change as Si is added to Au. Schematics of the nanowires at various points during growth are shown (regions I, II, and III)

This method has been improved upon over the years by combining CVD with size-monodisperse Au nanoparticles attached to a surface, and VLS growth is now the best method for producing nanowires of the highest quality and consistency. It can also be applied to a wide variety of metal-semiconductor systems. Unfortunately, VLS requires a substrate for growth and is not a scalable process, severely limiting the potential throughput. Buhro *et al* discovered that this process could be modified to run in the solution phase, via solution-liquid-solid (SLS) growth, to synthesize III-V semiconductor nanowires using low melting point metals or semimetals such as indium and bismuth.[43]
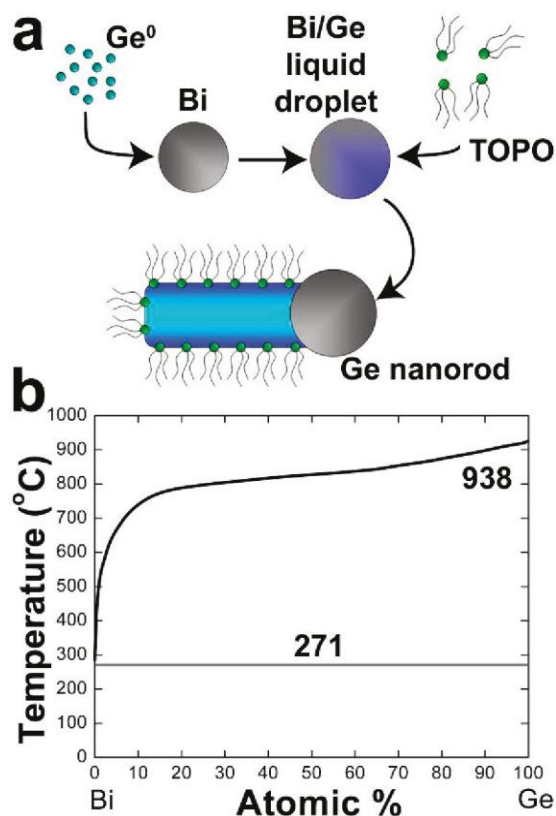
Figure 1.2: (a) Illustration of the Ge nanorod growth process and (b) the Ge/Bi phase diagram. The polymer coating that surrounds the Bi nanocrystals is not shown.[41]

The SLS mechanism for Ge nanorod growth, as illustrated in Figure 1.2, proceeds because Bi forms a eutectic with Ge at relatively low temperature, below the boiling point of the solvent yet high enough to decompose the reactant.[42] There are obvious advantages to performing reactions in the solution phase. The process is fully scalable, performed at ambient pressure and relatively low temperature, and allows for in situ surface modification and passivation of the nanowires. However, SLS growth is limited by the boiling point of the solvent.

1.2.2.2 Supercritical Fluid – Liquid – Solid Growth

To access the higher temperatures necessary for the decomposition of some Si and Ge precursors, an alternate growth medium is required. A supercritical fluid is any material that is heated and pressurized above its critical temperature and pressure. As seen in Figure 1.3, at this point the material no longer has an equilibrium between two phases, but rather consists of only one phase. This phase combines the ability to diffuse like a gas with the ability to dissolve materials like a liquid with density, viscosity, and diffusivity intermediate between those of liquids and gases. Their high diffusivity and low viscosity provide a medium for fast reactions without stirring that would be transport limited in the liquid phase.[44] Hanrath *et al.* developed the supercritical fluid – liquid – solid (SFLS) method for Ge nanowires in 2002,[45,46] though the reaction mechanism is exactly the same as the SLS method. The only difference is reaction medium.
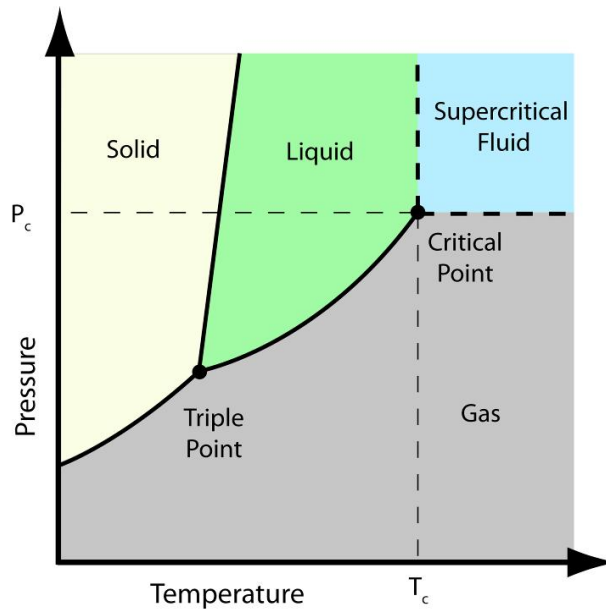
Figure 1.3: Generic equilibrium pressure-temperature phase diagram

1.2 LITHIUM ION BATTERIES

1.2.1 Lithium Ion Battery Basics

As the world's population continues to grow, we have a growing need for cheap, portable methods of energy storage and delivery. Most of these portable energy needs are met by lithium ion batteries. Lithium ion batteries offer one of the highest energy densities and longest lifetimes available, but there has been little improvement since they first hit the market in 1991.[47] Basically, all Li-ion batteries work by shuttling Li^+ between electrodes where they form Li-containing compounds. Figure 1.3 illustrates how this process works. The Li^+ ions are carried across a permeable membrane in an organic electrolyte solution, such as lithium phosphohexafluoride ($LiPF_6$) in diethylcarbonate. The principle was first proposed by Whittingham in 1976 using titanium (II) sulfide (TiS_2) as the cathode and a pure Li metal anode.[48] Goodenough then displayed a rechargeable Li-ion battery using a lithium cobalt oxide ($LiCoO_2$) cathode, a material still widely used today.[49,50] However, the pure Li metal anode posed safety concerns due to its high reactivity. Soon after, electrochemical intercalation of Li into graphite was demonstrated by a number of groups.[51-53] Using these much safer graphitic anodes and $LiCoO_2$ cathodes, the modern-day Li-ion battery was born.
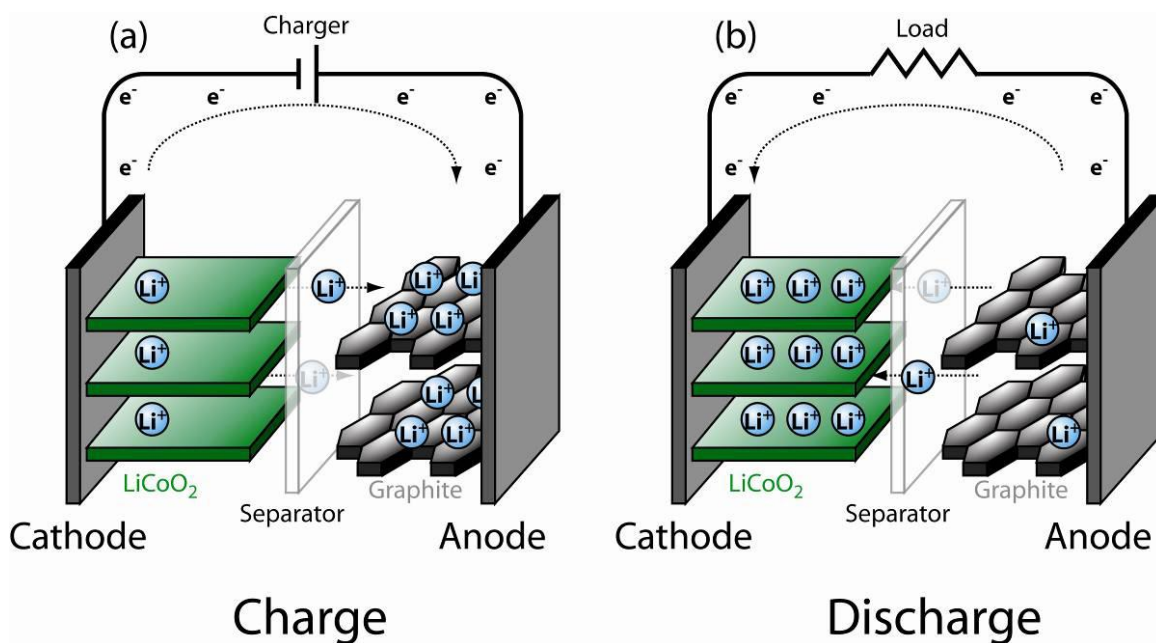
Figure 1.4: Schematic (a) charge and (b) discharge cycles for a Li-ion battery with a LiCoO$_2$ cathode and graphite anode.[40]

From laptops and cell phones to electric cars, there is always a drive for cheaper, lighter, smaller, longer lasting, more powerful, and faster charging batteries requiring more stable and higher capacity materials.[54] Capacity is directly related to the number of Li atoms that can intercalate into the active material. While carbon anodes are useful due to their high stability over repeated cycling, they can only accommodate one Li atom for every six C atoms (LiC$_6$), giving a maximum gravimetric capacity of 372 mA h/g.[55,56] Likewise, the maximum capacity of LiCoO$_2$ is only 274 mA h/g.[57] On the cathode side, there are several promising alternatives that offer moderate increases in capacity without sacrificing cyclability, including various other lithium metal oxides (e.g. LiMn$_2$O$_4$, LiNiO$_2$, LiV$_2$O$_5$), [58-62], lithium metal phosphates (e.g. LiFePO$_4$),[63] and even sulfur.[64] However, the largest potential capacity gains can be found on the anode side in lithium alloys.[65,66] Particularly, silicon (Si) and germanium (Ge) both form high capacity lithium

alloys at room temperature ($Li_{15}Si_4$, 3579 mA h/g[67-69] and $Li_{15}Ge_4$, 1624 mA h/g[70]), and both are abundant with a low working potential compared to Li[67,68,70]). Their limitations arise from a massive volume expansion of over 300% that causes pulverization of crystalline Si and Ge upon repeated lithiation/delithiation cycles, causing loss of electrical contact, irreversible capacity loss and eventually battery failure.[65,71] To overcome the pulverization problem, numerous approaches have been explored.

1.2.2 Nanostructured Materials for Lithium Ion Batteries

Nanostructuring has been shown to reduce these pulverization effects by accommodating higher degrees of strain. Nanotubes, nanorods, nanowires, nanocrystals, and thin films have all been explored with promising results. Si nanotubes grown using alumina templates have displayed capacities as high as 3247 mA h/g, but only 89% Coulombic efficiency.[72] Si and Ge nanocrystals display extremely high capacity retention over many cycles, but due to the need for an extensive conductive carbon matrix to maintain electrical contact their effective gravimetric capacity is limited.[73-75] Likewise, core-shell nanoarchitectures of Si over carbon show great cyclability but an unrealized maximum effective capacity.[71,76-79]. Thin films of both Si and Ge, grown by chemical vapor deposition (CVD), have capacities near their respective theoretical maxima with negligible capacity fade over hundreds of lithiation/delithiation cycles.[80-85] However, they are extremely expensive and could not be practically scaled for commercialization. Similarly, CVD and vapor-liquid-solid (VLS) grown nanowires have shown promise;[86-89] Cui, et al even achieved a capacity of 2725 mA h/g with good stability, retaining 1400 mA h/g after 700 cycles.[83] Again, these have problems with scalability due to their CVD roots. By utilizing solution and supercritical fluid based processes for Si and Ge nanostructure growth, such as solution-liquid-solid (SLS) and supercritical fluid-liquid-

solid (SFLS) growth, large quantities of nanowires, nanorods, or nanoparticles can be produced at relatively low cost.[90-95]

1.2.3 Silicon vs Germanium

Though Li-Ge and Li-Si alloys have both been explored since the 60s and 70s, only Si has garnered much attention as a LIB anode until recently. Si and Ge both offer unique properties as anode materials. Si has a much higher theoretical gravimetric capacity – 3579 mA h/g vs 1624 mA h/g – but nearly identical volumetric capacities. Though Ge is more expensive of the two materials, it has many attractive attributes. Si expands anisotropically upon lithiation, while Ge expands isotropically.[70] This leads to reduced strain and pulverization. Ge has a higher intrinsic conductivity than Si, and a Li diffusion coefficient 400 times that of Si.[96] This allows Ge to perform better at higher current densities making it attractive for high power situations.[97] By creating Si-Ge heterostructures, potentially the best of both materials can be realized. The Ge can provide a more robust, more conductive, and faster lithiating matrix for Si, while the Si can boost the overall capacity of the Si-Ge nanostructure. These nanostructures provide an avenue for exciting research and potential far-reaching improvements to Li-ion batteries.

1.3 MAGNETIC PROPERTIES OF NANOCRYSTALS

Nanostructured magnetic materials display remarkable size-dependent properties and have potential use in novel applications.[98] This is due to the isolation and synthesis of materials with single ferromagnetic domains less than 5 nm in diameter, ferromagnetic interfacial phenomena, and superparamagnetic materials. Nanometer sized magnetic materials have been integrated into numerous technologies, including magnetic separations, giant magnetoresistance, spin-dependent electron transport valves, high

density digital information storage, and even magnetic resonance imaging (MRI) contrast agents.[99,100] Though these usually utilize bulk magnetic materials that are nanostructured, research has revealed that some bulk diamagnetic noble metals display unusual ferromagnetic and paramagnetic effects at small diameters.

1.3.1 Emergence of Magnetism in Noble Metal Nanocrystals

Very small noble metal nanocrystals, less than 2 to 3 nm in diameter, have been shown in some instances to exhibit fundamentally different magnetic properties than in bulk form. Bulk Au is diamagnetic, but at the nanoscale has been shown to be ferromagnetic[101] or paramagnetic.[102] Pt and Pd nanocrystals, which are paramagnetic in bulk, have also shown enhanced paramagnetic[103,104] or even ferromagnetic[105] properties. Although these magnetic effects are not completely understood at present two hypotheses regarding the origins of the magnetism have been put forth. The first hypothesis suggests that the magnetic atomic orbital contributions significantly influence the overall magnetic properties as the nanocrystal size decreases.[103-105] In this scenario, the atomic orbital contributions are sensitively dependent on the crystal symmetry, crystalline phase, nearest atomic neighbor, crystalline defects, and the number of atoms within the nanocrystal. The opposing hypothesis suggests the magnetism originates from the atomic spin contributions at the metal surface-ligand bonding site.[101,102,106-108] In this case the strong metal-ligand bonding induces a spin imbalance at the surface that causes the unusual magnetic effects.[109-112] This hypothesis is supported by the disappearance of the unusual magnetic properties when weaker binding ligands are adsorbed to a nanocrystal surface.[113-115] Due to the limited support for each of theses hypotheses, we studied the magnetic properties of < 2 nm diameter Au nanocrystals with strongly bound dodecanethiol ligands.

Due to the large surface to volume ratio of atoms in nanometer size materials, magnetism at surfaces and interfaces is extremely important. This leads to a shift in the spin and orbital contributions to the magnetic moment. Previous reports have shown that very small magnetic particles exhibit fundamentally different magnetic properties than their bulk counterparts.[109-115] For example, though bulk Au is diamagnetic, 2 nm dodecanethiol capped Au nanocrystals have been reported to exhibit ferromagnetism. This ferromagnetism is believed to result from spin-orbit coupling between the surface-bound thiol molecules and the gold surface atoms. As the gold nanoparticle size decreases and the surface area to volume ratio increases, the likelihood of ferromagnetism increases. The origin of this effect is still currently being debated, but it is noted that this effect is different than the superparamagnetic effect.

1.3.2 Magnetic Measurements of Nanocrystals

Magnetism in bulk materials is well-defined. Materials display diamagnetism, paramagnetism, ferromagnetism, antiferromagnetism, or ferrimagnetism. The picture changes at the nanoscale due to uncoupled atomic exchange interactions and surface effects. When the domain of a ferromagnetic nanocrystal is smaller than its bulk magnetic domain, superparamagnetism occurs.[116] Superparamagnetism is the result of thermal energy overcoming the magnetic exchange energy of a material. Since magnetic exchange energy is proportional to the volume of the magnetic domains, decreased particle size leads to decreased magnetic energy. At small enough domains, thermal energy disrupts the interaction between magnetic units. The nanomagnets are easily aligned by an applied magnetic field like a paramagnet with high magnetic susceptibility, but rather than displaying hysteresis indicative of ferromagnets the moment immediately returns to 0 when a field is removed.

Magnetic properties of nanomaterials are measured with high sensitivity by superconducting quantum interference devices (SQUID). SQUID utilize a Josephson junction, two superconducting loops connected by a thin insulator. With this setup, magnetic flux is quantized and the insulating barrier induces a phase shift dependent on the magnitude of the current. This critical current is extremely sensitive to magnetic flux, and the voltage drop is measured to determine the magnetic moment. In a DC SQUID, two Josephson junctions are utilized and magnetic moments down to 5 aT can be detected. Both externally applied magnetic fields and temperature may be varied to analyze how the studied magnetic material behaves related to the variables. Though extremely sensitive, ensembles of nanomaterials must be measured in the magnetometer.

Figure 1.5 illustrates measurements made on nanocrystal ensembles in a SQUID. Column 1 shows field-dependent sweeps and column 2 shows temperature-dependent sweeps. For field-dependent sweeps, the temperature is held constant while the external magnetic field, H, is varied and the resulting magnetization, M, is measured. For temperature-dependent sweeps, the external magnetic field, H, is held constant while temperature is varied and magnetization, M, is measured. For zero-field cooled (ZFC) sweeps, the sample is cooled before applying the magnetic field. For field cooled (FC) sweeps, the magnetic field is applied before cooling.
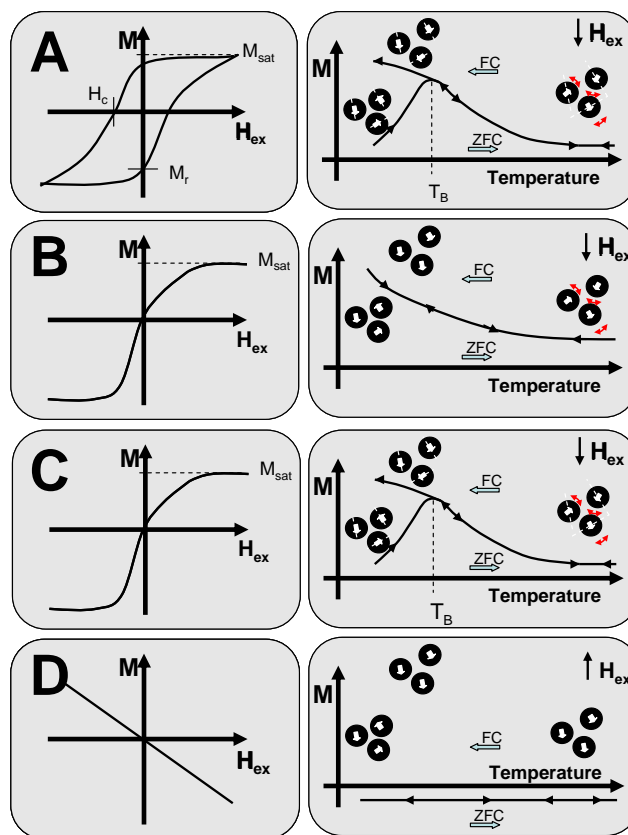
Figure 1.5: Illustration of (1st Column) field-dependent and (2nd Column) temperature-dependent magnetization sweeps in a SQUID for (A) ferromagnetic materials, (B) paramagnetic materials, (C) superparamagnetic materials, and (D) diamagnetic materials.

For ferromagnets, paramagnets, and superparamagnets there is a maximum magnetization that occurs, denoted as M_{sat}. This is the saturation magnetization, and it occurs when all the magnetic moments in individual nanocrystals are align in one direction. The difference in ferromagnets vs paramagnets and superparamagnets is that ferromagnets display hysteresis, and therefore remnant magnetization (H_r). This means that the magnetic domains remain partially aligned after being magnetized. In paramagnets and superparamagnets above the blocking temperature (T_b), thermal energy is enough rearrange spin states and prevent remnant magnetization. This removes all

hysteresis. The blocking temperature is the temperature at which the ZFC deviates from the FC. Above this temperature, thermal energy is enough to disrupt interaction between magnetic units and superparamagnets behave like paramagnets; below this temperature there is not enough thermal energy and they behave as ferromagnets.

1.4 DISSERTATION OUTLINE

Colloidal syntheses of nanostructures are presented throughout this dissertation. Chapters 2-4 all focus on the synthesis of various structures of Si and Ge and their potential applications as high capacity lithium ion battery anodes. Chapter 2 discusses the synthesis of a-Si:H particle colloids. The reaction parameter space was fully explored, and the effects of temperature, pressure, and initial trisilane concentration on the final product are presented. Hydrogen content and system is characterized by various techniques. Chapter 3 focuses on surface modification of Si nanostructures for increased conductivity; specifically, Cu-coating the a-Si:H nanoparticles and anneal studies on MPS grown Si nanowires are presented. Full characterization of these particles and their resulting improved behavior in lithium ion batteries are discussed. Chapter 4 focuses on a-Si coated Ge NWs and their improved capacity and cycle-life vs pure Ge and Si nanostructures.

In Chapters 5 and 6 other colloidal nanocrystals and their properties are explored. Chapter 5 discusses the synthesis of monodisperse Bi nanocrystals and the effect polymer concentration and precursor ratios on their growth. It also highlights seeded SLS growth processes to which the particles were applied. Chapter 6 discusses the synthesis of sub 2 nm Au nanocrystals and explores their magnetic properties. Finally, Chapter 7 summarizes the main conclusions of this dissertation and offers suggestion for future research works.

1.5 REFERENCES

(1)   Jose-Yacaman, M.; Rendon, L.; Arenas, J.; Serra Puche, M.C. *Science* **1996**, *273*, 223-225.

(2)   Ashby, M.F.; Schodek, D.L.; Ferreira, P.J.S.G. *Nanomaterials, Nanotechnologies, and Design*. Butterworth-Heinemann: 2009.

(3)   Gonsalves, A. *Intel 32 nm Processor Headed for Production* http://www.informationweek.com/news/hardware/processors/showArticle.jhtml?articleID=224400257&subSection=All+Stories (May 11, 2010)

(4)   Sun, S.H.; Murray, C.B. *J. Appl. Phys.* **1999**, *85*, 4325-4330.

(5)   Peng, Z.A.; Xi, P. *J of the Am. Chem. Soc.* **2001**, *123*, 1389-1395.

(6)   Peng, Z.A.; Peng, X.G. *J. of the Am. Chem. Soc.* **2002**, *124*, 3343-3353.

(7)   Korgel, B.A.; Monbouquette, H.G. *J. Phys. Chem.* **1996**, *100*, 346-351.

(8)   Shah, P.S.; Husain, S.; Johnston, K.P.; Korgel, B.A. *J. of Phys. Chem. B* **2001**, *105*, 9433.

(9)   Ozin, G.A.; Arsenault, A.C. *Nanochemistry: A Chemical Approach to Nanomaterials*; RSC Publishing, 2005

(10)   Murray, C.B.; Kagan, C.R.; Bawendi, M.G. *Annual Review of Materials Science* **2000**, *30*, Future.

(11)   El-Sayed, M.A. *Acc. Chem. Res.* **2001**, *34,* 257-264.

(12)   Sun, S.; Fullerton, E.E.; Weller, D.; Folks, L.; Moser, A. *Science* **2000**, *287*, 1989-1992.

(13)   Puntes, V.; Krishnan, K.M.; Alivisatos, A.P. *Science* **2001**, *291*, 2115-2117.

(14)   Lecomber, P. G.; Owen, A. E.; Spear, W. E.; Hajto, J.; Snell, A. J.; Choi, W. K.; Rose, M. J.; Reynolds, S. *J. Non-Cryst. Solids* **1985**, *77-8*, 1373-1382.

(15)   Owen, A. E.; Lecomber, P. G.; Spear, W. E.; Hajto, J. *J. Non-Cryst. Solids* **1983**, *59-6*, 1273-1280.

(16)   Kruangam, D.; Toyama, T.; Hattori, Y.; Deguchi, M.; Okamoto, H.; Hamakawa, Y. *J. Non-Cryst. Solids* **1987**, *97-8*, 293-296.

(17)   Snell, A. J.; Mackenzie, K. D.; Spear, W. E.; Lecomber, P. G.; Hughes, A. J. *Appl. Phys.* **1981**, *24*, 357-362.

(18)   Carlson, D. E.; Wronski, C. R. *Appl. Phys. Lett.* **1976**, *28*, 671-673.

(19)   Cui, L. F.; Ruffo, R.; Chan, C. K.; Peng, H. L.; Cui, Y. *Nano Letters* **2009**, *9*, 491.

(20)   Limthongkul, P.; Jang, Y. I.; Dudney, N. J.; Chiang, Y. M. *Acta Materialia* **2003**, *51*, 1103.

(21)   Graetz, J.; Ahn, C. C.; Yazami, R.; Fultz, B. *Journal of the Electrochemical Society* **2004**, *151*, A698.

(22)   Han, G. B.; Lee, J. N.; Choi, J. W.; Park, J. K. *Electrochim. Acta* **2011**, *56*, 8997.

(23)   Hwang, C. M.; Park, J. W. *Thin Solid Films* **2010**, *518*, 6590.

(24)   Cui, L.-F.; Hu, L.; Wu, H.; Choi, J. W.; Cui, Y. *Journal of the Electrochemical Society* **2011**, *158*, A592.

(25)   Pell, L. E.; Schricker, A. D.; Mikulec, F. V.; Korgel, B. A. *Langmuir* **2004**, *20*, 6546.

(26)   Rabideau, B. D.; Pell, L. E.; Bonnecaze, R. T.; Korgel, B. A. *Langmuir* **2007**, *23*, 1270.

(27)   Erker, L. *Treatise on Ores and Assaying*; 2nd ed.; University of Chicago, 1951.

(28)   Franks, J. *Nature* **1956**, *177*, 984.

(29)   Sears, G.W. *Acta Metal.* **1955**, *3*, 361-365

(30)   Brenner, S.S. *Acta Metal*. **1956**, *4*, 62-63.

(31)   Wagner, R.S.; Ellis, W.C. *Appl. Phys. Lett.* **1964**, *4*, 89-90.

(32)   Johnson, E.R.; Amick, J.A. *J. Appl. Phys*. **1954**, *25*, 1204-1208.

(33)   Duan, X.; Huang, Y.; Agarwal, M.; Lieber, C.M. *Nature* **2003**, *421*, 241-245.

(34)   Cui, Y.; Lieber, C.M. *Science* **2001**, *291*, 851-853.

(35)   Huang, Y.; Duan, X.; Cui, Y.; Lauhon, L.J.; Kim, K.H.; Lieber, C.M. *Science*, **2001**, *294*, 1313-1317

(36)   Duan, X.; Huang, Y.; Lieber, C.M. *Nano Lett*. **2002**, *2*, 487-490.

(37)   McAlpine, M.C.; Ahmad, H.; Wang, D.; Heath, J.R. *Nat. Mater*. **2007**, *6*, 379-384.

(38)   Chan, C.K.; Patel, R.N.; O'Connell, M.J.; Korgel, B.A.; Cui, Y. *ACS Nano* **2010**, *4*, 1443-1450.

(39)   Tian, B.; Zheng, X.; Kempa, T.J.; Fang, Y.; Yu, N.; Yu, G.; Huang, J.; Lieber, C.M. *Nature* **2007,** *449*, 885-889

(40)   Chockla, A.M. *University of Texas at Austin Dissertations*, 2012

(41)   Chockla, A.M.; Harris, J.T.; Korgel, B.A. *Chem Mater*., **2010**, *23*, 1964-1970.

(42)   Chockla, A.M; Korgel, B.A. *J. Mater. Chem*. **2009**, *19*, 996.

(43)   Yu, H.; Buhro, W.E. *Adv. Mater*. **2003**, *15*, 416-420.

(44)   Span, R.; Springer: Berlin, 2000, p 367.

(45)   Hanrath, T.; Korgel, B.A. *J. Am. Chem. Soc*. **2002**, *124*, 1424.

(46)   Hanrath, T.; Korgel, B.A. *Adv. Mater.* **2003**, *15*, 437.

(47)   Armand, M.; Tarascon, J. M. *Nature* **2008**, *451*, 652.

(48)   Whittingham, M. S. *Science* **1976**, *192*, 1126.

(49)   Mizushima, K.; Jones, P. C.; Wiseman, P. J.; Goodenough, J. B. *Materials Research Bulletin* **1980**, *15*, 783.

(50)   Mizushima, K.; Jones, P. C.; Wiseman, P. J.; Goodenough, J. B. *Solid State Ion.* **1981**, *3-4*, 171.

(51)   Besenhard, J. O.; Eichinger, G. *Journal of Electroanalytical Chemistry* **1976**, *68*, 1.

(52)   Eichinger, G.; Besenhard, J. O. *Journal of Electroanalytical Chemistry* **1976**, *72*, 1.

(53)   Basu, S.; Zeller, C.; Flanders, P. J.; Fuerst, C. D.; Johnson, W. D.; Fischer, J. E. *Materials Science and Engineering* **1979**, *38*, 275.

(54)   Han, J. T.; Liu, D. Q.; Song, S. H.; Kim, Y.; Goodenough, J. B. *Chem. Mat.* **2009**, *21*, 4753.

(55)   Dahn, J. R.; Zheng, T.; Liu, Y. H.; Xue, J. S. *Science* **1995**, *270*, 590.

(56)   Mohri, M.; Yanagisawa, N.; Tajima, Y.; Tanaka, H.; Mitate, T.; Nakajima, S.; Yoshida, M.; Yoshimoto, Y.; Suzuki, T.; Wada, H. *J. Power Sources* **1989**, *26*, 545.

(57)   Alcantara, R.; Lavela, P.; Tirado, J. L.; Stoyanova, R.; Zhecheva, E. *Journal of Solid State Chemistry* **1997**, *134*, 265.

(58)   Chang, C. C.; Scarr, N.; Kumta, P. N. *Solid State Ion.* **1998**, *112*, 329.

(59)   Ohzuku, T.; Kitagawa, M.; Hirai, T. *Journal of the Electrochemical Society* **1990**, *137*, 769.

(60)   Wakihara, M. *Materials Science & Engineering R-Reports* **2001**, *33*, 109.

(61)   Liu, G. Q.; Zeng, C. L.; Yang, K. *Electrochim. Acta* **2002**, *47*, 3239.

(62)   Murphy, D. W.; Christian, P. A.; Disalvo, F. J.; Carides, J. N. *Journal of the Electrochemical Society* **1979**, *126*, 497.

(63)   Padhi, A. K.; Nanjundaswamy, K. S.; Goodenough, J. B. *Journal of the Electrochemical Society* **1997**, *144*, 1188.

(64)   Murphy, D. W.; Carides, J. N. *Journal of the Electrochemical Society* **1979**, *126*, 349.

(65)   Boukamp, B. A.; Lesh, G. C.; Huggins, R. A. *Journal of the Electrochemical Society* **1981**, *128*, 725.

(66)   Gao, B.; Sinha, S.; Fleming, L.; Zhou, O. *Advanced Materials* **2001**, *13*, 816.

(67)   Hatchard, T. D.; Dahn, J. R. *Journal of the Electrochemical Society* **2004**, *151*, A838.

(68)   Li, J.; Dahn, J. R. *Journal of the Electrochemical Society* **2007**, *154*, A156.

(69)   Li, H.; Huang, X. J.; Chen, L. Q.; Zhou, G. W.; Zhang, Z.; Yu, D. P.; Mo, Y. J.; Pei, N. *Solid State Ion.* **2000**, *135*, 181.

(70)   Yoon, S.; Park, C. M.; Sohn, H. J. *Electrochemical and Solid State Letters* **2008**, *11*, A42.

(71)   Xu, Y. H.; Yin, G. P.; Zuo, P. J. *Electrochim. Acta* **2008**, *54*, 341.

(72)   Park, M.-H.; Kim, M. G.; Joo, J.; Kim, K.; Kim, J.; Ahn, S.; Cui, Y.; Cho, J. *Nano Letters* **2009**, *9*, 3844.

(73)   Lee, J. K.; Smith, K. B.; Hayner, C. M.; Kung, H. H. *Chem. Commun.* **2010**, *46*, 2025.

(74)   Lee, J.-K.; Kung, M. C.; Trahey, L.; Missaghi, M. N.; Kung, H. H. *Chem. Mat.* **2009**, *21*, 6.

(75)   DiLeo, R. A.; Frisco, S.; Ganter, M. J.; Rogers, R. E.; Raffaelle, R. P.; Landi, B. J. *Journal of Physical Chemistry C* **2011**, *115*, 22609.

(76)   Cui, L.-F.; Yang, Y.; Hsu, C.-M.; Cui, Y. *Nano Letters* **2009**, *9*, 3370.

(77)   Hu, Y.-S.; Adelhelm, P.; Smarsly, B. M.; Maier, J. *Chemsuschem* **2010**, *3*, 231.

(78)   Wang, W.; Datta, M. K.; Kumta, P. N. *Journal of Materials Chemistry* **2007**, *17*, 3229.

(79)   Wang, W.; Kumta, P. N. *ACS Nano* **2010**, *4*, 2233.

(80)   Baggetto, L.; Hensen, E. J. M.; Notten, P. H. L. *Electrochim. Acta* **2010**, *55*, 7074.

(81)   Baggetto, L.; Notten, P. H. L. *Journal of the Electrochemical Society* **2009**, *156*, A169.

(82)   Graetz, J.; Ahn, C. C.; Yazami, R.; Fultz, B. *Electrochemical and Solid State Letters* **2003**, *6*, A194.

(83)   Laforge, B.; Levan-Jodin, L.; Salot, R.; Billard, A. *Journal of the Electrochemical Society* **2008**, *155*, A181.

(84)   Maranchi, J. P.; Kumta, P. N.; Hepp, A. F. In *Developments in Solid Oxide Fuel Cells and Lithium Ion Batteries*; Manithiram, A., Kumta, P. N., Sundaram, S. K., Chan, S. W., Eds. 2005; Vol. 161, p 121.

(85)   Rong, J. P.; Masarapu, C.; Ni, J.; Zhang, Z. J.; Wei, B. Q. *ACS Nano* **2010**, *4*, 4683.

(86)   Yao, Y.; McDowell, M. T.; Ryu, I.; Wu, H.; Liu, N. A.; Hu, L. B.; Nix, W. D.; Cui, Y. *Nano Letters* **2011**, *11*, 2949.

(87)   Chan, C. K.; Patel, R. N.; O'Connell, M. J.; Korgel, B. A.; Cui, Y. *ACS Nano* **2010**, *4*, 1443.

(88)   Chan, C. K.; Ruffo, R.; Hong, S. S.; Huggins, R. A.; Cui, Y. *J. Power Sources* **2009**, *189*, 34.

(89)   Hu, L. B.; Wu, H.; La Mantia, F.; Yang, Y. A.; Cui, Y. *ACS Nano* **2010**, *4*, 5843.

(90)   Huang, R.; Zhu, J. *Materials Chemistry and Physics* **2010**, *121*, 519.

(91)   Hanrath, T.; Korgel, B. A. *Advanced Materials* **2003**, *15*, 437.

(92)   Harris, J. T.; Hueso, J. L.; Korgel, B. A. *Chem. Mat.* **2010**, *22*, 6378.

(93)   Heitsch, A. T.; Akhavan, V. A.; Korgel, B. A. *Chem. Mat.* **2011**, *23*, 2697.

(94)   Heitsch, A. T.; Fanfair, D. D.; Tuan, H. Y.; Korgel, B. A. *J. Am. Chem. Soc.* **2008**, *130*, 5436.

(95)   Heitsch, A. T.; Hessel, C. M.; Akhavan, V. A.; Korgel, B. A. *Nano Letters* **2009**, *9*, 3042.

(96)   Fuller, C. S.; Severiens, J. C. *Phys. Rev.* **1954,** *96,* 21-24.

(97)   Park, M.-H.; Cho, Y.; Kim, K.; Kim, J.; Liu, M.; Cho, J. *Angew. Chem. Int. Ed.* **2011,** *50,* 9647-9650.

(98)   Lee, D. C.; Smith, D. K.; Heitsch, A. T.; Korgel, B. A., *Annual Reports on the Progress of Chemistry, Section C: Physical Chemistry* **2007**, *103*, 351.

(99)   Weller, D.; Doerner, M. F., *Annual Review of Materials Science* **2000**, *30*, 611.

(100)   Gao, J. H.; Gu, H. W.; Xu, B., *Accounts of Chemical Research* **2009**, *42*, 1097.

(101)   Johnson, D. C.; Mosby, J. M.; Riha, S. C.; Prieto, A. L. *Journal of Materials Chemistry* **2010**, *20*, 1993.

(102)   Sethuraman, V. A.; Kowolik, K.; Srinivasan, V. *J. Power Sources* **2011**, *196*, 393.

(103)   Fuller, C. S.; Severiens, J. C. *Physical Review* **1954**, *96*, 21.

(104)   Park, M. H.; Cho, Y.; Kim, K.; Kim, J.; Liu, M. L.; Cho, J. *Angewandte Chemie-International Edition* **2011**, *50*, 9647.

(105)   Teh, L. K.; Choi, W. K.; Bera, L. K.; Chim, W. K. *Solid-State Electronics* **2001**, *45*, 1963.

(106)   Smith, D. A.; Holmberg, V. C.; Korgel, B. A. *ACS Nano* **2010**, *4*, 2356.

(107)   Chockla, A. M.; Harris, J. T.; Akhavan, V. A.; Bogart, T. D.; Holmberg, V. C.; Steinhagen, C.; Mullins, C. B.; Stevenson, K. J.; Korgel, B. A. *J. Am. Chem. Soc.* **2011**, *133*, 20914.

(108) Tuan, H.-Y.; Korgel, B. A. *Chem. Mat.* **2008**, *20*, 1239.

(109) Yamamoto, Y.; Miura, T.; Suzuki, M.; Kawamura, N.; Miyagawa, H.; Nakamura, T.; Kobayashi, K.; Teranishi, T.; Hori, H. *Phys. Rev. Lett.* **2004**, *93*, 116801.

(110) Crespo, P. ; Litran, R. ; Rojas, T.C. ; Multigner, M. ; de la Fuente, J.M. ; Sanchez-Lopez, J.C. ; Garcia, M.A. ; Hernando, A. ; Penades, S. ; Fernandez, A. *Phys. Rev. Lett.* **2004**, *93*, 087204.

(111) Nunomora, N.; Hori, H.; Teranishi, T.; Miyake, M.; Yamada, S. **1998**, *249*, 5-6.

(112) Ayuela, A.; Crespo, P.; Garcia, M.A.; Hernando, A.; Echenique, P.M. *New Journal of Physics*. **2012**, *14*, 013064.

(113) Garitaonandia, J.S.; Insausti, M.; Goikolea, E.; Suzuki, M.; Cashion, J.D.; Kawamura, N.; Ohsawa, H.; de Muro, I.G.; Suzuki, K.; Plazaola, F.; Rojo, T. *Nano Letters*. **2008**, *8*, 661-667.

(114) Gonzalez, C. ; Simon-Manso, Y. ; Marquez, M. ; Mujica, V. *J. of Phys. Chem. B*. **2006**, *110*, 687-691.

(115) Hori, H. ; Yamamoto, Y. ; Iwamoto, T. ; Miura, T. ; Teranishi, T. ; Miyake, M. *Phys. Rev. B*. **2004**, *69*, 174411.

(116) Freknel, J.; Dorfman, J., *Nature* **1930**, *126*, 274.

Chapter 2: Synthesis of Hydrogenated Amorphous Silicon (a-Si:H) Colloids[§]

2.1 INTRODUCTION

Hydrogenated amorphous silicon (a-Si:H) has a wide variety of uses, including memory switching devices,[1,2] light-emitting diodes,[3] thin film transistors,[4] and solar cells.[5] For these applications, layers of a-Si:H are usually vapor-deposited on substrates. However, a variety of other applications would benefit from the availability of large quantities of a-Si:H *particles*.   Fuel cells, for example, require a safe and efficient way to store hydrogen.[6]   Nanoparticles of amorphous Si have high surface area-to-volume ratio and an ability to bond H,[7] and unlike the effective, yet reactive solid metal hydrides,[6] such as MgH_2 and $LiBH_4$,[8-10] are not dangerous. Hydrogen reversibly bonds to both crystalline and amorphous Si,[11,12] but a-Si has an advantage over crystalline Si, as H can penetrate the amorphous structure and loading is not limited to surface adsorption. In fact, nanostructured a-Si has been shown to absorb up to 50 atomic% hydrogen, or 3.4% hydrogen by weight.[13] Another possible application of a-Si nanoparticles is as an anode material in Lithium ion batteries. The theoretical capacity for Li storage in Si of 4212 mAh/g is much higher than that of the standard graphitic anode of 372 mAh/g.[14] Lithiation of Si, however, leads to a massive 400% volume expansion that pulverizes the material and destroys the battery. Nanostructured Si can mechanically tolerate this expansion and might offer a solution to this problem.[15-18] Since Li incorporation leads to amorphization, it may be suitable to use a-Si nanoparticles as the anode material.

[§] Portions of this chapter appear in *Chemistry of Materials*, **2010**, *23*, 6378.

One way to generate a-Si particles is by an aerosol process.[19-22] This approach, however, yields little control over particle size and it is difficult to produce spherical unaggregated particles larger than 100 nm or so in diameter. A few years ago, we demonstrated the synthesis of colloidal a-Si particles by decomposition of trisilane (Si_3H_8) in supercritical n-hexane (sc-hexane) at high temperature.[23,24] By pressurizing the solvent above its critical point, colloidal solution-phase particle synthesis can be carried out at relatively high temperature. The particles are spherical, relatively monodisperse, not aggregated and easily dispersed in organic solvents. We began to examine these particles in more detail and found that the structural bond order and hydrogen loading varies significantly in the particles, depending on their synthesis conditions. For example, the color of the a-Si particles can range from bright yellow to deep red to dark purple as the reaction temperature is increased from 380°C to 550°C. These color changes relate to the hydrogen content within the particles. The hydrogen content was found to correlate with the amount of structural order of the material. Here, we report the structural Si bond order and hydrogen content of a-Si:H particles synthesized under various conditions.

2.2 EXPERIMENTAL DETAILS

2.2.1 Reagents

All chemicals were used as received, without further purification. Trisilane (Si-$_3H_8$; 100%) was obtained from Voltaix. (Caution: trisilane is pyrophoric and must be handled in inert atmosphere). N-hexane (95%, anhydrous) was obtained from Sigma-Aldrich. Trisilane and n-hexane were stored in a nitrogen-filled glovebox. Chloroform (with 0.75% ethanol as preservative) was used as received from Fisher Scientific.

2.2.2 a-Si:H Particle Synthesis

a-Si:H particles were prepared by trisilane decomposition in supercritical n-hexane using a home-built batch-scale reactor, similar to that described previously.[23] The cylindrical reactor is solid titanium, with an internal volume of 10 mL and sealed with tapered titanium plugs that are tightened by titanium screws. The reactor is heated in a brass block with two resistive heaters coupled to a Variac controller set at 70% power. The reactor temperature is regulated by a thermocouple inside the heating block. The brass block is insulated with fiberglass in a larger aluminum box. The reaction pressure is controlled by varying the amount of solvent and trisilane added to the 10 mL reactor. The pressures reported here were determined from the n-hexane phase diagram.[25]

A typical reaction is carried out by loading the reactor with n-hexane and trisilane in a nitrogen-filled glove box. The reactor is then sealed and removed from the glove box and inserted into the heating unit. For example, a typical reaction run at 420°C and 34.5 MPa (5000 psi) is performed by loading in a nitrogen-filled glove box the 10 mL titanium reactor with 5.8 mL n-hexane and 25 μL trisilane. In the meantime, the heating block is preheated to 50°C (outside the glove box) above the desired reaction temperature (in this case, 470°C), with an empty reactor in the block to maintain good thermocouple contact. After sealing the reactor, it is removed from the glove box and placed into the preheated block.   The temperature initially drops to about 40°C below the desired reaction temperature and returns to the targeted temperature after 2.5 min. After a total of 10 min of heating, the reactor is removed from the heating block and submerged in an ice bath. [*Caution: DO NOT EXCEED the maximum tolerated pressure and temperature of the reactor! The titanium reactors used for these experiments are not reliable above 69.0 MPa (10000 psi) and 600°C. Furthermore, caution is required when opening the reactor after reactions carried out with higher trisilane concentrations. For example, when more*

25

than 300 μL of Si$_3$H$_8$ is added, not all of the Si$_3$H$_8$ decomposes in a 10 min reaction and the remaining Si$_3$H$_8$ will ignite if the reactor is opened in air.]

Once the reactor cools to room temperature (usually after about 10 min in the ice bath), the reactor is opened and the product is collected with 5 mL chloroform. The product is centrifuged at 8000 rpm for 5 min to precipitate the particles. The supernatant is discarded. The particles are redispersed in 2 mL chloroform with light sonication and then stored in ambient atmosphere. Reaction yields of ~60% are routinely acquired.

2.2.3 Materials Characterization

SEM images were obtained using a Zeiss Supra 40 VP SEM operated at 5 keV. The particles were suspended in chloroform and deposited by evaporation on Si substrates and imaged. Size distributions were determined by counting 300 particles for each sample imaged from random areas of the substrate.

TEM images were obtained using a Phillips 208 TEM operated at 80 keV for general imaging, or a JEOL 2010F TEM operated at 200 keV. Particles were dispersed in chloroform at 2.5 mg/mL concentration, and 5 μL of the mixture was dropped onto carbon-coated 200 mesh copper TEM grids (Electron Microscopy Sciences).

X-ray diffraction (XRD) was carried out using a Rigaku R-Axis Spider Diffractometer with Image plate detector with Cu-kα (λ = 1.542 Å) radiation operated at 40 kV and 40 mA. Measurements were taken on particles suspended on a 0.5 mm nylon loop. Samples were scanned for 10 min while rotating at 10° per minute at 298 K in ambient atmosphere. The resulting radial data was integrated over 10-90° 2θ and plotted. Background scattering from the nylon loop was subtracted from the sample measurement.

Attenuated total reflection fourier transform infrared (ATR-FTIR) spectra were acquired with a Thermo Mattson Infinity Gold FTIR with an ATR stage made of

crystalline ZnSe.   The detector was cooled by liquid nitrogen, and spectra taken by averaging 128 scans from 400-4000 cm^{-1} at 1 cm^{-1} resolution.   The a-Si colloids were dropcast onto the ATR stage from chloroform and dried under a nitrogen gas purge. Backgrounds scans were performed on the blank ATR stage after purging the chamber with nitrogen to remove all carbon dioxide and water signals and automatically subtracted from the sample spectra.

Simultaneous thermal gravimetric analysis (TGA) and differential scanning calorimetry (DSC) measurements were performed on a Mettler-Toledo TGA/DSC1. 5-10 mL of each sample were loaded in 70 μL alumina crucibles by dropcasting from chloroform and dried in ambient atmosphere. Samples were heated from 25°C to 800°C at 5°C/min under a nitrogen atmosphere with an 80 mL/min purge. The hydrogen content in the samples was calculated from the maximum weight loss of the sample without accounting for possible solvent loss or oxidation during the measurement.

Raman spectroscopy was conducted on a Renishaw inVia Microscope equipped with a 514.5 nm Argon laser in backscattering configuration.   The instrument was calibrated to the Stokes Raman signal at 521 cm^{-1} for a bulk single crystal of Si with the [110] direction oriented normal to the laser. The beam was focused on the sample using an optical microscope with a 50x objective lens. Samples were prepared by dropcasting the particles from chloroform dispersions onto glass slides. Spectra were obtained by single scans from 100-1200 cm^{-1}. The laser power was attenuated during most experiments from 10% (0.35 mW) to 50% (1.5 mW) of the maximum power. Single scans from multiple areas of each sample yielded reproducible Raman spectra. Samples did not exhibit further crystallization after several scans on the same spot at 10% (0.35 mW) laser power. Amorphous and more ordered phases were quantified by fitting the corresponding bands with Gaussian and Lorentzian-Gaussian curves centered at 470-475

cm^{-1} and 490-496 cm^{-1} respectively.[26] The ratios of the integrated areas of these bonds were used for the estimation of the nanocrystalline volume fraction and increasing bond order.[27,28]

2.3 RESULTS AND DISCUSSION

2.3.1 a-Si:H Particle Synthesis

Figure 2.1 shows SEM images of a-Si:H particles made by decomposing Si_3H_8 in sc-hexane at 420°C and 34.5 MPa (5000 psi) for 10 min. The particles are spherical and relatively monodisperse. The average diameter of the particles depended on the amount of Si_3H_8 used in the reaction, ranging from as small as 170 nm up to about 1.7 μm, increasing in diameter as the Si_3H_8 is increased. The standard deviation about the mean diameter is less than 10% in some cases (Figure 2.1A for example). The smallest particles obtained using this method are about 170 nm in diameter, as reactions carried out with less Si_3H_8 give very little product.
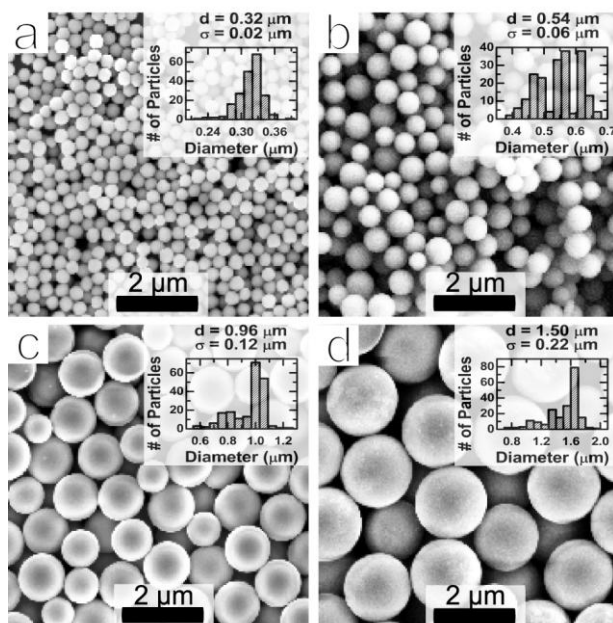
Figure 2.1: SEM images of a-Si:H particles synthesized in sc-hexane at 420°C at 34.5 MPa (5000 psi) with different amounts of Si_3H_8 added to the reactor: (a) 20 μL; (b) 60 μL; (c) 100 μL; (d) 300 μL   Insets: Particles size distributions determined from SEM images.

XRD showed that the particles are composed of hydrogenated amorphous silicon (a-Si:H).   Figure 2.2 shows XRD patterns of three different samples made at varying reaction temperatures of 380°C, 425°C, and 500°C. The diffraction data exhibit two broad diffraction peaks at 2θ values of 28.5° and 52°, characteristic of amorphous Si.[23,29-32]
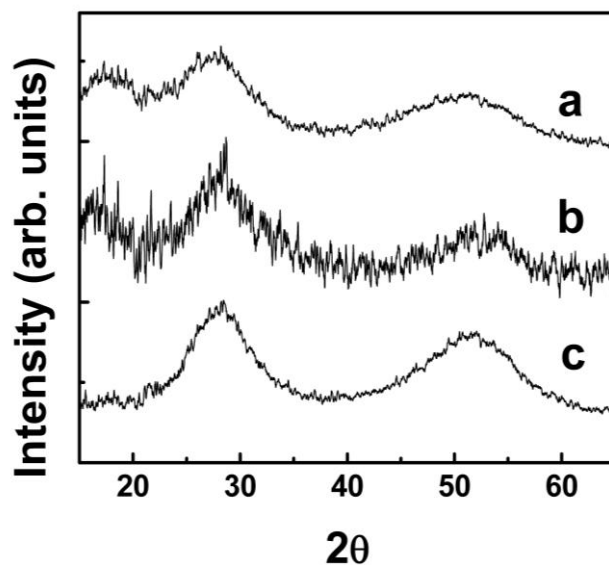
Figure 2.2: XRD of a-Si:H particles synthesized in sc-hexane at 34.5 MPa (5000 psi), 20 μL trisilane, and (a) 380°C, (b) 425°C, and (c) 500°C. The broad diffraction peaks at 2θ values of 52° and 28.5° are characteristic of a-Si:H.[23,29-32]

The particle morphology and optical properties were strongly affected by the reaction temperature. As shown in Figure 2.3, the color of the colloidal product varied from bright yellow, for the particles synthesized at the lowest temperature of 380°C, to red to a very dark purple (almost black) as the reaction temperature was increased to 550°C. The reaction temperature also affected the amount of aggregation between particles. Reaction temperatures greater than about 450°C led to significant aggregation with necking and some sintering between neighboring particles. Reaction temperatures below 400°C gave non-aggregated particles, but with rougher surfaces and a broader size distribution than those made at slightly higher temperature. Reactions carried out between 400 and 420°C produced particles with smooth surfaces, and the most monodisperse size distributions without aggregation. The effect of pressure on the system was also explored. At pressures below 24 MPa, large aggregates of a-Si were formed with no spherical

30
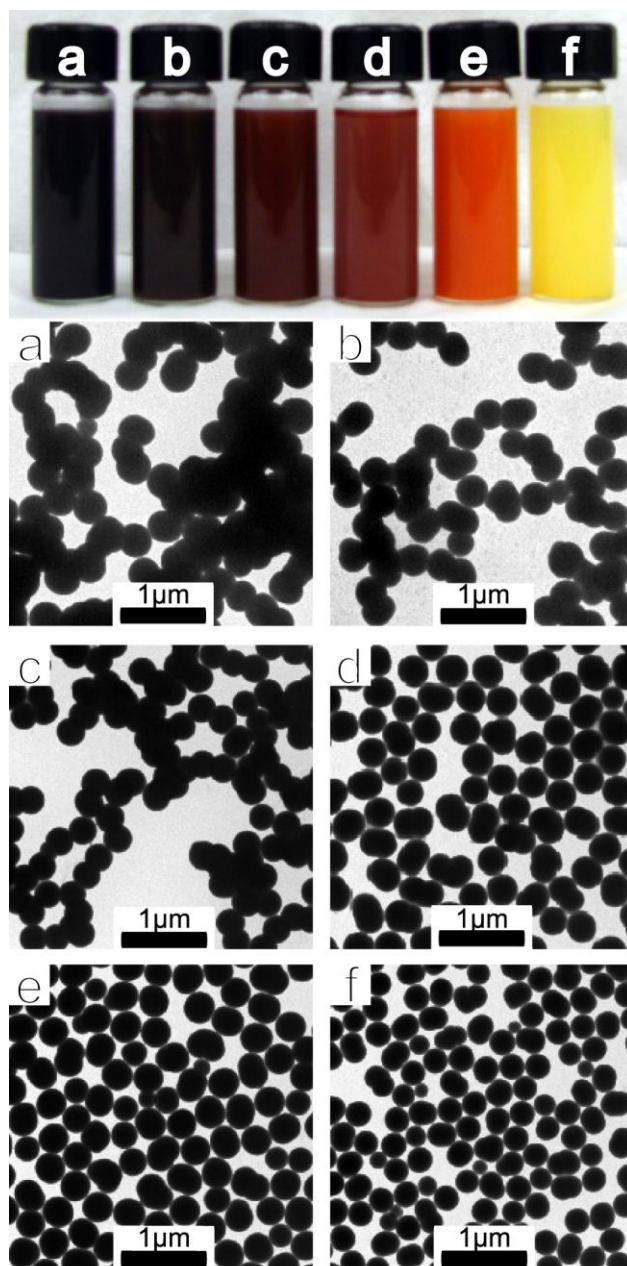
Figure 2.3: (Top) Photograph of vials of a-Si:H particles dispersed in chloroform that were made at different temperatures of (a) 550°C, (b) 500°C, (c) 450°C, (d) 420°C, (e) 400°C, and (f) 380°C. (Bottom) TEM images of the particles from the dispersions shown in the top panel. The labels correspond to those in the photograph. Particles were synthesized with 5 μL Si$_3$H$_8$ in sc-hexane at 34.5 MPa (5000 psi).

particles. Within the range of 27-45 MPa, no noticeable change in product was observed. Pressures above 45 MPa were not tested due to safety concerns.

2.3.2 Si-Si Bond Order in a-Si:H Particles

XRD (Figure 2.2) showed no evidence of a difference in structural order in the a-Si:H particles made at different reaction temperature, despite the fact that it has been shown to detect microcrystallinities of as low as 10%.[32] However, the difference in the color of the samples is consistent with changes in structure in the particles. The optical gap of a-Si can vary between 1.55 eV and 2.1 eV with differences in structural order and hydrogen content, increasing in energy with increasing disorder.[33-35] Raman spectroscopy is a much more sensitive probe to local atomic arrangements than XRD and was used to examine the particles. Figure 2.4 shows Raman spectra of a-Si:H particles synthesized at different temperatures and Si_3H_8 concentrations. Amorphous Si is characterized by a broad Raman band at ~475 cm^{-1} associated with the transverse optical (TO) mode and due to the stretching vibrations of the Si-Si bonds in the silicon tetrahedron.[26,28] Raman spectroscopy confirmed that all of the particle samples were mainly composed of amorphous Si when probed at 10% laser power. As the synthesis temperature was increased, the presence of a second Raman signal superimposed on the amorphous structure was dectected at ~490-496 cm^{-1}, indicating a higher amount of bond order in those samples. This trend became more evident when larger initial concentrations of Si_3H_8 were used in the reactions (Figure 2.4a-2.4c).
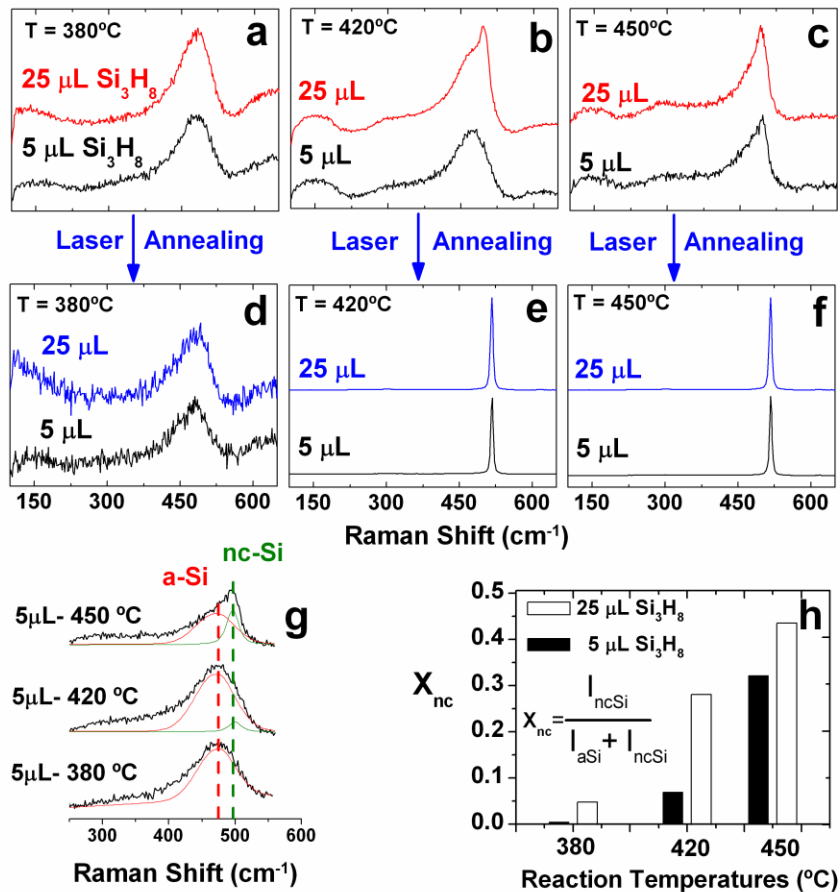
Figure 2.4: Raman spectra (λ_{exc}=514.5 nm) of a-Si:H particles made at different reaction temperature and Si_3H_8 concentration. Graphs (a)-(c) show the spectra obtained with the laser attenuated to 10% (0.35 mW) of its maximum power for the particles synthesized at (a) 380°C, (b) 420°C, and (c) 450°C. Graphs (d)-(f) correspond to those same particles after exposure at 50% (1.5 mW) laser power, collected with laser again attenuated to 10% power. Within each graph, the upper curve was synthesized with 25 µL of Si_3H_8 and the lower curve with 5 µL of Si_3H_8. Graph (g) shows the fitting of amorphous and crystalline contributions of the samples prepared with 5 µL of Si_3H_8 and exposed to 10% laser power. Fittings were obtained by utilizing Gaussian (a-Si:H) or a combination of Lorentzian-Gaussian (nc-Si) curves. Graph (h) shows the estimated volume fraction (X_{nc}) of 1-2 nm nanocrystallites embedded in the a-Si:H matrix. X_{nc} was obtained from the ratios of fitted integrated areas associated with the 1-2 nm nanocrystalline (490-495 cm^{-1}) and amorphous (475-480 cm^{-1}) phases corresponding to spectra (a)-(c). All samples were synthesized in 34.5 MPa (5000 psi) sc-hexane with 10 min of heating.

33

Another interesting observation was that particles synthesized at higher temperature could be crystallized under the probe laser used for the Raman experiments at 50% or higher power incidences (1.5 – 5.0 mW). When the particles made at 420°C and 450°C were again probed with the laser attenuated to only 10% power (0.35 mW) after exposure at 50% power (1.5 mW), they showed a sharp Raman peak centered at 516-518 cm^{-1}. This indicates the a-Si:H particles were annealed to microcrystalline Si (μc-Si) by laser irradiation. This shift of the TO peak toward higher wavenumbers is a result of a decreased phonon confinement effect.[26,36,37] Conversely, the particles synthesized at 380°C could not be crystallized under the Raman probe laser, even when operated at full laser power. The fact that the particles made at 380°C did not crystallize under the laser indicates that these particles were much more amorphous in character than those made at higher temperature. These differences in crystallization dynamics can be associated with the second Raman contribution detected at 490-496 cm^{-1} for the particles prepared at higher temperatures (Figure 2.4g). According to Zi's phonon confinement model, that peak can be assigned to 1-2 nm Si-ordered domains.[26,38] The most extensively used correlation length confinement model is not valid for such small diameters (minimum 4 nm).[26,36,37] The presence of these small, ordered Si clusters embedded in the amorphous Si matrix can act as seeds in the amorphous-to-crystalline transition observed under laser probe annealing. The absence of those seeds in the particles prepared at 380°C (Figure 2.4g) prevents the nucleation under the same annealing conditions.[26] The corresponding volume fraction of these embedded nanocrystals increases with reaction temperature and less so with initial Si_3H_8 concentrations (Figure 2.4h). Although the contribution of laser heating, even at only 10% power incidence, cannot be completely eliminated and may induce error in the

calculation of total crystalline volume fraction, the trend is undeniable. The particles synthesized at higher temperatures must possess a higher degree of structural ordering within the a-Si:H matrix associated with 1-2 nm Si ordered domains[26] or other intermediate ordered networks randomly distributed, as described by Tsu, et. al.,[28] that induced further crystallization upon laser annealing.

2.3.3 H-content in a-Si:H particles.

It is well-known that structural order tends to be correlated with hydrogen content in a-Si:H.[33,34]   Indeed, ATR-FTIR spectroscopy and TGA/DSC revealed significant differences in hydrogen content between the samples.   In ATR-FTIR spectroscopy, hydrogenated Si species tend to appear as spectral features related to Si-H, Si-H_2, and (Si-H_2)$_x$ chains.[39,40] TGA/DSC provides a quantifiable signature of hydrogen evolution when the sample is heated.

Figure 2.5 shows ATR-FTIR spectra of a-Si:H particles synthesized at a range of temperature. Peaks at ~2100 cm^{-1} and 900 cm^{-1}, corresponding to a Si-H stretches, were present in all of the spectra.[41] The spectra in Figure 2.5 have been normalized to the Si-H stretching frequency peak at ~2100 cm^{-1}. The presence of the peak at 870 cm^{-1} corresponding to the Si-H_2 wag, also provides an indication of how extensively hydrogenated the samples were. Particles made at 380°C had a significantly more intense peak at 870 cm^{-1} than at 900 cm^{-1}, indicating a large amount of hydrogen loading in those particles. The peak at 870 cm^{-1} was lower in intensity relative to the peak at 900 cm^{-1} for particles made at higher temperatures, indicating less Si hydrogenation.   When the reaction temperature was increased from 420°C to 425°C, there was a particularly noticeable difference in the spectra. Particles made at 420°C had a fairly significant Si-H_2 wag at 870 cm^{-1}, whereas particles made at 425°C did not exhibit this peak.   There

appears to be a qualitative change in the decomposition pathway of trisilane and Si incorporation into the growing particles at this temperature. ATR-FTIR spectra of particles made at 450°C do not exhibit the Si-H$_2$–related peak.
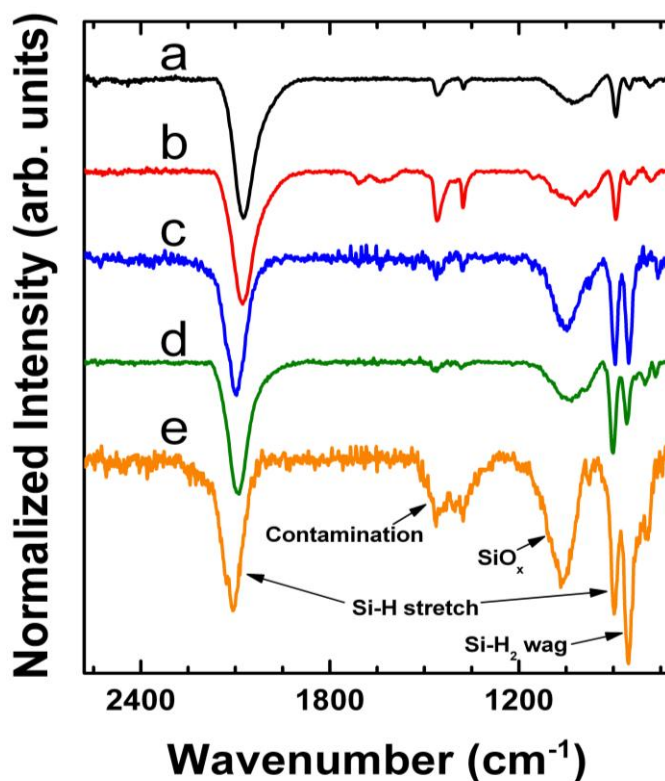
Figure 2.5: ATR-FTIR spectra of a-Si:H particles synthesized in sc-hexane at 34.5 MPa (5000 psi) with 25 μL of Si$_3$H$_8$ at various temperatures of (a) 450°C, (b) 425°C, (c) 420°C, (d) 400°C, and (e) 380°C. The spectra have been normalized to the intensity of the Si-H stretch at 2100 cm^{-1}.

The ATR-FTIR spectra clearly show that the hydrogen content is significantly higher in particles synthesized at lower temperature. TGA/DSC provided a quantitative estimate of the hydrogen loading in the samples. As shown in Figure 2.6, there is significant weight loss when the samples were heated. The majority of this weight loss is due to hydrogen desorption. The hydrogen content in the a-Si:H particles was significantly higher when

lower synthesis temperatures were used, increasing from 10 to 29 to 58 atomic% when the synthesis temperature was changed from 500°C to 425°C to 380°C, respectively. After hydrogen evolved from the sample, there was then a significant weight gain due to oxidation by residual oxygen in the chamber and the nitrogen source. The weight gain due to oxidation was largest for the particles made at the lowest temperature of 380°C. Unsatisfied Si bonds left by desorbed hydrogen appear to be more easily attacked by oxygen in these samples.
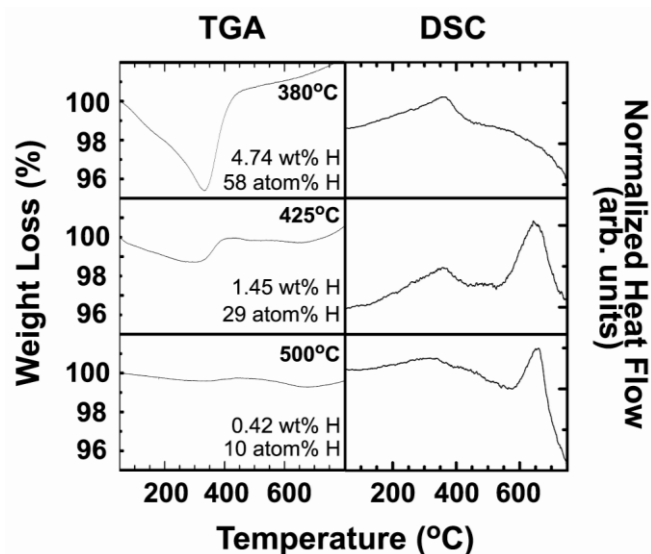
Figure 2.6: TGA/DSC data for a-Si:H particles synthesized with 50 μL Si_3H_8 in sc-hexane at 34.5 MPa (5000 psi) and temperatures of 380°C, 425°C, or 500°C. The temperature was increased at a rate of 5°C/min under flowing nitrogen. The weight loss in the sample is attributed to hydrogen desorption.

There is also a small exothermic peak in the DSC scan at ~340°C, when most of the hydrogen has desorbed and the particles are rapidly oxidizing.[13]   The particles synthesized at 425°C and 500°C exhibited exothermic spikes at 650°C due to the crystallization of the a-Si core.[7,42] Particles made at 380°C did not exhibit this feature in

37

the DSC data, indicating that there was no crystallization, most likely due to a prohibitively large amount of structural disorder in the particles and no nanocrystalline seeds.

2.4 CONCLUSION

Colloidal a-Si:H particles can be produced by Si_3H_8 decomposition in sc-hexane with a fairly wide range of size, hydrogen content and structural order, depending on the synthesis temperature, pressure and reactant concentration. Higher temperature reactions produced particles with more structural order and less associated hydrogen. Particles made at 450°C or higher were also slightly agglomerated. Raman spectroscopy was used as a sensitive probe to examine structural differences in the particles made at different temperature. The excitation laser used for Raman spectroscopy had enough power to crystallize particles that were synthesized at temperatures higher than 380°C due to the presence of intermediate order networks randomly distributed and small 1-2 nm ordered Si clusters that act as seeds for further crystallization. As far as we are aware, the reported method is the only available solution-phase approach to a-Si:H particles. Future work now involves examining their properties, including electrochemical studies on the potential of a-Si particles as a recipient for Li^+ implantation and the effects of hydrogen content on this process. The high hydrogen contents will also be tested for ease of removal and potential cyclability.

2.5 REFERENCES

(1)   Lecomber, P. G.; Owen, A. E.; Spear, W. E.; Hajto, J.; Snell, A. J.; Choi, W. K.; Rose, M. J.; Reynolds, S. *J. Non-Cryst. Solids* **1985**, *77-8*, 1373-1382.

(2)   Owen, A. E.; Lecomber, P. G.; Spear, W. E.; Hajto, J. *J. Non-Cryst. Solids* **1983**, *59-6*, 1273-1280.

(3)   Kruangam, D.; Toyama, T.; Hattori, Y.; Deguchi, M.; Okamoto, H.; Hamakawa, Y. *J. Non-Cryst. Solids* **1987**, *97-8*, 293-296.

(4)   Snell, A. J.; Mackenzie, K. D.; Spear, W. E.; Lecomber, P. G.; Hughes, A. J. *Appl. Phys.* **1981**, *24*, 357-362.

(5)   Carlson, D. E.; Wronski, C. R. *Appl. Phys. Lett.* **1976**, *28*, 671-673.

(6)   Bley, R. A.; Kauzlarich, S. M. *J. Am. Chem. Soc.* **1996**, *118*, 12461-12462.

(7)   Neiner, D.; Kauzlarich, S. M. *Chem. Mat.* **2010**, *22*, 487-493.

(8)   Fichtner, M. *Adv. Eng. Mater.* **2005**, *7*, 443-455.

(9)   Friedrichs, O.; Aguey-Zinsou, F.; Fernandez, J. R. A.; Sanchez-Lopez, J. C.; Justo, A.; Klassen, T.; Bormann, R.; Fernandez, A. *Acta Materialia* **2006**, *54*, 105-110.

(10)   Mauron, P.; Buchter, F.; Friedrichs, O.; Remhof, A.; Bielmann, M.; Zwicky, C. N.; Zuttel, A. *J. Phys. Chem. B* **2008**, *112*, 906-910.

(11)   Canaria, C. A.; Huang, M.; Cho, Y.; Heinrich, J. L.; Lee, L. I.; Shane, M. J.; Smith, R. C.; Sailor, M. J.; Miskelly, G. M. *Adv. Funct. Mater.* **2002**, *12*, 495-500.

(12)   Vandewalle, C. G.; Street, R. A. *Phys. Rev. B* **1995**, *51*, 10615-10618.

(13)   Farjas, J.; Das, D.; Fort, J.; Roura, P.; Bertran, E. *Phys. Rev. B* **2002**, *65*, 115403

(14)   Kasavajjula, U.; Wang, C. S.; Appleby, A. J. *J. Power Sources* **2007**, *163*, 1003-1039.

(15)   Chan, C. K.; Patel, R. N.; O'Connell, M. J.; Korgel, B. A.; Cui, Y. *ACS Nano* **2010**, *4*, 1443-1450.

(16)   Graetz, J.; Ahn, C. C.; Yazami, R.; Fultz, B. *Electrochem. Solid State Lett.* **2003**, *6*, A194-A197.

(17)   Li, H.; Huang, X. J.; Chen, L. Q.; Wu, Z. G.; Liang, Y. *Electrochem. Solid State Lett.* **1999**, *2*, 547-549.

(18)   Holzapfel, M.; Buqa, H.; Scheifele, W.; Novak, P.; Petrat, F. M. *Chem. Commun.* **2005**, 1566-1568.

(19)   Onischuk, A. A.; Strunin, V. P.; Ushakova, M. A.; Panfilov, V. N. *Khimicheskaya Fizika* **1994**, *13*, 129-138.

(20)   Everstei, F. C.; *Philips Research Reports* **1971**, *26*, 134-&.

(21)   Odden, J. O.; Egeberg, P. K.; Kjekshus, A. *Sol. Energ. Mat. Sol. C.* **2005**, *86*, 165-176.

(22)   Onischuk, A. A.; Strunin, V. P.; Samoilova, R. I.; Nosov, A. V.; Ushakova, M. A.; Panfilov, V. N. *J. Aerosol Sci.* **1997**, *28*, 1425-1441.

(23)   Pell, L. E.; Schricker, A. D.; Mikulec, F. V.; Korgel, B. A. *Langmuir* **2004**, *20*, 6546-6548.

(24)   Rabideau, B. D.; Pell, L. E.; Bonnecaze, R. T.; Korgel, B. A. *Langmuir* **2007**, *23*, 1270-1274.

(25)   Yaws, C. L. *Handbook of Thermodynamic Properties*; Gulf Publishing Company: Houston, TX, 1996; Vol. 2.

(26)   Viera, G.; Huet, S.; Boufendi, L. *J. Appl. Phys.* **2001**, *90*, 4175-4183.

(27)   Gajovic, A.; Gracin, D.; Juraic, K.; Sancho-Parramon, J.; Ceh, M. *Thin Solid Films* **2009**, *517*, 5453-5458.

(28)   Tsu, D. V. ; Chao, B. S. ; Jones, S. J. *Sol. Energ. Mat. Sol. C.* **2003**, *78*, 115-141.

(29)   Mahan, A. H.; Yang, J.; Guha, S.; Williamson, D. L. *Phys. Rev. B* **2000**, *61*, 1677-1680.

(30)   Mamiya, M.; Takei, H.; Kikuchi, M.; Uyeda, C. *J. Cryst. Growth* **2001**, *229*, 457-461.

(31)   Williamson, D. L. *Sol. Energ. Mat. Sol. C.* **2003**, *78*, 41-84.

(32)   Guha, S.; Yang, J.; Williamson, D. L.; Lubianiker, Y.; Cohen, J. D.; Mahan, A. H. *Appl. Phys. Lett.* **1999**, *74*, 1860-1862.

(33)   Cody, G. D.; Tiedje, T.; Abeles, B.; Brooks, B.; Goldstein, Y. *Phys. Rev. Lett.* **1981**, *47*, 1480-1483.

(34)   Sokolov, A. P.; Shebanin, A. P.; Golikova, O. A.; Mezdrogina, M. M. *J. Phys.-Condes. Matter* **1991**, *3*, 9887-9894.

(35)   Fukutani, K.; Kanbe, M.; Futako, W.; Kaplan, B.; Kamiya, T.; Fortmann, C. M.; Shimizu, I. *J. Non-Cryst. Solids* **1998**, *227*, 63-67.

(36)   Richter, H.; Wang, Z. P.; Ley, L. *Solid State Commun.* **1981**, *39*, 625-629.

(37)   Campbell, I. H.; Fauchet, P. M. *Solid State Commun.* **1986**, *58*, 739-741.

(38)   Zi, J.; Buscher, H.; Falter, C.; Ludwig, W.; Zhang, K. M.; Xie, X. D. *Appl. Phys. Lett.* **1996**, *69*, 200-202.

(39)   Webb, J. D.; Gedvilas, L. M.; Crandall, R. S.; Iwaniczko, E.; Nelson, B. P.; Mahan, A. H.; Reedy, R.; Matson, R. J. *Mater. Res. Soc. Symp. P.* **1999,** *557*, 311-316.

(40)   Roura, P.; Farjas, J.; Rath, C.; Serra-Miralles, J.; Bertran, E.; Cabarrocas, P. R. I. *Phys. Rev. B* **2006**, *73*, 085203.

(41)   Lucovsky, G.; Nemanich, R. J.; Knights, J. C. *Phys. Rev. B* **1979**, *19*, 2064-2073.

(42)   Spinella, C.; Lombardo, S.; Priolo, F. *J. App. Phys.* **1998**, *84*, 5383-5414.

Chapter 3: Enhanced Lithiation of Si Nanostructures Through Increased Surface Conductivity[§]

3.1 INTRODUCTION

Much of the research on lithium ion batteries (LIBs) currently focuses on developing lightweight and high energy density materials for applications such as electric and hybrid vehicles.[1] Carbon anodes have proven very useful due to their stable cycling characteristics, but suffer from limited charge storage capacity (gravimetric capacity of 372 mAh/g).[2] In search of higher capacity anode materials, lithium alloying materials have drawn considerable interest due to their high gravimetric and volumetric energy density. Among lithium alloying materials, Sn and Si show excellent electrochemical lithium alloying capabilities.[3,4] Si can alloy with lithium at room temperature to form $Li_{15}Si_4$, corresponding to a very high charge storage capacity of 3579 mAh/g that is approximately 10 times higher in gravimetric density than graphite.[5] However, Si-based anodes face several challenges. First, crystalline Si anodes undergo a 400% volume expansion during the lithiation process and then returns to their original volume after delithiation; this volume expansion and contraction causes pulverization of the Si and loss of electrical contact with the current collector. Secondly, the electrochemical alloying potential window of Si is above the lowest unoccupied molecular orbital (LUMO) level of most solvents, which leads to solvent decomposition and the formation of a solid electrolyte interface (SEI).[6] While SEI formation has been well studied in graphite anodes, the process is not fully understood for Si anodes.[7]

Different approaches have been explored to overcome the problem of volume expansion and contraction upon lithiation and delithiation of Si anodes. One approach is

[§] Portions of this chapter appear in *Chemistry of Materials*, **2012**, *24*, 1306-1315 and *Journal of the American Chemical Society*, **2011**, *133*, 20914.

to use nanostructures, such as nanocrystals, nanowires, nanotubes or nanorods. Kim *et al* have shown that Si nanotubes prepared in alumina membrane templates exhibit a very high reversible specific charge storage capacity of 3247 mAh/g with a Coulombic efficiency of 89%.[8] Similarly, Si nanowires[9] and porous Si[10] show high reversible capacities with long-term cycle stability. Unfortunately, it is very difficult to produce these materials at a reasonable cost in the bulk quantities required for commercial application.

Another approach to increase the stability of the electrode is to add buffer materials to stabilize the electrode during the volume change process. The buffer materials act as a strong mechanical support during lithium insertion and removal. Typically, carbon materials have been used as the buffer material in different architectural configurations. In core-shell nanoarchitectures, Si is coated over carbon nanotubes and fibers. The carbon undergoes less structural change than Si and acts as a mechanical support with efficient electron transfer.[11] Others have embedded Si particles and nanowires in carbon networks. Porous carbon networks can allow rapid access of Li ions to the Si particles.[12] Mixing Si nanowires with multiwall carbon nanotubes as a conducting buffer material led to relatively high reversible capacities of 1500 mAh/g for over 30 cycles.[13]

Heterostructure configurations of a conducting metallic substrate and Si coating have also been reported. For example, two-dimensional crystalline $TiSi_2$ nanonets with a particulate Si coating showed an increased performance over pure Si during the charge/discharge process.[14] Heterostructures are also used to reduce strain during lithiation and prevent inhibit pulverization. In one case, an amorphous carbon nanorod was coated with a layer of Al and capped by a layer of Si. The intermediate layer of Al reduces the mismatch in strain between the C and Si interfaces to enable stable operation

of the electrode under high-rate charge/discharge conditions.[15] However, in all of the above approaches, the buffer materials and the conducting components undergo lithiation reactions and it is difficult to determine the cause of failure in the battery electrodes. Furthermore, the lithiation potentials of the buffer materials are below the LUMO levels of the solvent, facilitating solvent decomposition on the Si surface. This leads to enhanced SEI layer formation, inhibiting lithiation and leading to failure of the battery electrodes.

As previously mentioned, the highest capacity LIB anodes have been nanostructured Si with high inherent electrical connectivity from being grown directly on conductive substrates. Unfortunately, the previously reported methods are high-cost, low throughput and not usable for commercial appications. Solution based syntheses of Si nanostructures yield high quantities of material through scalable processes, but do not have inherent conductivities high enough to function as high capacity LIB anodes. This problem is circumvented by enhancing the conductivity of the nanostructures. This chapter focuses on two techniques for enhancing conductivity: (1) coating a-Si:H particles with Cu nanoparticles and (2) annealing monophenylsilane (MPS) grown Si nanowires to deposit a conductive carbon coating on their surfaces.

3.2 CU-COATED A-SI (A-SI@CU) PARTICLES[§]

3.2.1 Introduction

Electrochemical lithiation/delithiation of crystalline Si leads to amorphization in only a few cycles. Once the amorphous phase is formed, the lithiation process stabilizes and additional pulverization and capacity loss is low.[16] Therefore, a-Si has been proposed for LIB applications, as there is no advantage to using crystalline Si after the

---

[§] Portions of this section appear in *Chemistry of Materials*, **2012**, *24*, 1306-1315.

first few cycles. a-Si has other potential advantages over crystalline Si, including a smaller predicted volume expansion, shorter lithium ion diffusion lengths, and smaller charge transfer resistance.[17] Nano-sized a-Si should offer even better tolerance to volume expansion/contraction processes. Recently, it has been shown that crystalline Si nanowires coated with a-Si have high charge storage capacity (~1000 mAh/g, three times the capacity of carbon) with a 90% capacity retention over 100 cycles.[17-18] Unfortunately, a-Si has a lower electrical conductivity and slower lithium insertion than its crystalline counterpart. To enhance the conductivity, and consequently, lithium insertion, metal coatings have been explored. Previously, it has been suggested that a coating of metal particles on Si particles significantly improves the electrical contact and cyclablity of lithium insertion reactions. [19] Yu *et al* reported that depositing silver on macroporous Si improved battery performance and reversible lithium storage.[20] Multi-layer Fe/Si structures exhibited suppressed volumetric expansion during cycling.[51] Cu deposition on Si has been used to enhance the electrical conductivity of Si powder by annealing to form Cu_3Si alloy at the interface of Cu and Si to enhance the electrical conductivity.[22] Recently, sputtered Cu coatings on crystalline Si showed increased cycling efficiency and rate capability of Si electrodes. [23]

In this report, Cu metal coatings were deposited on colloidal a-Si:H particles through a polyol reduction method. The Cu coating led to: (1) enhanced charge transfer kinetics and reduced charge transfer resistance, (2) more reversible and increased charge storage capacity, and (3) improved tolerance to volumetric expansion/contraction processes. Also, this Cu coating method is fully scalable to large quantity throughput.

3.2.2 Experimental Section

3.2.2.1 Reagents

All chemicals were used as received, without further purification. N-hexane (95%, anhydrous) and ethylene glycol (anhydrous) was obtained from Sigma-Aldrich. Trisilane (Si_3H_8; 100%) was obtained from Voltaix (*Caution: trisilane is extremely pyrophoric and must be stored in an inert atmosphere!*) Cu (II) acetate (anhydrous) was obtained from Fluka. Super P carbon black 99% (metals basis) was obtained from Alfa Aesar. Polyvinylidene fluoride (PVDF) was obtained from Aldrich. N-methylpyrrolidinoe (NMP) (99% extra pure) was obtained from Acros organics. 1 M $LiPF_6$ in a 1:1 weight ratio of ethylene carbonate to diethyl carbonate (Purolyte[®] Electrolyte with less than 200 ppm water) was obtained from Novolyte technologies. Lithium foil was obtained from Sigma-Aldrich. Chloroform (with 0.75% ethanol as preservative) was obtained from Fisher Scientific. Trisilane and n-hexane were stored in a nitrogen filled glove box.

3.2.2.2 Synthesis of Cu coated a-Si:H

The synthesis of colloidal hydrogenated amorphous silicon (a-Si:H) particles has been reported in our earlier publication.[37] In short, the particles are synthesized via the thermal decomposition of trisilane (Si_3H_8) in supercritical n-hexane at 34.5 MPa (5000 psi) in a titanium batch reactor. Control over particle size and hydrogen content is attained by adjusting the initial trisilane concentration and reaction temperature. The particles are spherical and relatively monodisperse.[37a] The average particle diameter was varied from 170 nm to 1.7 μm while hydrogen content was varied from 10 atomic% to 58 atomic% with reactions temperatures of 500°C down to 380°C, respectively.

In a typical Cu coating reaction, a-Si:H particles were synthesized by decomposing 150 μL of Si_3H_8 in supercritical n-hexane at 400 °C and 34.5 MPa (5000 psi) for 10 min. The particles were 850 nm in diameter (as measured by SEM) and the hydrogen content of the particles was 40 atomic% (as estimated by TGA-DSC). Cu was deposited on the colloidal a-Si:H particles by a polyol-mediated reduction of Cu precursors. The reaction was performed in a schlenk line under inert atmosphere. Pre-synthesized a-Si:H particles dispersed in 20 mL ethylene glycol (anhydrous, Sigma Aldrich) in a round bottom flask. The mixture was degassed under vacuum at 80 °C for 10 minutes to remove volatile impurities. The mixture was then placed under N_2 atmosphere and heated at ~10 °C/min to 120 °C. A 5mL solution of Cu (II) acetate in ethylene glycol was injected after the reaction temperature stabilized at 120 ºC. The injection was performed over 10 min to avoid a drastic drop in reaction temperature. Once the Cu precursor was injected into the reaction chamber, it the temperature of the system was slowly raised to 140 ºC. This temperature was maintained for 4 h, and then the reaction was quenched to room temperature. Different loading levels of Cu over the a-Si:H particles were studied by varying the amount of Cu precursor used in the reaction. The effect of initial particle hydrogen loading on Cu deposition was also studied by maintaining constant Cu concentration while varying the a-Si:H hydrogen content.

3.2.2.3 Electrode preparation and analysis

The electrodes were prepared by creating a slurry of a-Si:H particles or Cu coated a-Si:H as the active material, Super P carbon black as an electronic conductor, and PVDF dissolved in NMP as binder in a 70:20:10 ratio by weight. The as-prepared slurry was coated onto a Cu foil and dried under vacuum at 120 ºC for 6 hours. The electrodes were cut into 12.5 mm diameter disks. The coin cells (2032 type) were assembled in an

argon filled glove box using metallic lithium as the counter electrode and 1M LiPF$_6$ dissolved in ethylene carbonate (EC) and diethyl carbonate (DEC) (1:1 in weight ratio) as the electrolyte solution. A polypropylene membrane (Celgard 2400, Celgard) was used as a separator. The cells were assembled in an argon-filled glove box (Unilab 2000, MBraun).

3.2.2.4 Materials Characterization

Scanning electron microscopy (SEM) was performed with a Hitachi S-5500 high-resolution scanning electron microscope (STEM) operating at 30.00 kV or a Zeiss Supra 40 VP SEM operated at 5 keV. A small amount of the sample dispersed in acetone was dropped into the Au TEM grid covered with a thin amorphous carbon film (Ted Pella) for the STEM analysis. For particle sizing, particles were suspended in chloroform and deposited by evaporation on Si substrates and imaged. 300 particles were counted from random areas of the substrate from each sample.

Thermal gravimetric analysis (TGA) was performed on a Mettler-Toledo TGA/DSC1. 5-10 mL of each sample were loaded in 70 μL alumina crucibles by drop casting from chloroform and dried in ambient atmosphere. Samples were heated from 25 to 800 $^{\circ}$C at 5 $^{\circ}$C/min under a nitrogen atmosphere with an 80 mL/min purge. The hydrogen content in the samples was calculated from the maximum weight loss of the sample without accounting for possible solvent loss or oxidation during the measurement.

X-ray photoelectron spectroscopy (XPS) was performed with a Kratos AXIS Ultra DLD system calibrated using the signals for Au 4f$_{7/2}$ at 83.98 eV. Spectrums were collected at 0.05 eV steps with 1000 ms integration time at each step and the measurements were conducted under a vacuum of 10^{-9} Torr.Sputtering experiments were

conducted at 4kV. XPS samples were prepared by dropcastingapproximately 2 mg of sample onto a clean 1x1 cm glassy carbon disc.

X-ray diffraction (XRD) was used to find the crystallinity and composition of the films. A Rigaku R-Axis Spider X-ray diffractometer with Image plate detector was used with a Cu-Kα (λ = 1.542 Å) source operated at 40 kV and 40 mA. Samples were loaded in a 0.5 mm Nylon loop and scanned for 30 minutes while rotating at 2° per minute. The resulting radial data were integrated over 10-90° 2θ with 2DP software. The peaks were analyzed using JCPDS (Joint Committee on Powder Diffraction Standards).

Fourier Transform IR – CO probe experiments were performed on the Cu coated a-Si:H colloidal suspension. Initially, CO gas (Airgas) was bubbled using a stainless steel needle submerged in the suspension at a flow rate of 35 sccm for 10 minutes. A liquid IR cell was filled with a 100 μL aliquot of the CO saturated sample and monitored in a Bruker FT-IR spectrometer.All the spectra are acquired from 400 – 4000 cm^{-1} with 4 cm-1 resolution byaveraging 32 scans. The liquid IR cell consisted of a 0.5 mm Teflon spacer sandwiched between two rectangular CaF$_2$ windows. The colloidal suspension prior to CO bubbling was used for the background spectra.

All the galvanostatic cycling experiments were performed with a multichannel battery test system (BT 2000, Arbin). The cells were tested at a constant current density with voltage cutoff of 3 V/0.01V versus Li/Li$^+$.

Raman spectroscopy was performed with a Renishaw In Via microscope system utilizing a 514.5 nm Argon laser in back-scattering configuration. The instrument was calibrated to the Stokes Raman signal at 521 cm^{-1} using a bulk single crystal of Si with the [110] direction oriented normal to the laser. For the ex-situ analysis, the beam was focused using a 50X aperture resulting in an approximately 2 μm diameter sampling cross section. To avoid crystallization of the a-Si:H particles, five accumulations at low

power (10%, 3 mW) with 10 s exposure time was used. To perform *in situ* Raman measurements, an optically transparent quartz window was mounted on one side of the coin cell (2032) with Torr-seal. Prior to affixing the quartz window ~3 mm diameter hole was drilled in the coin cell component, washed with acetone, and dried. The coin cell battery was assembled using the procedure previous outlined, but the sample coated on the Cu disc was faced toward the quartz window. The coin cell was mounted on the Raman stage and focused using a long working distance objective lens. A 514.5 nm green laser set to 50% power setting for 10 s exposure time was used for each measurement, with five accumulations per measurement. The coin cell was connected to a computer controlled potentiostat (EG&G 263A). The charging/discharging measurements were triggered simultaneously with Raman measurements. For the charging/discharging measurements a 100 mA/g load was used.

3.2.3 Results and Discussion: Cu Deposition on a-Si:H Particles

3.2.3.1 Nature of Deposition

A low temperature solution-based polyol method was developed for depositing Cu on colloidally-grown a-Si:H particles. The low temperature chemical method has advantages over high energy processes such as physical vapor deposition or atomic layer deposition (ALD) in its ease of application and ability to deposit Cu uniformly over the particle surface area. Additionally, the low temperature method will not induce crystallization of a-Si:H, as opposed to the aforementioned high temperature techniques. The polyol method offers the ability to control shape and size of Cu particles. Cu nanoparticle synthesis by the polyol method is typically performed with a reducing agent such as $NaBH_4$, $NaH_2PO_2 \cdot H_2O$ or ascorbic acid, or with a chelating agent such as PVP (polyvinylpyrrolidone).[24] PVP, however, is very difficult to completely remove from the

49

reaction mixture, even after multiple washes.[25] Therefore, ethylene glycol was used both as solvent and reducing agent to form Cu. This approach avoids contamination of the a-Si:H particles with chelating ligands. In ethylene glycol, the process can be carried at lower temperatures (140-160 ºC) for a shorter period of time (2-4 h) compared to other solvents like oleylamine (230 ºC, 6h).[26]
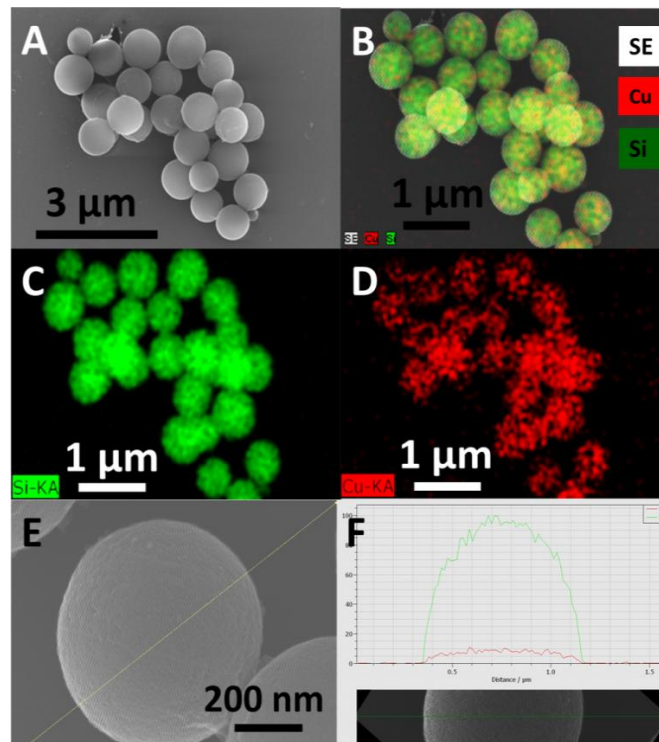
Figure 3.1: (A) STEM-EDS image of 620 nm spherical a-Si:H particles coated with Cu using a 50:1 a-Si:H : Cu ratio. (B) Elemental analysis showing the presence of Cu and Si. (C) Elemental analysis of showing the presence of Si. (D) Elemental analysis showing the presence of Cu. (E) Line scan image of a single copper coated a-Si:H particle. (F) Elemental analysis of line scan showing the presence and location of Si and Cu.

620 nm a-Si:H particles were coated with copper (50:1 a-Si:H : Cu) using ethylene glycol as reducing agent. Figure 3.1 shows scanning transmission electron

microscopy with energy dispersive x-ray spectroscopy (STEM-EDS) analysis of Cu-coated a-Si:H particles. The particles are 620 nm in diameter with smooth surfaces after the Cu coating, and elemental mapping analysis confirms the presence of Cu on the Si particles (Figure 3.1 B-F).
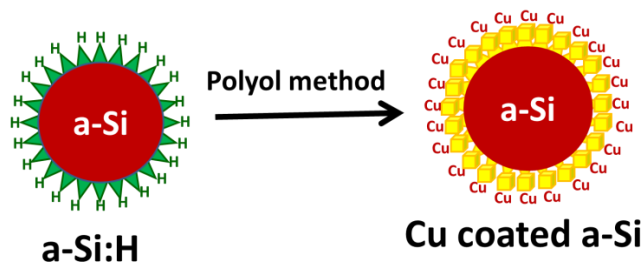
Illustration 3.1: Schematic representation of the polyol method used for coating Cu over a-Si:H particles.

Low loading levels of Cu (Figure 3.1) resulted in the formation of very small Cu particles with uniform coverage over the surface of the a-Si:H particles, as represented in Illustration 3.1. The polyol method of Cu coating a-Si:H particles was compared to conventional physical mixing of Cu with a-Si:H particles. Mixing the a-Si:H particles with Cu particles produced a non-uniform Cu coating. Furthermore, this physical mixing method involves a high temperature Cu reduction which leads to crystallization of a-Si:H and alloying of Cu with Si as confirmed by XRD and Raman experiments. To understand the deposition of copper over a-Si:H by polyol reduction, a series of experiments was performed while varying the loading levels of Cu during synthesis. High concentrations of Cu (10:1 mole ratio of a-Si:H : Cu) led to the formation of 10-15 nm cube-shaped crystals over the a-Si:H surface (Figure 3.2). In many images, the Cu particles bridge neighboring a-Si:H particles (Figure 3.2c). However, high resolution TEM analysis (Figure 3.2d) shows a lattice d-spacing of 2.45 Å instead of the crystalline

metallic Cu d-spacing of 2.08 Å (111). This change in lattice spacing is due to oxidation of metallic copper, with 2.45 Å corresponding to the Cu_2O (111) lattice d-spacing. The nature of deposited copper is further analyzed with XRD, FT-IR and XPS in detail.
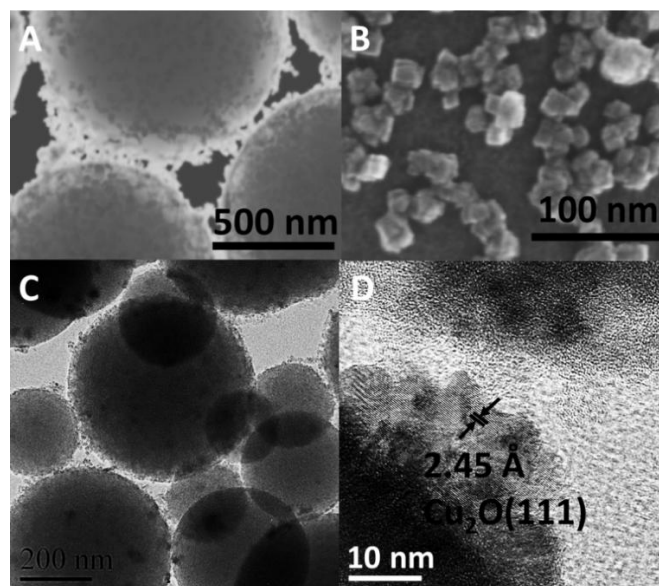
Figure 3.2: (A) STEM dark field image of Cu coated a-Si:H particles synthesized with a 10:1 a-Si:H : Cu mole ratio. (B) Closer look at the cubic shaped Cu crystals. (C) TEM images of high Cu coated a-Si:H particles showing the bridging between particles. (D) HRTEM image showing lattice fringes with a d-spacing of 2.45Å corresponding to Cu_2O formation.

3.2.3.2 Chemical Structure of Cu on Si

Figure 3.3a shows XRD data of Cu-coated a-Si:H particles prepared with varying amounts of Cu. The presence of Cu is confirmed by the presence of peaks at $43.2°$ (111), $50.4°$ (200) and $74.1°$ (220) 2θ. The amorphous nature of the Si is maintained after the Cu coating as shown by the presence of broad peaks at $28.4°$, $47.3°$ and $56.1°$ 2θ. For a-Si:H particles with relatively low H content ($Si_{0.75}H_{0.25}$), crystalline Cu was detected only at higher Cu coating levels (25:1 and 10:1 a-Si:H : Cu loading). It has been shown in the literature that the presence of Cu_2O over Cu metal is inevitable, due to the presence of

trace water impurities in the solvent or oxidation of samples when exposed to air.[24a, 27] The oxidation state of the Cu on the a-Si:H particles was determined using an FT-IR-CO probe.
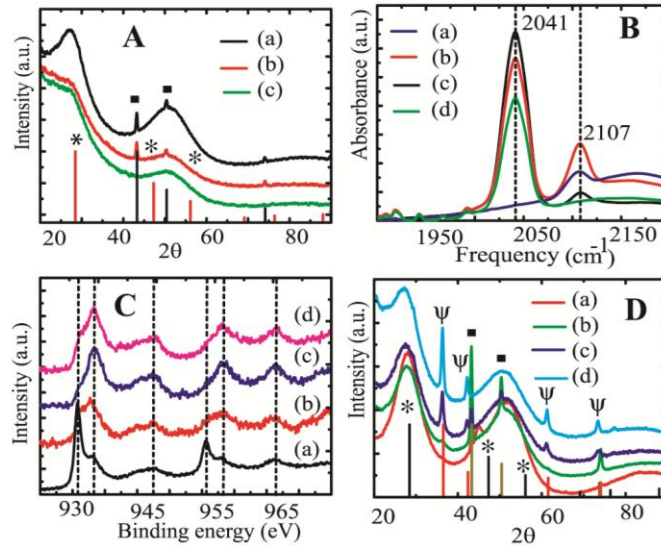
Figure 3.3: (A) XRD of a-Si:H ($Si_{0.75}H_{0.25}$) particles treated with different Cu loadings: (a) 10: 1, (b) 25:1, (c) 50:1, red line with * symbol shows the standard Si (JCPDS#89-5012) and black lines with (■) shows the Cu (JCPDS#04-0836). (B) FTIR-CO probe analysis showing the CO interaction with metallic Cu and copper oxide for different loading ((a) 1:1, (b) 10:1, (c) 25:1 and (d) 50:1) of Cu coated a-Si:H particles. (C) High resolution XPS analysis of Copper on the Cu coated a-Si:H particles with different loading of copper such as (a) 10:1, (b) 25:1, (c) 50:1 and (d) 100:1 mole ratios. (D) XRD analysis of (50:1 a-Si:H : Cu) copper loading on different hydrogen concentration a-Si:H particle, where (a) a-$Si_{0.9}H_{0.1}$, (b) a-$Si_{0.75}H_{0.25}$, (c) a-$Si_{0.6}H_{0.4}$ and (d) a-$Si_{0.5}H_{0.5}$. The peaks corresponding to Cu (yellow color lines with (■) symbol) at values of 43.2° (111), 50.4° (200) and 74.1° (220) 2θ grow with increasing hydrogen concentration. Black line with * symbol shows the standard Si (JCPDS#89-5012) and red lines with ψ shows the Cu_2O (JCPDS#77-0199).

Figure 3.3b shows the FT-IR spectrum of Cu-coated a-Si:H prepared with varying amounts of Cu. Peaks at 2041 cm^{-1} and 2107 cm^{-1} correspond to the stretching frequency

of linearly adsorbed CO on metallic Cu and Cu^{n+} sites, respectively.[28] Higher Cu loading led to more Cu oxide formation. This may be attributed to more deposition of Cu particles with thin Cu_2O shells on the a-Si:H surface.

In the case of high hydrogen (50% hydrogen) content, the a-Si:H particles show only the presence of Cu_2O with no metallic Cu. This behavior can be attributed to the large amount of Cu particles grown on the surface of a-Si:H which undergo oxidation to form an oxide layer. If the oxide layer thickness is greater than the penetration depth of X-rays, it is very difficult to observe the metallic phase of Cu. Thus, this formation of Cu oxide is related to the high concentration of copper and direct evidence of high Cu nucleation on a-Si:H surfaces with high hydrogen concentration.
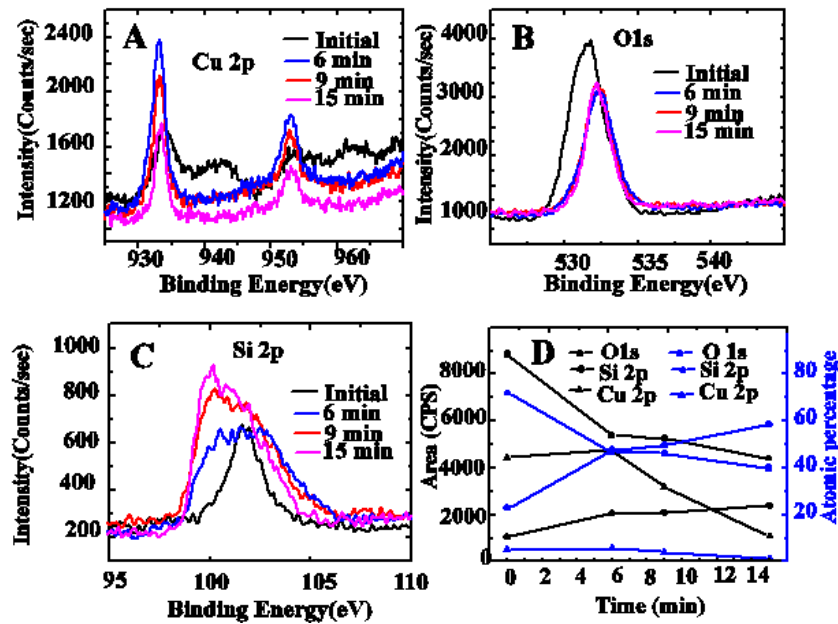
Figure 3.4: (A,B,C) High resolution XPS analysis of Cu 2p, O1s, Si 2p of Cu coated a-Si:H with 50% hydrogen content respectively for different time interval of Ar sputtering. (D) Plot of change in area and the atomic percentage of each element (Cu, Si and O) with different time interval of Ar sputtering.

54

To further understand the nature and formation of Cu_2O over the surface of Cu coated a-Si:H samples XPS Ar sputtering experiments were performed for different time intervals. Figure 3.4a shows the high resolution XPS analysis of Cu after different Ar sputtering times. The presence of Cu oxide is confirmed by the shift in binding energy from 930.8 to 933.4 eV for Cu $2p_{3/2}$ and 950.6 to 953.2 eV for Cu $2p_{1/2}$ along with the presence of satellite peaks at 942.3 and 961.3 eV. XPS analysis after 6 minutes of sputtering shows a shift in Cu $2p_{3/2}$ and Cu $2p_{1/2}$ to binding energy 930.8 and 950.6 eV for respectively, corresponding to metallic Cu. The oxide layer over the Cu is removed completely after 6 min, supported by analysis of the O 1s intensity profile remains constant further sputtering (Figure 3.4b). With an additional 3 minutes of sputtering time, nine total minutes, the thin layer of Cu is completely removed and the Cu peaks decrease in intensity coinciding with the relative growth in the Si 2p peak (Figure 3.4c). Figure 3.4d shows the observed changes in composition measured by XPS. These results confirm that a few layers of Cu undergo oxidation to form Cu_2O and the thickness of Cu on the surface of a-Si:H is about 10-15 nm (STEM and TEM measurements).

3.2.4 Results and Discussion: Electrochemical performance

3.2.4.1 Lithium Insertion in Bare a-Si:H Particles

a-Si:H particles of varying sizes were tested for electrochemical lithium insertion in coin cell assemblies against lithium. Figure 3.5 shows the specific capacity versus number of cycles at charging/discharging rates of 100 mA/g and 50 mA/g.
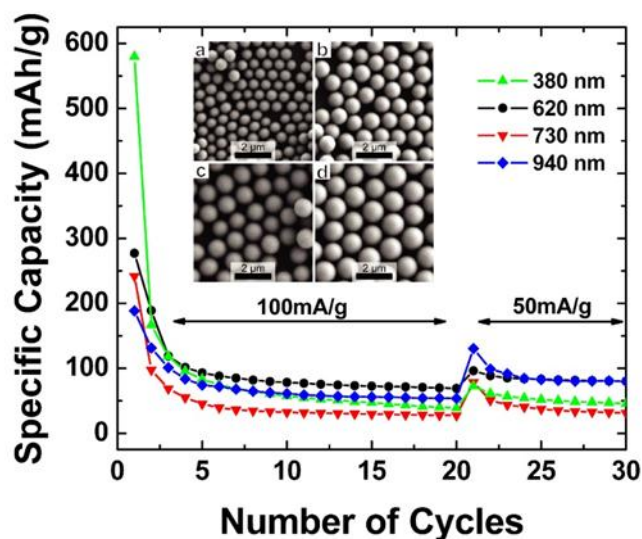
Figure 3.5: Plot of specific capacity vs. cycle number of different size a-Si:H particles (a) 380 nm, (b) 620 nm, (c) 730 nm and (d) 940 nm at the current rate of 100 mA/g and 50 mA/g. The inset figure shows the spherical a-Si:H particles in different sizes (a) 380 nm, (b) 620 nm, (c) 730 nm and (d) 940 nm synthesized by varying the initial trisilane concentration.

The smallest particles tested (380 nm diameter) showed a relatively high capacity of 580 mAh/g in the first cycle that dropped significantly to 165 mAh/g in the second cycle and then further to 40 mAh/g capacity in subsequent cycles at the current rate of 100mA/g. The capacities of particles of different sizes only differed by 10 to 20 mAh/g with no apparent size-dependence. The average capacity of the particles is limited to about 50 mAh/g at the current load of 100 mA/g. Lowering the current load to 50 mA/g did not improve the charge storage capacity. This storage capacity is quite low compared to the maximum storage capacity of 3579 mAh/g ($Li_{15}Si_4$composition) for Si.[5] The relative contributions to the charge storage capacity from the conducting carbon (Super-P) and a-Si:H were studied by preparing separate electrodes with 100% super-P and 100% a-Si:H. Figure 3.6 shows the galvanostatic charging/discharging behavior and the

incremental capacity (IC) plots of 100% a-Si:H particles and 100% graphitic (Super-P) carbon. In the galvanostatic experiment, the first lithiation curve of Super-P carbon shows the decomposition of electrolyte that takes place before the lithiation of graphite (Figure 3.6A). During lithiation, a plateau formed at 2.2 V that can be attributed to the lithiation of Super-P carbon. After the first cycle, this lithiation behavior remains constant for 20 cycles with a capacity of 150 mAh/g. The columbic efficiency remains almost 100% after the first cycle (data not shown). The lithium storage stabilization behavior after the initial lithiation cycle can be attributed to the beneficial role of the SEI layer. The incremental capacity plots are obtained by plotting dQ/dV (derivative of the state of charge with respect to potential) against the potential, V. This plot gives information about peak potentials of lithiation and delithiation process and the plateau in the galvanostatic cycling experiments. The incremental capacity plot (Figure 3.6B) also clearly shows the reduction peak of graphitic carbon at 2.2 V and the solvent decomposition peaks below 1.2 V. The a-Si:H particles without binder and carbon exhibited a maximum lithium storage capacity of only 3 mAh/g (Figure 3.6C). Curiously, this capacity was obtained on the 50th cycle, as the charge storage capacity increased with cycling. This may be attributed to the continual formation of SEI layers. The low lithiation capacity (3 mAh/g) can be attributed to poor conductivity of the individual a-Si:H particles, their large size, and high charge transfer resistance between particles. These results indicate that the minimal lithiation capacity observed in Figure 3.5 was primarily due to lithiation of carbon and not the a-Si:H particles. Figure 3.6D shows the incremental capacity plot of the 2nd and 50th lithiation/delithiation cycles for a-Si:H particles. For the 2nd cycle, there are no observable peaks. In the 50th cycle, there are clear peaks at 0.52 V, corresponding to lithium insertion of a-Si:H. This clearly demonstrates that SEI formation is different for Si versus carbon anodes.
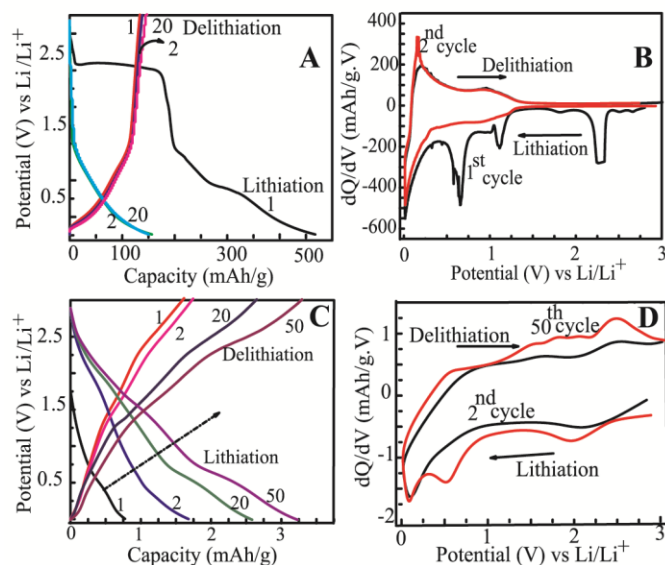
Figure 3.6: Galvanostatic charging/discharging behavior of pure graphitic super-p conducting matrix and 100% a-Si:H particles and their incremental capacity plots. (A) galvanostatic lithiation/delithiation of Super-P graphitic carbon for 20 cycles at the rate of 100 mAh/g. (B) Incremental capacity plot showing the first cycle (a) and second cycle of lithiation/delithiation process (b). (C) Galvanostatic lithiation/delithiation of a-Si:H particles for 50 cycles at the rate of 100 mAh/g. (D) Incremental capacity plot showing the second cycle (a) and 50th cycle of lithiation/delithiation process (b).

3.2.4.2 Lithium Insertion in a-Si@Cu Particles

The Cu-coated a-$Si_{0.75}H_{0.25}$ and pristine a-$Si_{0.75}H_{0.25}$ particles with 380 nm particle size were tested for long term stability at different charging/discharging rate in a single coin cell (2032) mode against lithium (Figure 3.7). The results are compared with the lithium charge storage capacity of graphite. The Cu-coated a-Si:H particles shows a specific charge storage capacity of 600 mA h/g at 100mA/g current load, which is nearly 7 times higher than that of pristine a-Si:H particles (84 mA h/g) and higher than that of commercial graphite anodes (372 mA h/g). Furthermore, the Cu coated a-Si:H particles did not lose capacity and degrade with successive cycling. It showed an increase in

58

charge storage capacity with increase in number of cycles. This may be attributed to the lithiation property of a-Si:H previously noted for pure a-Si:H particles (Figure 3.6C). At the effective C rate (rate required to charge/discharge a battery in 1 hr is 1C) of 0.23C, the anode showed a specific capacity of 600 mAh/g and upon increasing the rate to 1C it maintained a storage capacity of about 500 mAh/g for 10 cycles. The effective C rate is defined as $C = I_A/Q_{Exp}$ where I_A is the applied current (mAg^{-1}) and Q_{Exp} is the experimental capacity which is lower than the theoretical capacity $(Q_{Th} = 4200)$. A similar approach has been utilized for nanomaterials.[29]
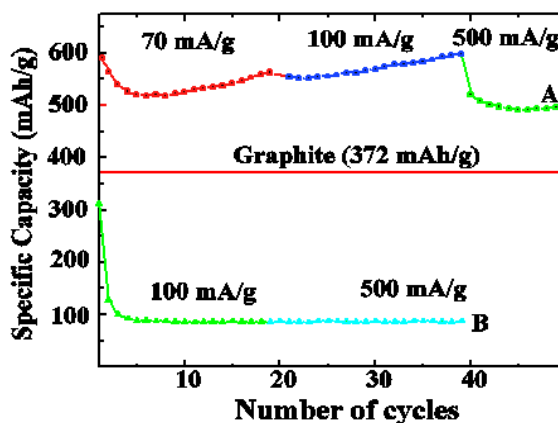
Figure 3.7: Long term stability of specific discharge capacity for: (A) Cu coated a-$Si_{0.75}H_{0.25}$ particles with a molar copper loading ratio of 50:1 a-Si:H : Cu, tested at current loads of 70, 100 and 500 mA/g was tested. (B) Pristine a-$Si_{0.75}H_{0.25}$ particles, tested at current loads of 100 and 500 mA/g. For both samples, composite anodes of test material, carbon super-P, and PVDF were used in a 70:20:10 ratios by weight. The charge storage capacity of graphite is given for comparison.

3.2.4.3 In Situ Raman Spectroscopy

In situ Raman spectroscopy was performed on Cu coated a-Si:H and pristine a-Si:H to understand the role of Cu in the electrochemical lithiation/delithiation process. In situ Raman spectroscopy has been used to study phase changes in crystalline Si/carbon composite electrodes.[30] In those experiments, the Si peak disappeared when the lithium

alloy formation potential window of 0.45 V to 0.2 V was reached, which was attributed to the passivation of the Si surface by lithium.[30-31] Due to this loss of peak intensity, the experiment could not be continued to gather more information on the system. In our experiments, the phase change from crystalline to amorphous Si during electrochemical alloying was avoided by starting with a-Si:H particles.
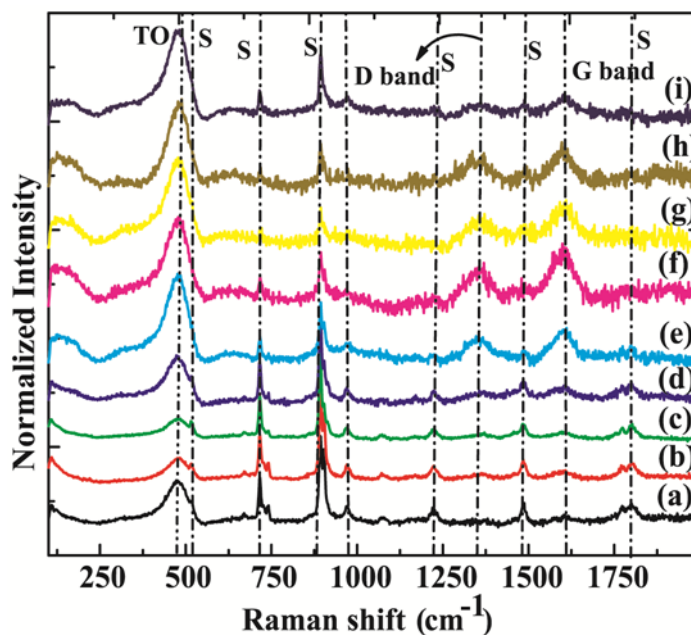
Figure 3.8: *In situ* Raman measurements of a-Si:H particles with the electrode composition of 70:20:10 of active a-Si:H, conductive carbon Super-P, and binder PVDF. TO is the phonon mode of a-Si:H and S represents the solvent peaks. D and G band corresponds to the conductive carbon present in the electrode. The Raman signatures were measured at different potentials during the charging and discharging process corresponding to: (a) initial, (b) 2 V, (c) 1.2 V, (d) 0.65 V, (e) 0.57 V, (f) 0.35 V, (g) 0.1 V, (h) 2nd cycle lithiation 0.19 V (i) 2nd cycle delithiation 0.58 V.

In general, it is difficult to characterize amorphous materials by standard techniques such as XRD and HR-TEM. Raman spectroscopy, however, is well-suited for these

experiments as a-Si has a large Raman cross section with a peak around 475 cm^{-1}, corresponding to the phonon mode (TO) of amorphous Si.[31-32]

In situ Raman spectra were acquired in coin cell mode for 10 s at 50% laser power over 5 acquisitions to achieve a high signal to noise ratio. The electrodes were prepared as described previously with a 70:20:10 active material: super-P: PVDF ratio by weight. This preparation provided a reasonable Raman signature with good signal to noise ratio and no sintering effect (Figure S1). Figure 3.8 shows in situ Raman spectra acquired for an a-Si:H battery composite electrode for the first three charge / discharge cycles. The Raman peak at 475 cm^{-1}, corresponding to a-Si, shows no change as a function of applied potential. In contrast, there are significant changes in Raman scattering intensity at 1600 cm^{-1}, corresponding to the G-band of graphitic carbon, similar to previous reports on lithiation and delithiation in carbon anodes.[33] This illustrates that the lithiation capacity in bare a-Si:H composite electrodes is mainly due to the lithiation/delithiation of the carbon added during the electrode preparation, and that the Si is not being lithiated. There are also subtle changes in Raman modes associated with the ethylene carbonate solvent, suggesting the formation of SEI on the surface of the carbon during cycling. This SEI formation is commonly observed in graphite anode electrodes due to decomposition of the solvent (1M LiPF$_6$ in EC: DEC).[34]
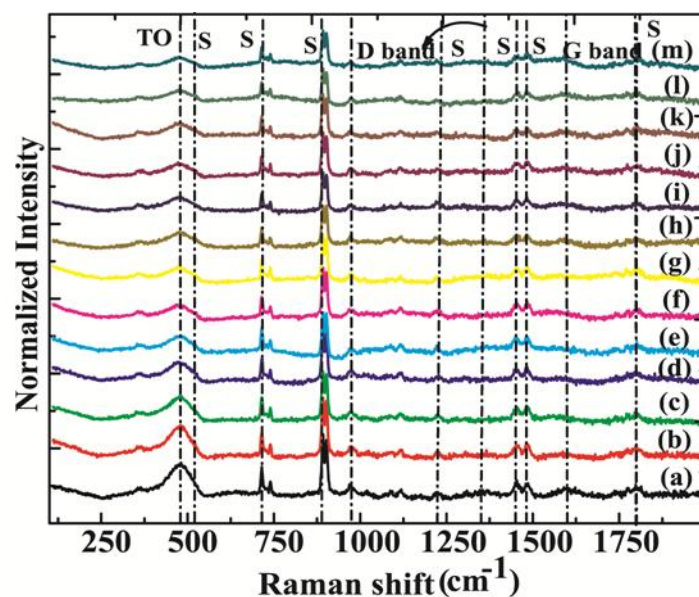
Figure 3.9: *In situ* Raman spectra of copper coated a-Si:H particles while charging/discharging at 100 mAh/g. TO is phonon mode of a-Si:H and S represents the solvent peaks. D and G band corresponds to the conductive carbon present in the electrode. The Raman signatures were measured at different potentials during the charging and discharging process simultaneously corresponding to: (a) initial, (b) 0.42 V, (c) 0.12 V, (d) 0.08 V, (e) 0.07 V, (f) 0.03 V, (g) delithiation 0.29 V, (h) delithiation 0.56 V, (i) 2nd cycle lithiation 1.69 V, (j) 2nd cycle lithiation 1.52 V, (k) 2nd cycle delithiation 0.53 V, (l) 2nd cycle delithiation 1.46 V, and (m)2nd cycle delithiation 2.66 V.

Figure 3.9 shows *in situ* Raman spectra for an electrode composed of the Cu-coated a-Si:H particles. As opposed the pristine a-Si:H electrode, there is a change in the peak signature at 475 cm^{-1}(amorphous Si TO mode). To further understand this change, we have analyzed the peak intensity, full width half maximum (FWHM), and peak area of the amorphous Si peak at 475 cm^{-1} (Figure 3.10A). The peak intensity, FWHM and peak area decreases during the lithiation process, as expected. This demonstrates that Cu coated a-Si particles are reversibly alloying with lithium. Similar results were obtained for a-Si lithiation through ex-situ Raman measurements.[31] It is also worth noting that

there is not much change in either the graphic carbon G-band mode at 1600 cm^{-1} or the Raman modes associated with the solvent, suggesting that the Cu coating suppresses decomposition of solvent.
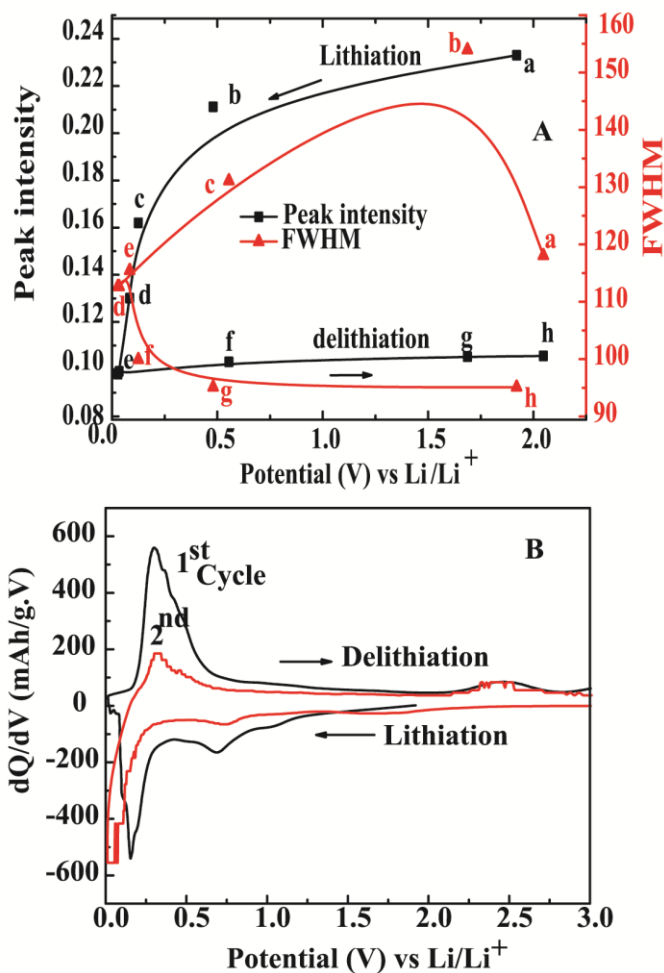
Figure 3.10: (A) Quantitative in situ Raman analysis of Cu coated a-Si:H particles, during the first charging/discharging cycle based on the amorphous Si (TO mode) at 475 cm^{-1}. (B). Incremental capacity plot of Cu coated a-Si showing the lithiation/delithation potentials. Where (a) initial, (b) 0.42 V, (c) 0.12 V, (d) 0.08 V, (e) 0.07 V, (f) 0.03 V, (g) delithiation 0.29 V, (h) delithiation 0.56 V.

Figure 3.10B shows the corresponding incremental plot of galvanostatic charging/discharging in Cu coated a-Si:H particles that was simultaneously acquired while running in situ Raman. The peaks present in the first cycle at the potentials 0.69 V and 0.15 V are attributed to the lithiation potential of a-Si:H particles, with no other significant peaks present. A small peak at 1.03 V may be attributed to lithiation of conducting carbon with SEI formation, but the relative amount of lithiation by the carbon is relatively small compared to the pristine a-Si:H particles composite electrode. The delithiation peak at 0.29 V confirms reversible lithiation with Cu coated a-Si:H particles. This further shows that the Cu coated a-Si:H particles are lithiated while the lithiation of carbon and decomposition of solvent are suppressed by the presence of the Cu coating. This is confirmed in the second cycle by the loss of 1.03V peak due to carbon lithiation and SEI formation. Likewise, in the second cycle, the lithiation potential has been shifted towards 0.73 V from 0.65 V suggesting easier lithiation in subsequent cycles. Recently, studies by Oumellal *et al.*, showed that a major portion of the lithium lost during the charging of Si anodes is associated with SEI formation, causing large contact resistance due to loss of particle to particle contact. These results were supported by SEM and electrochemical impedance spectroscopy (EIS) analysis.[35] Earlier reports have also shown that the capacity fade of Si anodes is due to the loss of electrical conductivity.[36] In this report, we have prepared a-Si:H particles coated with Cu that acts as an electronic "wiring" to prevent the loss of electrical conductivity and suppress decomposition of solvent over the a-Si:H particles, thereby overcoming failures in the lithiation/delithiation process.

3.2.5 Summary

A unique chemical process to coat Cu over pre synthesized a-Si:H particles has been developed. The hydrogen content in the a-Si:H plays a significant role in the Cu

coating process. These Cu coated a-Si:H particles exhibited significantly enhanced lithium storage capacity over pristine a-Si:H particles of about 7 fold. The presence of Cu helps to suppress the solvent decomposition and enhance electrical wiring between the particles. *In situ* Raman measurements elucidate the fundamental nature of the lithiation/delithiation process taking place in a-Si:H particles and the role of the Cu layer in these processes. This chemical approach of coating Cu over a-Si:H particles shows great potential towards developing material for lithium ion battery.

3.3 ENHANCED CONDUCTIVITY AND LITHIATION OF BARE SILICON NANOWIRE FABRIC[§]

3.3.1 Introduction

Solvent-based processes for nanowire synthesis, like supercritical fluid-liquid-solid (SFLS) and solution-liquid-solid (SLS) growth, can produce large amounts of Si nanowires at relatively low cost.[55-42] In a 10 mL laboratory-scale reactor, hundreds of milligrams of nanowires with lengths over 100 μm can be produced in a few hours,[55,41] which is sufficient to create nanowire-based non-woven fabrics of several inches on a side.[42] These nanowires exhibit excellent mechanical properties, are highly flexible, and have strength-to-weight ratios greater than both carbon fiber and Kevlar.[42,44] This fabric material is thin—ranging from about 50 – 150 μm thick—and has a paper-like appearance and feel. The first fabrics consisting entirely of one-dimensional nanomaterials were made from carbon nanotubes due to their mechanical strength, flexibility, large aspect ratio, and the ability to produce the material in macroscopic quantities.[45,46] Metal oxide nanowires that can easily be synthesized in large quantities by simple hydrothermal methods have also been formed into macroscopic membranes.[47] Group IV nanowires have only recently been synthesized in large enough quantities to

---

[§] Portions of this section appear in *Journal of the American Chemical Society*, **2011**, *133*, 20914.

form free-standing fabrics.[42, 48] Fabric-like materials of carbon nanotubes (CNT) and graphene sheets have been recently explored as electrodes for flexible LIB applications,[43, 51, 50-54] and as electrode supports for other materials, as in graphene-silicon,[43, 54] CNT-SiNW,[51, 50] and CNT-Li$_4$Ti$_6$O$_{12}$[51, 52] electrodes. Here, we demonstrate that a Si nanowire fabric can function as a stand-alone anode material without the need for additional conductive fillers (activated carbon) or polymeric binders. For good battery performance, it was necessary to convert a thin polyphenylsilane[55] coating on the Si nanowires to carbon by annealing under forming gas (7% H$_2$ in N$_2$) at 900°C. This thin layer provides the necessary electrical conductivity for efficient Li$^+$ charging and discharging of the layer. Here, we report the LIB performance of the Si nanowire fabric and the role of the shell on the cycling behavior.

3.3.2 Experimental Section

3.3.2.1 Reagents

All chemicals were used as received, without further purification. Dodecanethiol (DDT, ≥98%), tetrachloroaurate trihydrate (≥99.9%), sodium borohydride (≥98%), toluene (ACS grade and anhydrous, 99.8%), ethanol (99.9%), tetraoctylammonium bromide (TOAB, 98%), and chloroform (99.8%) were purchased from Sigma Aldrich. Monophenylsilane (MPS, >95%) was obtained from Gelest, and LiPF$_6$ (1.0M in a 1:1 mixture of ethylcarbonate [EC>99.95%]: diethyl carbonate [DEC>99.98%]) was purchased from Novolyte. For battery assembly, Celgard 2400 membranes (25μm) were used as separators, purchased from Celgard, and Li metal (99.9%) from Alfa Aesar.

3.3.2.2 Synthesis of Si Nanowires

Si nanowires were synthesized by gold nanocrystal-seeded supercritical fluid-liquid-solid (SFLS) growth in toluene using the synthetic procedures detailed in previous

reports[55]. Briefly, MPS and 2nm Au nanoparticles[56] are mixed together in a 290:1 Si:Au mole ratio and diluted with anhydrous toluene to achieve an MPS concentration of 156 mM. Nanowires are then grown in a flow-through sealed titanium reactor at 490°C and 10.3 MPa. After the reaction, the nanowires are collected from the reactor walls and washed with chloroform (10mL) and ethanol (5mL) several times via centrifugation at 8,000 rpm. Nanowires are then dispersed in chloroform to a concentration of 5mg/mL and stored in a vial under ambient conditions prior to use.

3.3.2.3 Construction of LIB Anode and Electrochemical Testing

Si nanowire fabric was prepared by sonicating nanowire dispersions (5-10 mg/mL Si nanowires in chloroform) for 1 hour. The dispersions were drop cast into a Teflon trough and left overnight to dry. After drying, the fabric is peeled from the trough using tweezers and a thin razor blade wedged between the fabric and trough bed when necessary and cut into 1cm x 1cm squares that were loaded into quartz boats and heated under a moderate flow of forming gas in a tube furnace.

Batteries were prepared within an argon-filled glovebox using a Cu foil current collector. The Si nanowire fabric was placed on the Cu current collector to serve as the anode material. The electrolyte was a 1.0 M solution of $LiPF_6$ in a 1:1 mixture of ethylcarbonate : diethyl carbonate (EC>99.95%, DEC>99.98%, Novolyte). A few drops of electrolyte were deposited over the nanowire fabric. A Celgard 2400 separatror membrane (25μm thick, Celgard) was then added followed by Li metal (99.9%, Alfa Aesar) foil as the counter electrode. Galvanostatic measurements were made using an Arbin BT-2143 test unit that was cycled between 3V and 10mV vs Li/Li$^+$ at a rate of C/20 (C = 3579 mA h/g[58-60]).

After cycling, the batteries were disassembled and the anode cleaned by soaking the fabric in acetonitrile overnight followed by a rinse with 0.5 M sulfuric acid for 1 minute (i.e., until bubbling subsided). The anode was then placed in a vial and soaked in isopropanol for several minutes. The IPA was decanted and the anode was soaked two more times in the same way and then dried in air before SEM and TEM imaging.

3.3.2.4 Materials Characterization

Scanning electron microscopy (SEM) images were acquired using a Zeiss Supra 40 SEM with an in-lens arrangement, a working voltage of 5 keV and a working distance of 5 mm. SEM samples were imaged silicon wafers (S.E.H). Transmission electron microscopy (TEM) images were digitally acquired using a either a FEI Tecnai Spirit BioTwin TEM operated at 80 kV or a field emission JEOL 2010F TEM operated at 200 kV. TEM samples were prepared by drop-casting from chloroform dispersions onto 200 mesh lacey-carbon copper TEM grids (Electron Microscopy Sciences).

X-ray diffraction (XRD) was carried out using a Rigaku R-Axis Spider Diffractometer with Image plate detector with Cu-k$_\alpha$ ($\lambda = 1.5418$ Å) radiation operated at 40 kV and 40 mA. Measurements using were taken on samples on a 0.5 mm nylon loop. Samples were scanned for 10 min while rotating at 1° per second under ambient conditions. The radial data were integrated from 20 to 80 2θ and plotted. Background scattering from the nylon loop was subtracted from the sample measurement.

X-ray photoelectron spectroscopy (XPS) was performed on a Kratos photoelectron spectrophotometer with monochromatic Al Kα radiation (1487 eV). The Si nanowire fabric was secured on the experimental tray using double sided Cu tape. Spectra were collected at 0.1 eV intervals and 800 ms integration time through a tungsten coil set at 4.8 V bias with respect to the sample. Data were collected continuously under

high vacuum (10^{-9} torr). The effect of sample charging on the XPS data was corrected by shifting the Si^0 $2p^3/_2$ peak to a binding energy of 99.3 eV.

XPS results were analyzed using CasaXPS software. Background subtraction was done using a Shirley background model. Peak areas were deconvoluted as Voigt functions (30% Gaussian character). The Si 2p region was deconvoluted as Si^0 $2p_{3/2}$, Si^0 $2p_{1/2}$, Si^{+1}, Si^{+2}, Si^{+3} and Si^{+4} peaks were placed at 99.3 eV, 99.9 eV, 100.1 eV, 101.1 eV, 102.1 eV and 103.2 eV, respectively. Zero-valent Si spin splits were assumed to have the same FWHM and the area of the $2p_{1/2}$ was set as half the area of the $2p_{3/2}$. Similarly, one FWHM value was used for all the other oxide peaks; however, for simplicity other oxidative states were not divided into their respective spin splits. Values for the FWHM of the oxidized states were constrained by placing the FWHM between 1.8X and 2.2X of the zero-valent peaks.

The C1s region was deconvoluted into three peaks placed at 284 eV, 284.7 eV and 285.5 eV. These binding energies correspond to Si-C, C-C and C-O bonding, respectively. The O1s region was deconvoluted into two peaks. A first peak placed at 532.5 eV corresponding to SiO_2 and C-O bonding. A second peak placed at 533.9 eV relates to adsorbed O_2 on the surface of the wires. Only one FWHM of was used to generate the peaks for each species of C and O.

Raman spectroscopy was performed using a Renishaw inVia microscope equipped with a 514.5 nm Argon laser in backscattering configuration. The Stokes Raman signal at 521 cm^{-1} for single crystalline bulk Si oriented with the [110] direction normal to the laser was used to calibrate the instrument. The beam was focused using an optical microscope with a 50x objective lens. Spectra were taken on freestanding sheets of nanowire fabric lying on glass slides by single scans from 100-2000 cm^{-1} at 5% (0.2 mW) laser power.

3.3.3 Results and Discussion

3.3.3.1 Si Nanowire Fabric

Figure 3.11 shows a photograph and SEM images of Si nanowire fabric made by casting concentrated dispersions of SFLS-grown nanowires in toluene into a Teflon trough. The fabric is composed of highly entangled nanowires.
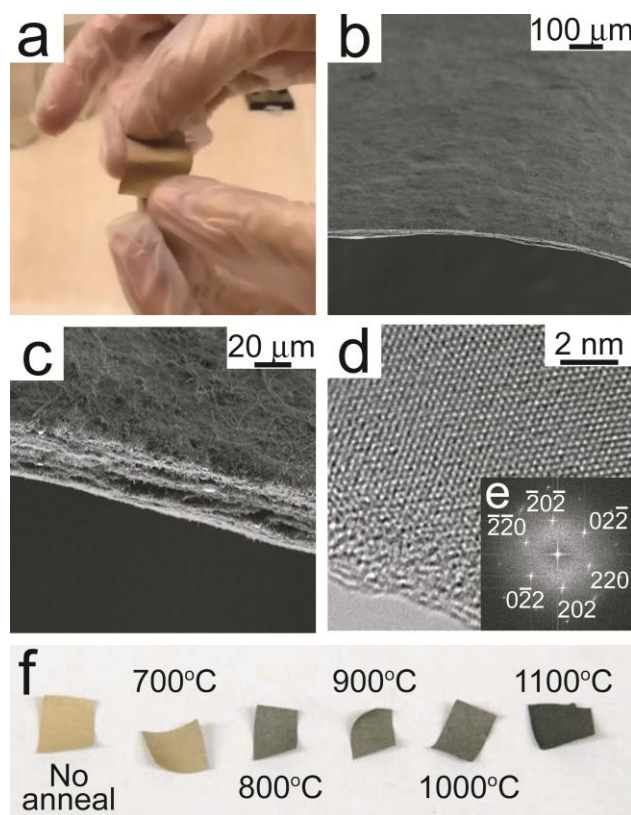
Figure 3.11: (a) Photograph of mechanically flexible Si nanowire fabric. (b,c) SEM images of the fabric. (d) High resolution TEM image of a Si nanowire showing its crystallinity. (e) FFT pattern from the TEM image in (d) shows a <110> growth direction. (f) Photographs of Si nanowire fabrics annealed at the indicated temperature under reducing atmosphere.

It is about 50 μm thick and relatively porous containing approximately 90% void volume. The Si nanowire fabric is pliable with good mechanical integrity. Even though the

nanowires are single crystals of a material (i.e., Si) that is brittle in bulk form, they are mechanically flexible and strong due to their narrow diameter.[62]

3.3.3.2 Electrochemical performance of Si nanowire fabric anodes in LIBs

1cm x 1cm squares of Si nanowire fabric were tested as stand-alone Si-based anode materials without added carbon binder for a LIB. The as-made Si nanowire fabric with no added carbon binder performed poorly. As shown in Figure 3.12, the initial capacity on the first cycle was just under 600 mAh/g, but then dropped to nearly zero capacity after only a couple of cycles. Tests of the electrical conductivity showed that the nanowire fabric is electrically insulating with a conductivity of about 0.2 nS/m. The nanowire fabric needs to be sufficiently conductive to facilitate efficient lithium alloying with Si.[57]
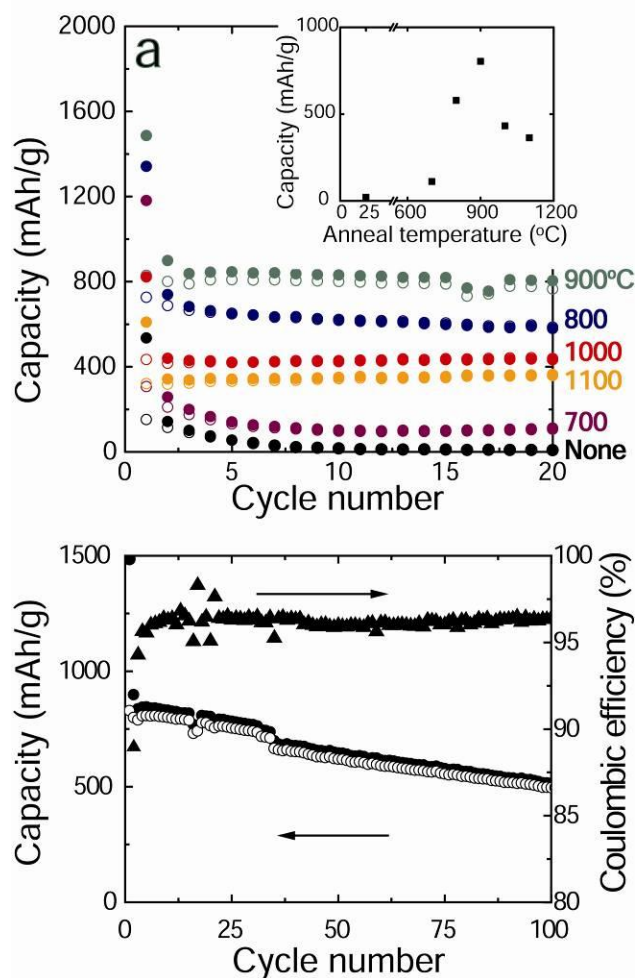
Figure 3.12: (a) Galvanostatic cycling tests of Si nanowire fabric before and after annealing at 700°C, 800°C, 900°C, 1000°C, and 1100°C a cycle rate of C/20 (C = 3579 mA h/g[5, 6]). (a, inset) Discharge capacities after 20 cycles for batteries with nanowire fabric anodes annealed at various temperatures. (b) Galvanostatic cycling of a Si nanowire fabric anode annealed at 900°C.

The electrical conductivity of the Si nanowire fabric was enhanced significantly by annealing under reducing atmosphere at temperatures greater than 700°C. Figure 3 shows current-potential (I-V) curves for nanowire fabric annealed at various temperatures.   Annealing at temperatures between 700°C and 1000°C led to

conductivities ranging from 70 to 150 nS/m. Fabric annealed at 1100°C had a conductivity of 1400 nS/m.
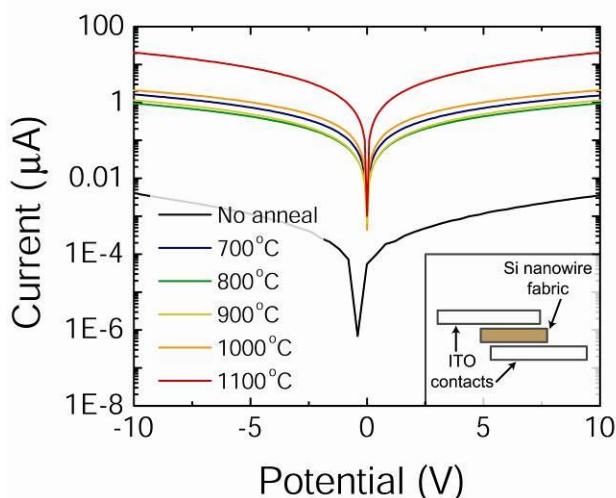
Figure 3.13: Current-potential measurements of Si nanowire fabric placed between two ITO electrodes (inset). The nanowire fabric was annealed under reducing atmosphere at the indicated temperatures. Measurements were made using fabric samples approximately 150 μm thick with a contact area of 1 cm^2.

Figure 3.11f shows photographs of Si nanowire fabric after annealing under forming gas at various temperatures. The fabric turns increasingly black with higher annealing temperature. The Si nanowires produced by the SFLS process using phenylsilane as a reactant have a thin polyphenylsilane shell on their surface.[55] Annealing under a reducing environment transforms this shell material to carbon, which provides the significantly enhanced electrical conductivity. When the nanowires are annealed in the presence of oxygen and water, the shell material oxidizes to a defective and insulating SiO_2 layer.

The annealed Si nanowire fabric performed well in galvanostatic cycling tests. Figure 3.12a shows the capacity, cycling at a C/20 rate (where C= 3579 mA h/g,

corresponding to $Li_{15}Si_4$[58-60]), for Si nanowire fabric annealed (under reducing atmosphere) at various temperatures. All of the nanowire samples exhibited the large initial irreversible capacity loss during the first cycle, which is typical for Si anode materials due to formation of solid electrolyte interphase (SEI) layers when cycling to low potentials. The nanowire fabric annealed to 700°C performed better than the as-made nanowires, but the capacity was still very limited. Nanowires annealed at 900°C on the other hand performed quite well and retained a cycling capacity of 800 mAh/g after 20 cycles. As shown in Figure 3.12b, the capacity was still higher than 500 mAh/g after 100 cycles. Once the nanowires were annealed at even higher temperature (> 900°C), they did not perform as well. The inset in Figure 3.13a plots the charge and discharge capacities after twenty cycles for Si nanowire fabric electrodes annealed at various temperatures.

	Capacity (mAh/g)			Retention (%)	
Temperature (°C)	1st Cycle	2nd Cycle	20th Cycle	C_{ret1} §	C_{ret2} †
No anneal	534	142	8	2	6
700°C	1180	257	111	9	43
800°C	1341	738	579	43	78
900°C	1485	898	804	54.0	89
1000°C	821	439	433	57	99
1100°C	608	341	363	60	106

Table 3.1: Summary of the capacity retention Si nanowire fabric anodes annealed at the indicated temperatures. §Amount of charge capacity retained after 20 cycles compared to the first charging cycle. †Amount of charge capacity retained after 20 cycles compared to the second charging cycle.

The highest performance was achieved from nanowires annealed at 900°C. Table 3.1 summarizes the capacity retention data of the Si nanowire fabric annealed at various temperatures.

Figure 3.14 shows the constant current voltage profiles and differential capacity curves for the first and twentieth cycles of batteries with Si nanowires annealed at 800°C, 900°C, 1100°C and 1100°C. Each constant current voltage profile shows two plateaus during the charge cycle corresponding to the lithiation of crystalline silicon and the formation of the $Li_{15}Si_4$ phase.[59] The discharge cycles have a steeper slope than the charging cycles (corresponding to a broader peak in the differential capacity curves), indicating that delithiation occurs over a relatively broad range of potential, which is consistent with amorphous silicon. The corresponding differential plots provide a better illustration of the potentials at which the lithiation and delithiation events occur. Each of the first cycle charge curves in the differential (dQ/dV) plots show a peak between 150 and 200mV corresponding to lithiation of crystalline Si. This peak is shifted slightly in the 900°C sample (Figure 3.14d) to around 250mV. A peak near 50mV is also observed for each sample and is attributed to the formation of $Li_{15}Si_4$.[59] By the 20th cycle, the first lithiation event has shifted to around 300mV, which falls in the range expected for lithiation of amorphous Si (a-Si).[51] The second lithiation event has significantly reduced intensity indicating a marked consumption of crystalline silicon. The first discharge cycle shows a prominent peak at around 450mV, which corresponds to the delithiation potentials of amorphous silicon and $Li_{15}Si_4$.[51] Lithium extraction during the 20th cycle occurs at the a-Si delithiation potential (300mV)[51].
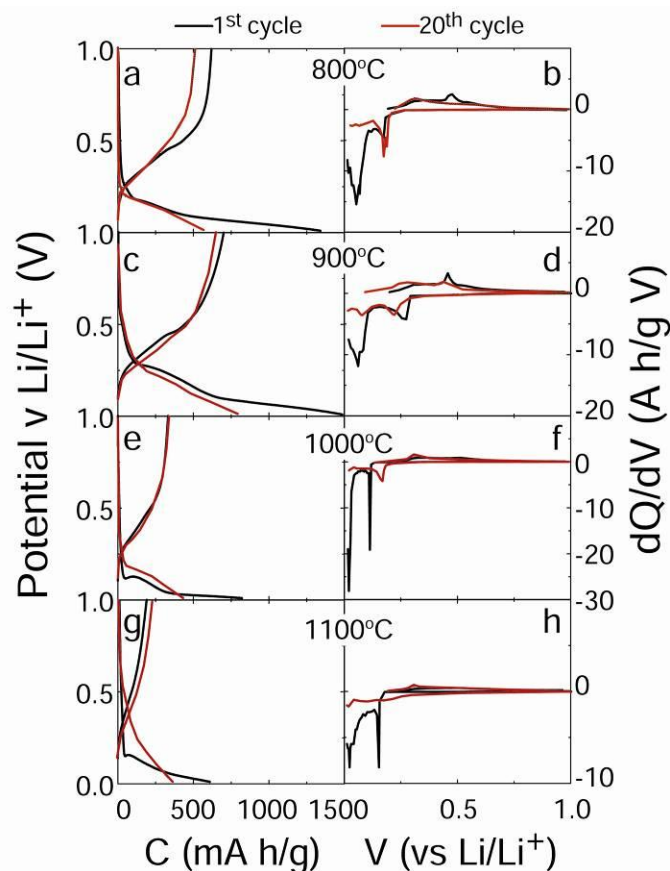
Figure 3.14: Constant current voltage profiles for Si nanowire fabric anodes annealed at (a) 800°C, (b) 900°C, (c) 1000°C and (d) 1100°C with corresponding differential capacity curves (b, d, g, and h, respectively)

3.3.3.3 Composition of the carbonaceous shell on the Si nanowires.

Raman and X-ray photoelectron spectroscopy and X-ray diffraction were used to determine the composition of the shell material formed after annealing the nanowires under forming gas. Figure 3.15 shows Raman spectra of nanowires as-made and after annealing at various temperatures. The as-made nanowires exhibit the characteristic Si (TO) band at 521 cm^{-1} along with a smaller peak at 495 cm^{-1} that is most likely related to stacking faults.[55,56] After annealing at 700°C, the nanowire spectra still have the characteristic Si-related peaks, but there is a significant sloping baseline due to

fluorescence from the sample. This fluorescence is due to a chemical change in the shell material that is probably related to the phenyl species. As the annealing temperature was increased, the fluorescent signal diminished in intensity. Nanowires annealed at 900°C and above had almost no fluorescent background. The nanowires annealed at 800°C and higher exhibited two prominent bands at ~1350cm^{-1} and ~1600cm^{-1} corresponding to disordered (D) and graphitic (G) carbon.[61-64] These peaks are not present in the Raman spectra of the as-made nanowires nor in the spectra of the nanowires annealed at 700°C. It appears that the fluorescent species formed as a result of annealing at 700°C is converted to the carbon that forms at higher annealing temperatures.
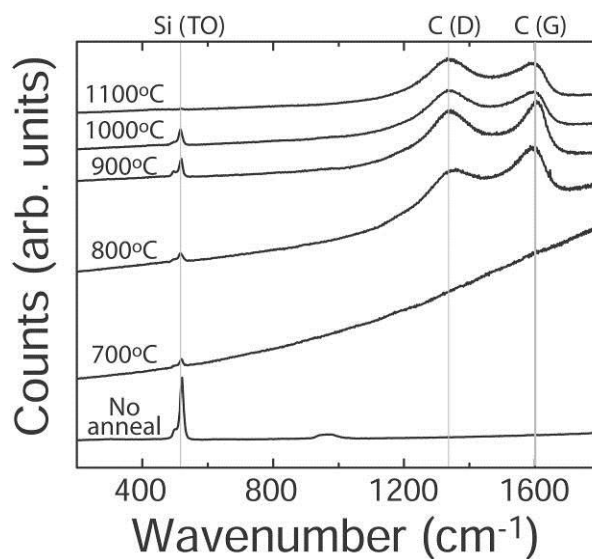
Figure 3.15: Raman spectra of Si nanowire fabric before and after annealing under reducing atmosphere at various temperatures. The Si (TO) peak at 521cm^{-1} and carbon-related D and G bands at 1380 cm^{-1} and 1560 cm^{-1} are labeled.

The much improved battery performance of the Si nanowire fabric after annealing results from the formation of the electrically conductive carbon layer on the nanowires. It is obvious from the changing color of the nanowire fabric from its typical pale yellow

77

color to black that the shell material has been converted to carbon, as confirmed by the Raman spectra. But why does the battery performance diminish when the nanowires are heated above $900^{o}C$? The Raman spectra show that the same carbon species that helped to achieve good battery response are still present on the nanowires annealed at $1000^{o}C$ and $1100^{o}C$, and the electrical conductivity of the nanowires is also high (Figure 3.13). However, XPS and XRD revealed that there was a significant amount of Si oxidation and some SiC formation when the nanowires were annealed at these higher temperatures. XRD (Figure 3.18) showed that the nanowires were still composed predominantly of crystalline Si after annealing, indicating that the oxidation and carbide formation was occurring only on the nanowire surface. It appears that residual oxygen or water, most likely contained initially in the polyphenylsilane shell, is oxidizing the surfaces of the nanowires. Nanowires annealed at $1100^{o}C$ no longer have a measureable Si^0 XPS peak and all of the Si signal corresponds to either Si^{4+} or Si^{2+}. XRD also indicates that some of the surface carbon reacts with the underlying Si to form SiC. The SiC diffraction peaks are very broad, indicating that crystalline SiC domains are extremely small, which is consistent with the lack of SiC-related Raman signal at 790 cm^{-1}.[66] The Si^0 signal does not show up in XPS or the Raman spectra because the surface layer becomes too thick to penetrate. Additionally, XPS (Figures 3.16 and 3.17) showed a noticeable decrease in relative carbon signal in XPS, along with the appearance of a relatively strong XPS signal at higher binding energy of 285.5 eV, indicating that the carbonaceous layer has also oxidized to some extent.
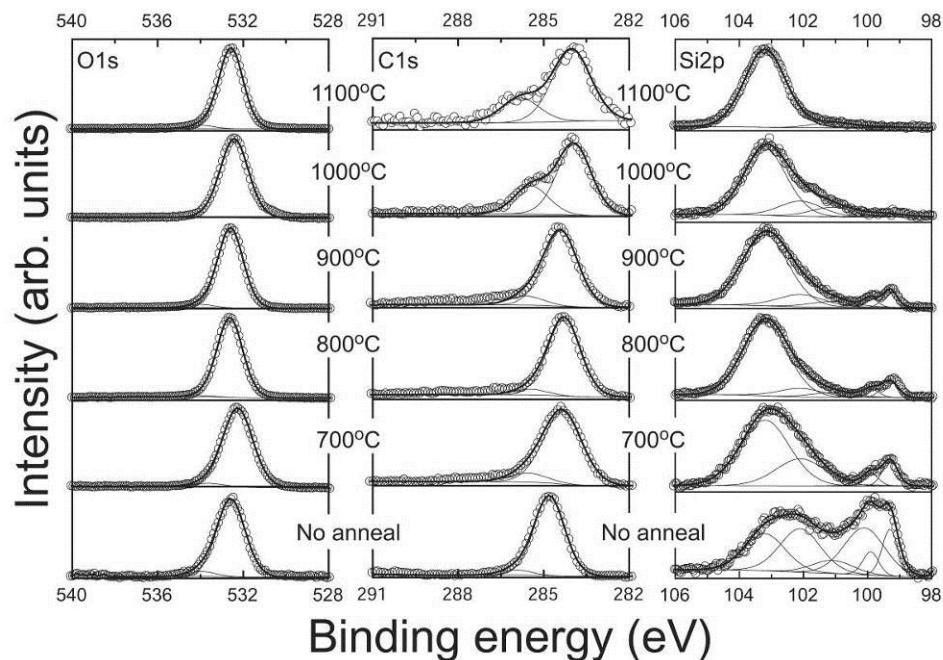
Figure 3.16: XPS data of O1s, C1s and Si2p states of Si nanowire fabric annealed at the temperature indicated. The intensities of all of the peaks are normalized, but the carbon signal decreased significantly relative to the Si signal as the annealing temperature was raised. Figure 7 plots the relative amounts of O, C and Si obtained from integration of the XPS peaks. The peak fitting procedures are described in the Experimental Section.
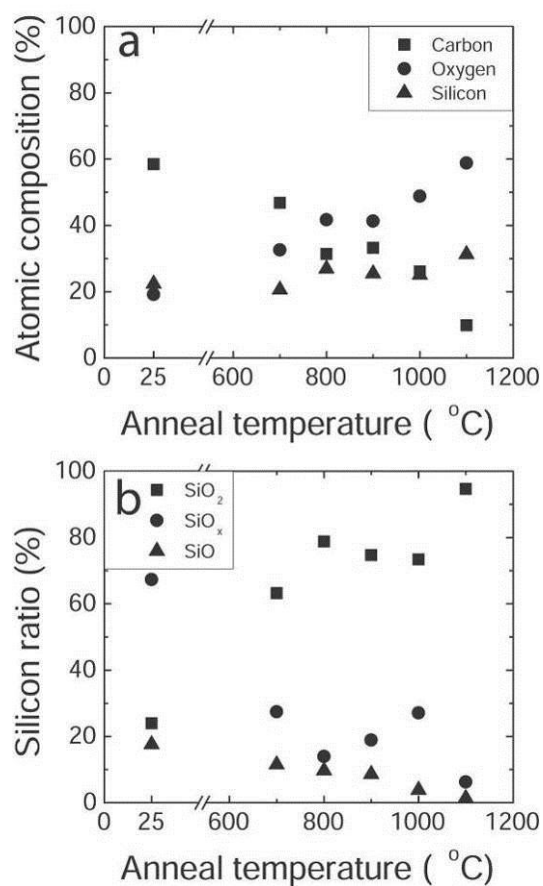
Figure 3.17: Summary of compositional analysis extracted from the XPS data in Figure 6: (a) relative Si, C, and O content determined by integrating the O1s, C1s and Si2p peaks; (b) relative SiO, SiO_x, SiO_2 content determined from the Si2p peak structure.
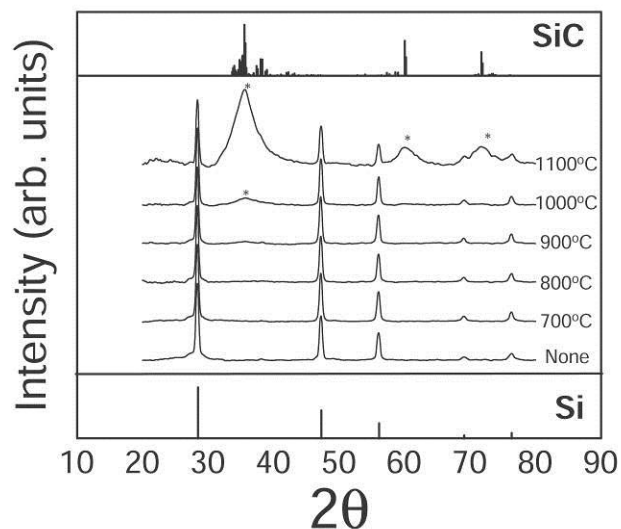
Figure 3.18: XRD of Si nanowire fabric before and after annealing at the indicated temperatures under forming gas. The peak positions corresponding to diamond cubic Si (JCPDS: 00-027-1402) and silicon carbide (SiC, labeled '*'. JCPDS: 00-029-1131) are shown.

The oxide and SiC that forms at the nanowire surface after annealing at 1000°C and 1100°C is most likely responsible for the reduced lithiation/delithiation of the nanowire fabric. SiC is known to be electrochemically inactive for lithiathion.[67] And the oxide layer creates an electrically insulating barrier between the Si core and the electrolyte that is not conducive to battery performance.

3.3.4 Summary

A non-woven fabric of Si nanowires is reported. The fabric has the look and feel of tissue paper, yet is composed entirely of crystalline Si. Annealing the nanowire fabric at 900°C under reducing atmosphere (forming gas) led to good performance as an anode in a Li ion battery without adding carbon binder. The key to their good performance is the presence of a thin electrically conductive carbon layer on the nanowires. When the nanowires were annealed above 900°C, the battery performance diminished due to the

formation of a surface barrier layer of SiO_2 and SiC under the conducting carbonaceous coating that prevented efficient lithitation and delithiation.

This study shows that surface composition of Si nanowires plays a critical role in their effectiveness as an anode material in a LIB. Si nanowires can alloy with lithium, but their capacity and cycling stability all rely on the quality of the surfaces. In this case here of Si nanowires grown by the SFLS process with monophenylsilane as a reactant, a residual polyphenylsilane shell can be converted from an inactive layer to a coating that enables Si nanowire lithiation/delithiation. The coating is conformal and uniform and does not require a separate materials deposition step. Carbon binder, which would lower the specific capacity of the material, need not be added. This Si nanowire fabric represents a mechanically-flexible silicon anode material with the potential to be applied in light-weight paper-based or plastic LIBs.

3.4 CONCLUSIONS

Cycle life and lithiation capacity of Si nanostructures can be greatly improved by enhancing their surface conductivity. Two methods for enhancing this conductivity were presented. a-Si:H particles initially showed low capacity for lithiation as an anode material. Cu nanoparticles were synthesized on the surface of the a-Si:H particles by a hydrogen enhanced reduction of Cu acetate. The lithiation capacity of a-Si:H particles increased from 84 mA h/g to 600 mA h/g, a seven-fold increase, after addition of Cu nanoparticles,. Though still not near the theoretical maximum capacity of Si, the large increase seen after increasing the surface conductivity of the particles is promising and applicable to other systems.

A free standing fabric of MPS grown Si nanowires was formed and utilized as an anode material for LIBs without the addition of conductive carbon or binder. The fabric

was initially nonconductive, but after annealing under a reducing atmosphere the conductivity increased greatly. The anneal reduced the polyphenylsilane shell on the surface of the wires into conductive carbon, creating a uniformly distributed conductive matrix that was chemically attached to the wire surfaces. This increased the lithiation capacity of the wires after 20 cycles from 8 mA h/g (unannealed) to 804 mA h/g (900 $^{\circ}$C anneal) – an amazing 100-fold capacity increase.

3.5 REFERENCES

(1)　(a) Tarascon, J. M.; Armand, M. *Nature* **2001,** *414* (6861), 359-367; (b) Armand, M.; Tarascon, J. M. *Nature* **2008,** *451* (7179), 652-657.

(2)　Mohri, M.; Yanagisawa, N.; Tajima, Y.; Tanaka, H.; Mitate, T.; Nakajima, S.; Yoshida, M.; Yoshimoto, Y.; Suzuki, T.; Wada, H. *J Power Sources* **1989,** *26* (3-4), 545-551.

(3)　Boukamp, B. A.; Lesh, G. C.; Huggins, R. A. *J Electrochem Soc* **1981,** *128* (4), 725-729.

(4)　Gao, B.; Sinha, S.; Fleming, L.; Zhou, O. *Adv Mater* **2001,** *13* (11), 816-819.

(5)　(a) Timmons, A.; Dahn, J. R. *J Electrochem Soc* **2007,** *154* (5), A444-A448; (b) Li, H.; Huang, X. J.; Chen, L. Q.; Zhou, G. W.; Zhang, Z.; Yu, D. P.; Mo, Y. J.; Pei, N. *Solid State Ionics* **2000,** *135* (1-4), 181-191.

(6)　Wen, C. J.; Huggins, R. A. *J Solid State Chem* **1981,** *37* (3), 271-278.

(7)　(a) Kasavajjula, U.; Wang, C.; Appleby, A. J. *J Power Sources* **2007,** *163* (2), 1003-1039; (b) Ruffo, R.; Hong, S. S.; Chan, C. K.; Huggins, R. A.; Cui, Y. *The Journal of Physical Chemistry C* **2009,** *113* (26), 11390-11398; (c) Lee, Y. M.; Lee, J. Y.; Shim, H.-T.; Lee, J. K.; Park, J.-K. *J Electrochem Soc* **2007,** *154* (6), A515-A519.

(8)　Park, M. H.; Kim, M. G.; Joo, J.; Kim, K.; Kim, J.; Ahn, S.; Cui, Y.; Cho, J. *Nano Lett* **2009,** *9* (11), 3844-3847.

(9)　Song, T.; Xia, J. L.; Lee, J. H.; Lee, D. H.; Kwon, M. S.; Choi, J. M.; Wu, J.; Doo, S. K.; Chang, H.; Il Park, W.; Zang, D. S.; Kim, H.; Huang, Y. G.; Hwang, K. C.; Rogers, J. A.; Paik, U. *Nano Lett* **2010,** *10* (5), 1710-1716.

(10)　Xiao, J.; Xu, W.; Wang, D. Y.; Choi, D. W.; Wang, W.; Li, X. L.; Graff, G. L.; Liu, J.; Zhang, J. G. *J Electrochem Soc* **2010,** *157* (10), A1047-A1051.

(11)　(a) Cui, L. F.; Yang, Y.; Hsu, C. M.; Cui, Y. *Nano Lett* **2009,** *9* (9), 3370-3374; (b) Hu, Y. S.; Adelhelm, P.; Smarsly, B. M.; Maier, J. *Chemsuschem* **2010,** *3* (2),

231-235; (c) Xu, Y. H.; Yin, G. P.; Ma, Y. L.; Zuo, P. J.; Cheng, X. Q. *J Mater Chem* **2010,** *20* (16), 3216-3220; (d) Si, Q.; Hanai, K.; Ichikawa, T.; Hirano, A.; Imanishi, N.; Takeda, Y.; Yamamoto, O. *J Power Sources* **2010,** *195* (6), 1720-1725; (e) Wang, W.; Kumta, P. N. *Acs Nano* **2010,** *4* (4), 2233-2241.

(12)   Magasinski, A.; Dixon, P.; Hertzberg, B.; Kvit, A.; Ayala, J.; Yushin, G. *Nat Mater* **2010,** *9* (4), 353-358.

(13)   Chan, C. K.; Patel, R. N.; O'Connell, M. J.; Korgel, B. A.; Cui, Y. *Acs Nano* **2010,** *4* (3), 1443-1450.

(14)   Zhou, S.; Liu, X. H.; Wang, D. W. *Nano Lett* **2010,** *10* (3), 860-863.

(15)   Krishnan, R.; Lu, T.-M.; Koratkar, N. *Nano Lett.* **2011,** *11*, 377-384.

(16)   Limthongkul, P.; Jang, Y. I.; Dudney, N. J.; Chiang, Y. M. *Acta Mater* **2003,** *51* (4), 1103-1113.

(17)   Cui, L. F.; Ruffo, R.; Chan, C. K.; Peng, H. L.; Cui, Y. *Nano Lett* **2009,** *9* (1), 491-495.

(18)   Cui, L. F.; Hu, L. B.; Wu, H.; Choi, J. W.; Cui, Y. *J Electrochem Soc* **2011,** *158* (5), A592-A596.

(19)   Yang, X. L.; Wen, Z. Y.; Huang, S. H.; Zhu, X. J.; Zhang, X. F. *Solid State Ionics* **2006,** *177* (26-32), 2807-2810.

(20)   Yu, Y.; Gu, L.; Zhu, C. B.; Tsukimoto, S.; van Aken, P. A.; Maier, J. *Adv Mater* **2010,** *22* (20), 2247-+.

(21)   Kim, J. B.; Lee, H. Y.; Lee, K. S.; Lim, S. H.; Lee, S. M. *Electrochem Commun* **2003,** *5* (7), 544-548.

(22)   (a) Kim, J. W.; Ryu, J. H.; Lee, K. T.; Oh, S. M. *J Power Sources* **2005,** *147* (1-2), 227-233; (b) Johnson, D. C.; Mosby, J. M.; Riha, S. C.; Prieto, A. L. *J Mater Chem* **2010,** *20* (10), 1993-1998.

(23)   (a) Sethuraman, V. A.; Kowolik, K.; Srinivasan, V. *J Power Sources* **2011,** *196* (1), 393-398; (b) Chen, H.; Xiao, Y.; Wang, L.; Yang, Y. *J Power Sources* **2011,** *196* (16), 6657-6662.

(24)   (a) Park, B. K.; Jeong, S.; Kim, D.; Moon, J.; Lim, S.; Kim, J. S. *J Colloid Interf Sci* **2007,** *311* (2), 417-424; (b) Anzlovar, A.; Orel, Z. C.; Zigon, M. *J Nanosci Nanotechno* **2008,** *8* (7), 3516-3525; (c) Fievet, F.; Fievetvincent, F.; Lagier, J. P.; Dumont, B.; Figlarz, M. *J Mater Chem* **1993,** *3* (6), 627-632; (d) Carroll, K. J.; Reveles, J. U.; Shultz, M. D.; Khanna, S. N.; Carpenter, E. E. *J Phys Chem C* **2011,** *115* (6), 2656-2664; (e) Larcher, D.; Patrice, R. *J Solid State Chem* **2000,** *154* (2), 405-411.

(25)   (a) Song, H.; Rioux, R. M.; Hoefelmeyer, J. D.; Komor, R.; Niesz, K.; Grass, M.; Yang, P.; Somorjai, G. A. *J Am Chem Soc* **2006,** *128* (9), 3027-3037; (b)

Borodko, Y.; Habas, S. E.; Koebel, M.; Yang, P.; Frei, H.; Somorjai, G. A. *The Journal of Physical Chemistry B* **2006,** *110* (46), 23052-23059.

(26)   Son, S. U.; Park, I. K.; Park, J.; Hyeon, T. *Chemical Communications* **2004,** (7), 778-779.

(27)   Zhao, Y.; Zhu, J. J.; Hong, J. M.; Bian, N. S.; Chen, H. Y. *Eur J Inorg Chem* **2004,** (20), 4072-4080.

(28)   (a) Dulaurent, O.; Courtois, X.; Perrichon, V.; Bianchi, D. *The Journal of Physical Chemistry B* **2000,** *104* (25), 6001-6011; (b) Bradley, J. S.; Hill, E. W.; Chaudret, B.; Duteil, A. *Langmuir* **1995,** *11* (3), 693-695.

(29)   Beuvier, T.; Richard-Plouet, M.; Mancini-Le Granvalet, M.; Brousse, T.; Crosnier, O.; Brohan, L. *Inorg Chem* **2010,** *49* (18), 8457-8464.

(30)   Nanda, J.; Datta, M. K.; Remillard, J. T.; O'Neill, A.; Kumta, P. N. *Electrochem Commun* **2009,** *11* (1), 235-237.

(31)   Pollak, E.; Salitra, G.; Baranchugov, V.; Aurbach, D. *The Journal of Physical Chemistry C* **2007,** *111* (30), 11437-11444.

(32)   Gaisler, S. V.; Semenova, O. I.; Sharafutdinov, R. G.; Kolesov, B. A. *Phys Solid State+* **2004,** *46* (8), 1528-1532.

(33)   Hardwick, L. J.; Ruch, P. W.; Hahn, M.; Scheifele, W.; Kotz, R.; Novak, P. *J Phys Chem Solids* **2008,** *69* (5-6), 1232-1237.

(34)   (a) Baranchugov, V.; Markevich, E.; Salitra, G.; Aurbach, D.; Semrau, G.; Schmidt, M. A. *J Electrochem Soc* **2008,** *155* (3), A217-A227; (b) Hardwick, L. J.; Ruch, P. W.; Hahn, M.; Scheifele, W.; Kötz, R.; Novák, P. *J Phys Chem Solids* *69* (5-6), 1232-1237.

(35)   Oumellal, Y.; Delpuech, N.; Mazouzi, D.; Dupre, N.; Gaubicher, J.; Moreau, P.; Soudan, P.; Lestriez, B.; Guyomard, D. *J Mater Chem* **2011,** *21* (17), 6201-6208.

(36)   (a) Bridel, J. S.; Azais, T.; Morcrette, M.; Tarascon, J. M.; Larcher, D. *Chem Mater* **2010,** *22* (3), 1229-1241; (b) Dimov, N.; Kugino, S.; Yoshio, M. *Electrochim Acta* **2003,** *48* (11), 1579-1587.

(37)   (a) Harris, J. T.; Hueso, J. L.; Korgel, B. A. *Chem Mater* **2010,** *22* (23), 6378-6383; (b) Pell, L. E.; Schricker, A. D.; Mikulec, F. V.; Korgel, B. A. *Langmuir* **2004,** *20* (16), 6546-6548.

(38)   Heitsch, A. T.; Fanfair, D. D.; Tuan, H.-Y.; Korgel, B. A., *J. Am. Chem. Soc.* **2008**, *130*, 5436.

(39)   Lee, D. C.; Hanrath, T.; Korgel, B. A. *Angew. Chem. Int. Ed.* **2005**, *44*, 3573.

(40)   Holmes, J. D.; Johnston, K. P.; Doty, R. C.; Korgel, B. A. *Science* **2000**, *287*, 1471.

(41) Hanrath, T.; Korgel, B. A. *Adv. Mater.* **2003**, *15*, 437.

(42) Smith, D. A.; Holmberg, V. C.; Korgel, B. A. *ACS Nano* **2010,** *4*, 2356.

(43) Lee, J. K.; Smith, K. B.; Hayner, C. M.; Kung, H. H. *Chem. Commun.* **2010***, 46*, (12), 2025-2027.

(44) Smith, D. A.; Holmberg, V. C.; Lee, D. C.; Korgel, B. A. *J. Phys. Chem. C* **2008**, *112*, 10725.

(45) de Heer, W. A.; Bacsa, W. S.; Châtelain, A.; Gerfin, T.; Humphrey-Baker, R.; Forro, L.; Ugarte, D. *Science* **1995**, *268*, 845.

(46) Endo, M.; Muramatsu, H.; Hayashi, T.; Kim, Y. A.; Terrones, M.; Dresselhaus, M. S. *Nature* **2005**, *433*, 476.

(47) Yuan, J.; Liu, X.; Akbulut, O.; Hu, J.; Suib, S. L.; Kong, J.; Stellacci, F. *Nature Nanotech.* **2008**, *3*, 332.

(48) Holmberg, V. C.; Patel, R. N.; Korgel, B. A. *J. Mater. Res.* **2011**, *26*, 2305.

(49) Heitsch, A. T.; Akhavan, V. A.; Korgel, B. A. *Chem. Mater.* **2011,** *23*, 2697.

(50) Choi, J. W.; Hu, L.; Cui, L.; McDonough, J. R.; Cui, Y., *J. Power Sources* **2010***, 195*, 8311.

(51) Huang, R.; Fan, X.; Shen, W.; Zhu, J. *App. Phys. Lett.* **2009**, *95*, 133119.

(52) Hu, L.; Wu, H.; La Mantia, F.; Yang, Y.; Cui, Y. *ACS Nano* **2010,** *4*, 5843.

(53) Ng, S. H.; Wang, J.; Guo, Z. P.; Chen, J.; Wang, G. X.; Liu, H. K. *Electrochim. Acta* **2005**, *51*, 23.

(54) Wang, J.-Z.; Zhong, C.; Chou, S.-L.; Liu, H.-K. *Electrochem. Commun.* **2010,** *12*, 1467.

(55) Tuan, H.-Y.; Korgel, B. A. *Chem. Mater.* **2008**, *20*, 1239.

(56) Saunders, A. E.; Sigman, M. B.; Korgel, B. A. *J. Phys. Chem. B* **2004**, *108*, 193.

(57) Choi, H. S., Park, C. R. *InTech*, **2010,** ISBN 978-953-307-058-2 Available from:

http://www.intechopen.com/articles/show/title/towards-high-performance-anodes-with-fast-charge-discharge-rate-for-lib-based-electrical-vehicles

(58) Weydanz, W. J.; Wohlfahrt-Mehrens, M.; Huggins, R. A. *J. Power Sources* **1999**, *81*, 237.

(59) Obrovac, M. N.; Christensen, L., *Electrochem. Solid-State Lett.* **2004**, *7*, A93.

(60) Chan, C. K.; Peng, H.; Liu, G.; McIlwrath, K.; Zhang, X. F.; Huggins, R. A.; Cui, Y. *Nat Nano* **2008**, *3*, 31.

(61) Tuinstra, F.; Koenig, J. L. *J. Chem. Phys.* **1970**, *53*, 1126.

(62) Lespade, P.; Al-Jishi, R.; Dresselhaus, M. S. *Carbon* **1982**, *20*, 427.

(63)   Ferrari, A. C.; Robertson, J. *Phys. Rev. B* **2000**, *61*, 14095.

(64)   Ferrari, A. C. *Solid State Commun.* **2007**, *143*, 47.

(65)   Galeener, F. L.; Mikkelsen Jr, J. C. *Solid State Commun.* **1981**, *37*, 719.

(66)   Monika, W.;Wang, Y. ; Zerda, T. W*J. Phys. Condens. Matter* **2005**, *17*, 2387.

(67)   Timmons; A; Todd; A. D, W.; Mead; S, D.; Carey; Graham, H.; Sanderson; R, J.;
         Mar; R, E.; Dahn; J, R. *Electrochem. Soc.* **2007,** *154.*

Chapter 4: Amorphous Silicon Coated Germanium Core-Shell Nanowires

4.1 INTRODUCTION

As the world's population continues to grow, we have a growing need for cheap, portable methods of energy storage and delivery. Most of these portable energy needs are met by lithium ion batteries. Lithium ion batteries offer one of the highest energy densities and longest lifetimes available, but there has been little improvement since they first hit the market in 1991.[1] They are limited by the amount of Li ions that can be chemically stored in the anode and cathode materials. While gains are necessary on both the cathode and anode side, this report focuses on the anode only. On the anode side, the largest potential capacity gains can be found in lithium alloys.[2,3] Particularly, silicon (Si) and germanium (Ge) both form high capacity lithium alloys at room temperature ($Li_{15}Si_4$, 3579 mA h/g[4-6] and $Li_{15}Ge_4$, 1624 mA h/g[7]), and both are abundant with a low working potential compared to Li[4,5,7]. Both have capacities much higher than the 372 mA h/g lithiation capacity of the current standard, graphite. Their limitations arise from a massive volume expansion of over 300% that causes pulverization of crystalline Si and Ge upon repeated lithiation/delithiation cycles, causing loss of electrical contact, irreversible capacity loss and eventually battery failure.[2,8] To overcome the pulverization problem, numerous approaches have been explored.

Nanostructuring has been shown to reduce these pulverization effects by accommodating higher degrees of strain. Nanotubes, nanorods, nanowires, nanocrystals, and thin films have all been explored with promising results. Si nanotubes grown using alumina templates have displayed capacities as high as 3247 mA h/g, but only 89% Coulombic efficiency.[9] Si and Ge nanocrystals display extremely high capacity retention over many cycles, but due to the need for an extensive conductive carbon matrix to

maintain electrical contact their effective gravimetric capacity is limited.[10-12] Likewise, core-shell nanoarchitectures of Si over carbon show great cyclability but an unrealized maximum effective capacity.[8,13-15] Thin films of both Si and Ge, grown by chemical vapor deposition (CVD), have capacities near their respective theoretical maxima with negligible capacity fade over hundreds of lithiation/delithiation cycles.[16-18] However, they are extremely expensive and could not be practically scaled for commercialization. Similarly, CVD and vapor-liquid-solid (VLS) grown nanowires have shown promise;[19,20] Cui, et al even achieved a capacity of 2725 mA h/g with good stability, retaining 1400 mA h/g after 700 cycles.[18] Again, these have problems with scalability due to their CVD roots. By utilizing solution and supercritical fluid based processes for Si and Ge nanostructure growth, such as solution-liquid-solid (SLS) and supercritical fluid-liquid-solid (SFLS) growth, large quantities of nanowires, nanorods, or nanoparticles can be produced at relatively low cost.[21,22]

Though Li-Ge and Li-Si alloys have both been explored since the 60s and 70s, only Si has garnered much attention as a LIB anode until recently. Si and Ge both offer unique properties as anode materials. Si has a much higher theoretical gravimetric capacity – 3579 mA h/g vs 1624 mA h/g – but nearly identical volumetric capacities. Though Ge is the more expensive of the two materials, it has many attractive attributes. Si expands anisotropically upon lithiation, while Ge expands isotropically.[9] This leads to reduced strain and pulverization. Ge has a higher intrinsic conductivity than Si, and a Li diffusion coefficient 400 times that of Si.[23] This allows Ge to perform better at higher current densities making it attractive for high power situations.[24] By creating Si-Ge heterostructures, potentially the best of both materials can be realized. The Ge can provide a more robust, more conductive, and faster lithiating matrix for Si, while the Si can boost the overall capacity of the Si-Ge nanostructure. This report presents Ge

nanowires coated with a-Si as high capacity anodes in lithium ion batteries. By evenly coating the surface of the nanowires with a-Si, the conductive pathways for Si are increased along with the surface to volume ratio. This encourages easier lithiation from decreased diffusion pathlengths and overall resistivity to Li-ions. Theoretically, the total gravimetric capacity of the anode could then be increased by increasing the thickness of the a-Si layer. These nanostructures provide an avenue for exciting research and potential far-reaching improvements to Li-ion batteries.

4.2 EXPERIMENTAL DETAILS

4.2.1 Reagents

Dodecanethiol ($C_{12}H_{25}SH$, ≥98%), gold tetrachloroaurate trihydrate ($HAuCl_4 \cdot 3H_2O$, 99.9+%), sodium borohydride ($NaBH_4$, 98+%), tetraoctylammonium bromide ($C_{32}H_{68}BrN$, TOAB, 98%), toluene (C_7H_8, ACS grade), ethanol (C_2H_5OH, ACS grade), methanol (CH_3OH, ACS grade), and chloroform ($CHCl_3$, ACS grade) were purchased from Sigma-Aldrich. Triply distilled deionized water (DI-H_2O) filtered with an 18.2 MΩ-cm resistance Barnstead E-pure unit was used for all aqueous preparations. Monophenylsilane (MPS, >95%) and diphenylgermane (DPG, >95%) was obtained from Gelest. Trisilane (Si_3H_8, >95%) was obtained from Voltaix and $LiPF_6$ (1.0M in a 1:1 mixture of ethylcarbonate [EC>99.95%]: diethyl carbonate [DEC>99.98%]) was purchased from Novolyte. For battery assembly, Celgard 2400 membranes (25μm) were used as separators, purchased from Celgard, and Li metal (99.9%) from Alfa Aesar. All chemicals were used as received.

4.2.2 Synthesis of Ge@a-Si Nanowires

4.2.2.1 SFLS Growth of Ge Nanowires

Ge NWs were produced by the standard SFLS method as previously described. Briefly, a solution of dodecanethiol capped Au nanocrystals and DPG in toluene is loaded into a titanium piston under nitrogen. A nitrogen filled titanium reactor is placed in the heating block and pressurized with supercritical anhydrous toluene to 1000 psi at 380 $^{\circ}$C. Flow is then switched to the piston and the reactant solution is flowed in at 0.5 mL/min for 40 min. The reactor is then sealed and allowed to cool to room temperature. The product is removed from the reactor and 10 mL of chloroform is added. The dispersion is centrifuged at 8000 rpm for 5 min in a glass centrifuge tube and the precipitate is collected. The precipitate is redispersed in chloroform, and the centrifugation process is repeated two more times.

4.2.2.2 Coating Ge Nanowires with a-Si through decomposition of trisilane

For in situ coating of a-Si on Ge NWs, the entire reaction is performed within a nitrogen filled glovebox. The standard Ge NW SFLS reaction is performed, but the Ge NWs are never removed from the first reactor. After cooling the Ge NWs, 10 mL of pure anhydrous toluene is flowed through the reactor at 0.5 mL/min to remove any remaining reactants. The reactor is heated to 200 $^{\circ}$C and then sealed. A 5 mL injection loop loaded with a solution of trisilane in anhydrous toluene is attached to the 6-way valve. The trisilane solution is flowed into the reactor at 0.5 mL min for 5 min while the exit valve remains sealed. The reactor is then completely sealed and allowed to rest for 15 min. The temperature is increased to 430 $^{\circ}$C over 30 min and remained at 430 $^{\circ}$C for 15 min. The reactor was then removed from the block and cooled to room temperature. The product

was extracted with chloroform and purified by centrifugation as described for pure Ge NWs.

4.2.2.3 Coating Ge Nanowires with a-Si through decomposition of monophenylsilane

Monophenylsilane was also used as an a-Si source for coating Ge NWs. The standard Ge NW SFLS reaction is performed, but the Ge NWs are never removed from the first reactor. After cooling the Ge NWs, 10 mL of pure anhydrous toluene is flowed through the reactor at 0.5 mL/min to remove any remaining reactants. Two separate methods were then utilized: batch and flow-through.

For the batch reactions, the reactor is heated to 200 ^{o}C and then sealed. A 5 mL injection loop loaded with a solution of monophenylsilane in anhydrous toluene is attached to the 6-way valve. The monophenylsilane solution is flowed into the reactor at 0.5 mL min for 5 min while the exit valve remains sealed. The reactor is then completely sealed and allowed to rest for 15 min. The temperature is increased to 490 ^{o}C over 30 min and remained at 490 ^{o}C for 15 min. The reactor is then removed from the block and cooled to room temperature. The product is extracted with chloroform and purified by centrifugation as described for pure Ge NWs.

For the flow-through reactions, a more dilute solution of monophenylsilane in anhydrous toluene was loaded in a 30 mL titanium piston. The reaction then proceeds just as the initial Ge NW reaction. The reactor, still containing the Ge NWs, is heated to 490 ^{o}C and pressurized to 1500 psi with pure toluene. The piston containing MPS is hooked to the reactor setup. The MPS solution is flowed through the reactor at 0.5 mL/min for 40 min at 490 ^{o}C. The reactor is then sealed and allowed to cool to room temperature. The product is extracted with chloroform and purified by centrifugation as described for pure Ge NWs.

4.2.3 Construction of LIB Anodes

The Ge and Ge@a-Si nanowire slurries were prepared by dispersing the nanowires (70 mg) in 2 mL toluene and bath sonicating for 1 hour. Meanwhile, 20 mg PVdF and 10 mg carbon black were dissolved in 1 mL NMP and bath sonicated for 1 hour. The nanowire and PVdF / carbon black suspensions (70:20:10 w/w solid content of Ge : PVdF : carbon black) were mixed and wand sonicated for an additional 30 minutes. The solution was then reduced by rotovap to yield a thick slurry. The slurry was cast onto Cu foil–which acts as the current collector for the battery–using a 200 μm film applicator and vacuum dried overnight at 100 $^{\circ}$C. Batteries were assembled in an argon-filled glovebox. Nanowire anodes were punched from the Cu foil (1 cm diameter) supported slurry film. The electrolyte was a 1.0 M solution of LiPF$_6$ in a solution of 1:1 w/w EC:DEC with 5% FEC additive. A few drops of electrolyte were deposited over lithium foil and again atop a Celgard 2400 separator membrane (25 μm thick, Celgard) before adding the Ge or Ge@a-Si anode and crimping the completed battery.

For the MPS coated Ge NWs, batteries were tested on free standing films. Ge nanowire fabric was prepared by sonicating nanowire dispersions (5-10 mg/mL Ge nanowires in chloroform) for 1 hour. The dispersions were drop cast into a Teflon trough and left overnight to dry. After drying, the fabric is peeled from the trough using tweezers and a thin razor blade wedged between the fabric and trough bed when necessary and cut into 1cm x 1cm squares that were loaded into quartz boats and heated under a moderate flow of forming gas in a tube furnace.

Batteries were prepared within an argon-filled glovebox using a Cu foil current collector. The Si nanowire fabric was placed on the Cu current collector to serve as the anode material. The electrolyte was a 1.0 M solution of LiPF$_6$ in a 1:1 mixture of ethylcarbonate : diethyl carbonate (EC>99.95%, DEC>99.98%, Novolyte) with 5% FEC

additive. A few drops of electrolyte were deposited over the nanowire fabric. A Celgard 2400 separatror membrane (25μm thick, Celgard) was then added followed by Li metal (99.9%, Alfa Aesar) foil as the counter electrode.   Galvanostatic measurements were made using an Arbin BT-2143 test unit that was cycled between 3V and 10mV vs Li/Li$^+$ at a rate of C/20 (C = 3579 mA h/g).

4.2.4 Materials Characterization

Scanning electron microscopy (SEM) images were acquired using a Zeiss Supra 40 SEM with an in-lens arrangement, a working voltage of 5 keV and a working distance of 5 mm. SEM samples were imaged silicon wafers (S.E.H). Transmission electron microscopy (TEM) images were digitally acquired using a either a FEI Tecnai Spirit BioTwin TEM operated at 80 kV or a field emission JEOL 2010F TEM operated at 200 kV. TEM samples were prepared by drop-casting from chloroform dispersions onto 200 mesh lacey-carbon copper TEM grids (Electron Microscopy Sciences).

X-ray diffraction (XRD) was carried out using a Rigaku R-Axis Spider Diffractometer with Image plate detector with Cu-k$_\alpha$ (λ = 1.5418 Å) radiation operated at 40 kV and 40 mA. Measurements using were taken on samples on a 0.5 mm nylon loop. Samples were scanned for 10 min while rotating at 1° per second under ambient conditions. The radial data were integrated from 20$^\text{o}$ to 80$^\text{o}$ 2θ and plotted. Background scattering from the nylon loop was subtracted from the sample measurement.

Raman spectroscopy was performed using a Renishaw inVia microscope equipped with a 514.5 nm Argon laser in backscattering configuration. The Stokes Raman signal at 521 cm^{-1} for single crystalline bulk Si oriented with the [110] direction normal to the laser was used to calibrate the instrument. The beam was focused using an optical microscope with a 50x objective lens. Spectra were taken on freestanding sheets

of nanowire fabric lying on glass slides by single scans from 100-2000 cm^{-1} at 5% (0.2 mW) laser power.

4.3 RESULTS AND DISCUSSION

4.3.1 Characterization of a-Si coated Ge Nanowires

4.3.1.1 Ge@a-Si Nanowires Grown with Trisilane

TEM images of typical reaction results can be seen in Figure 4.1. Ge NWs were coated with trisilane in (A) 1:1, (B) 4:1, and (C) 10:1 Si:Ge loading levels. The a-Si coating is clearly thicker with increased Si loading.
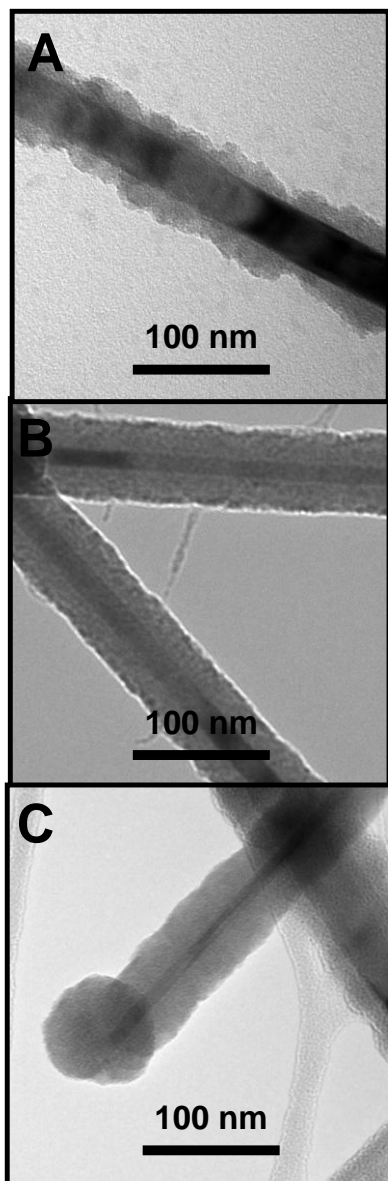
Figure 4.1: TEM images of Ge@a-Si NWs synthesized with Si:Ge loading levels of: (A) 1:1 Si:Ge, (B) 4:1 Si:Ge, and (C) 10:1 Si:Ge.

XRD spectra can be seen in Figure 4.2. XRD clearly shows the presence of crystalline Ge, though due to the large intensity differences the amorphous Si is not observed. Significant differences in the high Si loading versus low Si loading were not observed. Extremely small shoulders at 28° 2θ are seen in both spectra indicating a

96

relatively small amount of crystalline Si is present in both samples. The shoulder is slightly larger in the high Si loaded sample as expected.
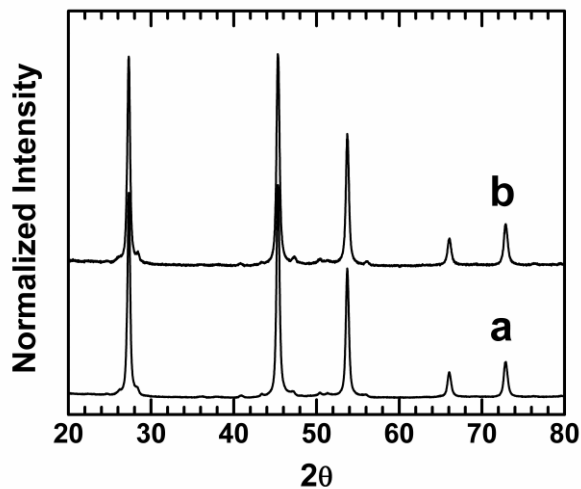
Figure 4.2: XRD spectra of (a) 1:1 Si:Ge nanowires and (b) 10:1 Si:Ge nanowires.
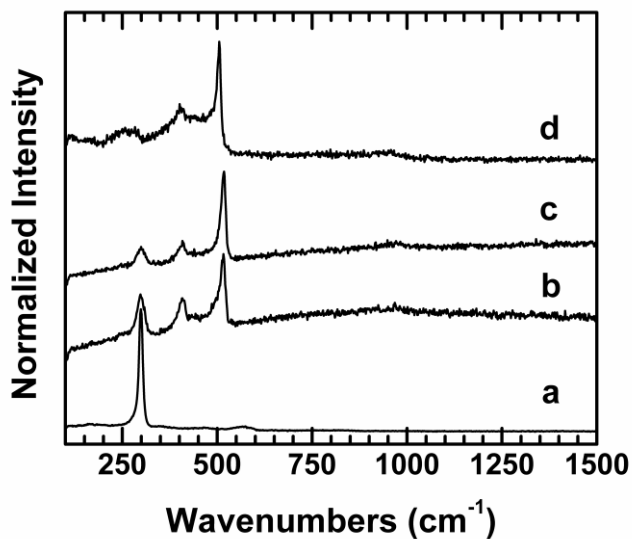
Figure 4.3: Raman spectra of Ge and Ge@a-Si nanowires acquired using a 514.5 nm Argon laser at 0.1 mW power of; (a) pure Ge NWs, (b) 1:1 Si:Ge Ge@a-Si NWs, (c) 4:1 Si:Ge Ge@a-Si NWs, and (d) 10:1 Si:Ge Ge@a-Si NWs.

However, the Raman spectra are extremely interesting as seen in Figure 5.3. Again, crystalline Ge is present as seen at 298 cm^{-1}, but a broad a-Si is not observed at 480 cm^{-1} at low a-Si loading levels. (b) and (c) show a large peak for c-Si (519 cm^{-1}) present with only a small amorphous shoulder. At highest a-Si loading levels, (d), the Si peak is shifted toward 495 cm^{-1}, indicating increased amorphous character of the Si. Simulaneously, the Ge peak spreads. The thick layer of a-Si causes these changes in the spectra. Previously I have observed a laser annealing phenomenon for a-Si particles under high laser power (3.0 mW), but these samples were probed with only 0.1 mW laser power. Likely, the power required to anneal the sample was decreased due to the strain at the Si-Ge interface, giving rise to the unexpectedly large 519 cm^{-1} peak even under low power. The thick a-Si sample is not affected as much because there is less interface to volume and the strain is weakened. The ratio of the Si peak to the Ge gets larger with Si loading, as expected. Finally, a peak is present at 403 cm^{-1} attributed to Si-Ge local phonon modes.[25] The high ratio of this peak to the pure Ge and Si peaks indicates that there is a significant amount of contact between Ge and Si, yet no crystalline SiGe was observed in XRD. This strongly indicates a core-shell structure of a-Si on Ge.

To further explore the Si-Ge system, Raman spectra of dense $Si_{(1-x)}Ge_x$ films deposited on glass at normal incidence were measured. The spectra from the as deposited films are shown in Figure 4.4a.
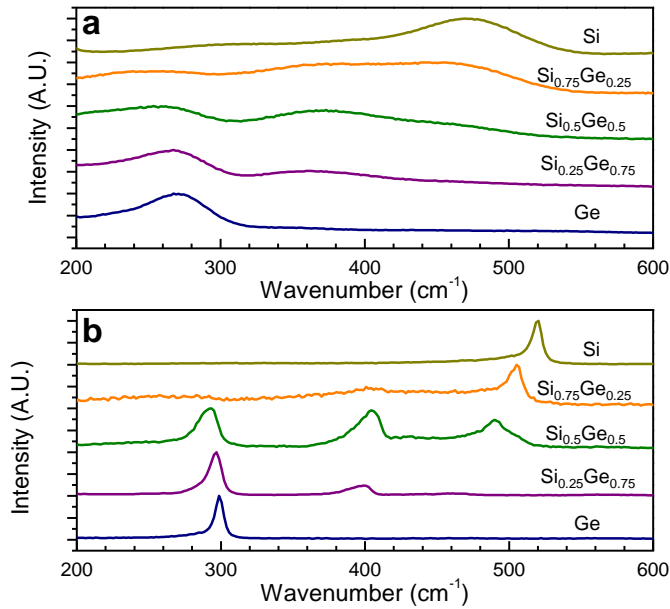
Figure 4.4: Raman spectra of $Si_{(1-x)}Ge_x$ films a) as deposited and b) Raman-laser annealed films

The features are diffuse, indicating that the material is amorphous; broad peaks characteristic of Si-Si, Si-Ge and Ge-Ge vibrations are present for the intermediate compositions. The features sharpen considerably after annealing the films with the Raman laser. Only 10% laser power was required for annealing. Spectra of annealed films are shown in Figure 4.4b. Expectedly, the pure silicon and pure germanium films show only vibrations of the homogeneous bonds, whereas the Si-Ge vibration is observed in the intermediate compositions. The peak intensities of the Si-Si, Si-Ge, and Ge-Ge vibrations are similar in the $Si_{0.5}Ge_{0.5}$ film, consistent with random bonding of silicon and germanium rather than preferred bonding of Si with Si or of Ge with Ge. The $Si_{0.75}Ge_{0.25}$ and $Si_{0.25}Ge_{0.75}$ films each had a strong peak for the majority component homogeneous bond and a minor peak for the heterogeneous bond.

4.3.1.2 Ge NWs Grown with MPS Additives

The alternative approach to coating Ge NWs with a-Si shells used an MPS precursor as the Si source. Figure 4.5 shows the TEM images of Ge NWs treated with MPS. In (A), the MPS is added in situ after the Ge NW reaction is completed and cooled at completion. In (B), the same process is completed but it is incubated for 4 hrs rather than cooled. Finally, (C) has MPS added along with DPG for the initial reaction. TEM reveals no noticeable difference amongst the samples. (D) is a typical HRTEM image showing that there is a small amorphous shell surrounding the Ge NWs.
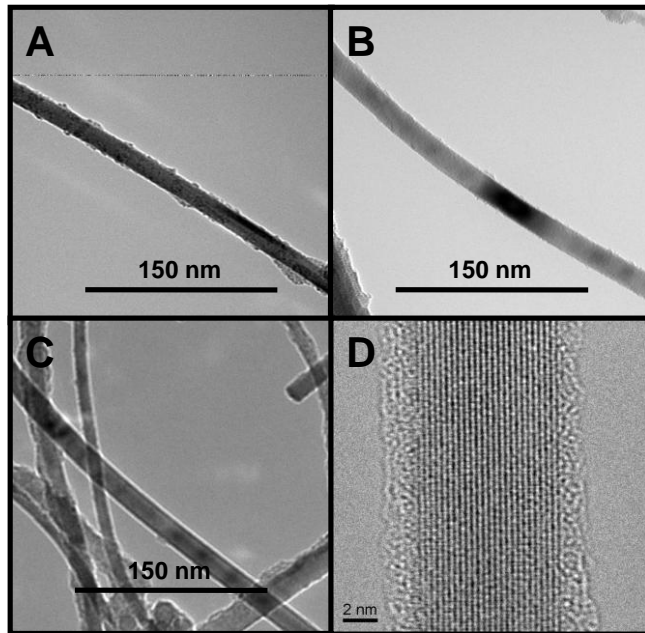
Figure 4.6: TEM images of Ge NWs treated with MPS. (A) MPS added after the reaction, (B) MPS added after the reaction and then incubated in the reactor for 4 hrs, and (C) MPS added to the initial DPG solution. (D) Typical high resolution TEM image of Ge NWs coated with MPS.

Figure 4.7 shows Raman spectra of the as-made MPS treated Ge nanowires. All of the samples contain crystalline Ge only, with peaks at ~300 cm^{-1}. Interestingly, all of the samples that were treated with MPS also display carbon D and G bands that arise at

1380 and 1560 cm^{-1}, respectively.[26,27] In fact, the incubated sample (d) has carbonaceous peaks that completely dwarf the Ge peak. This is similar to the annealed MPS Si nanowire paper discussed in previous chapters.[28]
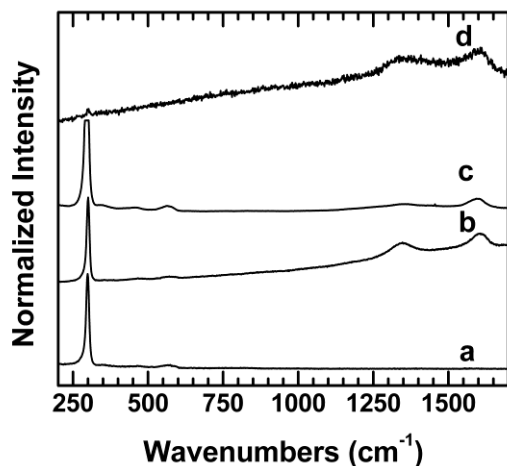
Figure 4.7: Raman spectra of the four as made nanowire paper samples acquired with a 514.5 nm Argon laser at 0.1 mW power. (a) pure Ge NW, (b) Ge NW with MPS added after the reaction, (c) Ge NW synthesized with MPS and DPG in initial solution, and (d) Ge NW with MPS added after the reaction and then incubated in the reactor for 4 hrs.

4.3.2 Electrochemical Characterization of Nanowires

The trisilane grown a-Si coated Ge nanowires show improved lithium ion battery performance over bare Ge wires, displaying improved capacities and maintained cyclability as seen in Figure 4.8. The nanowires were cast in a 70:20:10 (by weight) NW : PVdF : carbon black slurry and formed into anodes. As a-Si is added to the surface of the Ge NWs gravimetric capacity after 20 cycles increases from (a) ~500 mA h/g for bare Ge NWs, to (b) 650 mA h/g with 1:1 Si:Ge. Further increases are seen, up to (c) 1050 mA h/g with 4:1 Si:Ge and all the way to (d) 1800 mA h/g at 10:1 Si:Ge loading. The higly loaded Ge@a-Si NWs are very encouraging, with a reversible capacity above the theoretical maximum of Ge.

101
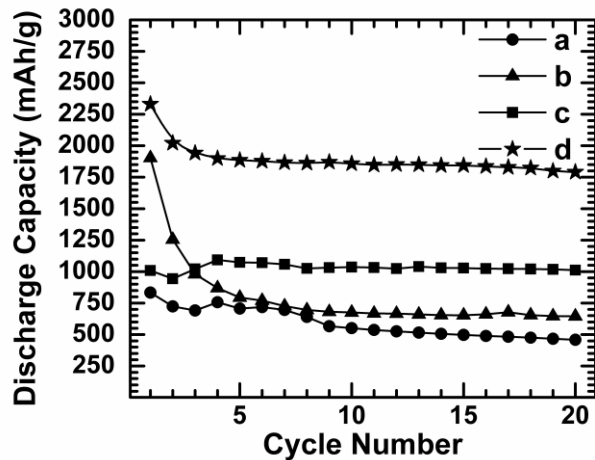
Figure 4.8: Plot of gravimetric capacity of NW samples cycled at a C/20 rate for 20 cycles. (a) pure Ge NW, (b) 1:1 Si loaded Ge NWs, (c) 4:1 Si loaded Ge NWs, and (d) 10:1 Si loaded Ge NWs.

Figure 4.9 shows the discharge capacities of the Ge NW paper anodes. These were plain NW anodes, with no addition of binder or conductive carbon. Both samples (b) and (c) that were treated with MPS but not incubated showed a moderate decrease in capacity, but whether the MPS was added after the reaction (a) or during (b) had no effect on cycling characteristics. The sample incubated for 4 hrs in the reactor displayed a 75% increase in capacity to 750 mA h/g. This effect is attributed to a slight uptick in surface conductivity between the wires due to formation of conductive carbon on the surface of the wires. The samples were then annealed under reducing atmosphere to enhance conductivity, but the Ge NWs were destroyed in the process. The unpassivated Ge NWs are easily oxidized and destroyed when heated. Despite the reducing atmosphere, the adsorbed water and oxygen was enough to destroy the paper anodes.
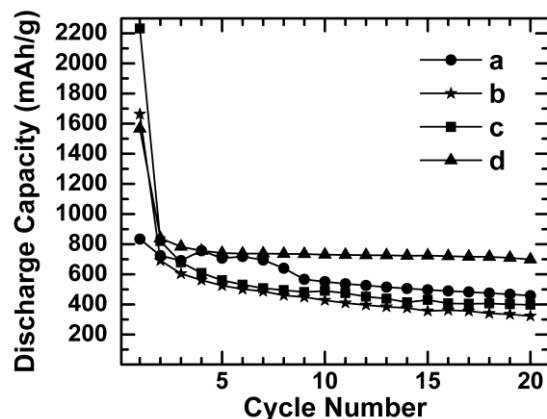
Figure 4.9: Plot of gravimetric capacity of NW samples cycled at a C/20 rate for 20 cycles. (a) pure Ge NW, (b) Ge NW with MPS added after the reaction, (c) Ge NW synthesized with MPS and DPG in initial solution, and (d) Ge NW with MPS added after the reaction and then incubated in the reactor for 4 hrs.

4.4 CONCLUSIONS

Though Si offers higher theoretical capacities than Ge, in practice Si suffers from poor conductivity and pulverization of the anode material. Ge offers higher conductivities and isotropic expansion. a-Si also exhibits isotropic expansion and less pulverization that its crystalline counterpart. The best of both systems is realized through the use of heterostructure. By coating Ge nanowires with a-Si, the a-Si has support of a more conductive matrix and decreased lithium ion diffusion lengths. a-Si coated Ge nanowires were successfully synthesized through a post-reaction decomposition of trisilane on the surface of the wires. The thickness of the a-Si shell was controlled by varying the ratio of Si to Ge in the reaction. Shells were grown up to 40 nm thick with even and complete coverage of the nanowire surfaces. The a-Si shells enhanced the lithiation capacity of the wires while maintaining high reversibility. With a 40 nm shell, a lithiation capacity of

103

1800 mA h/g after 20 cycles was maintained – higher than the theoretical capacity of Ge alone.

Monophenylsilane was also used to coat the Ge nanowires with significantly different results. Despite various MPS treatments, little variation in coating was noticed. HRTEM did identify a thin amorphous shell on the nanowire surface, and Raman identified a small carbonaceous coating. After incubation, capacity of the Ge NWs increased due to reduction of the coating to conductive carbon. The lithiation capacity of the nanowires was increased 75% after MPS incubation. Attempts to anneal the NW paper were unsuccessful.

4.5 REFERENCES

(1)   Armand, M.; Tarascon, J. M. *Nature* **2008**, *451*, 652.

(2)   Hatchard, T. D.; Dahn, J. R. *Journal of the Electrochemical Society* **2004**, *151*, A838.

(3)   Li, J.; Dahn, J. R. *Journal of the Electrochemical Society* **2007**, *154*, A156.

(4)   Li, H.; Huang, X. J.; Chen, L. Q.; Zhou, G. W.; Zhang, Z.; Yu, D. P.; Mo, Y. J.; Pei, N. *Solid State Ion.* **2000**, *135*, 181.

(5)   Yoon, S.; Park, C. M.; Sohn, H. J. *Electrochemical and Solid State Letters* **2008**, *11*, A42.

(6)   Park, M.-H.; Kim, M. G.; Joo, J.; Kim, K.; Kim, J.; Ahn, S.; Cui, Y.; Cho, J. *Nano Letters* **2009**, *9*, 3844.

(7)   Lee, J. K.; Smith, K. B.; Hayner, C. M.; Kung, H. H. *Chem. Commun.* **2010**, *46*, 2025.

(8)   Lee, J.-K.; Kung, M. C.; Trahey, L.; Missaghi, M. N.; Kung, H. H. *Chem. Mat.* **2009**, *21*, 6.

(9)   DiLeo, R. A.; Frisco, S.; Ganter, M. J.; Rogers, R. E.; Raffaelle, R. P.; Landi, B. J. *Journal of Physical Chemistry C* **2011**, *115*, 22609.

(10)   Cui, L.-F.; Yang, Y.; Hsu, C.-M.; Cui, Y. *Nano Letters* **2009**, *9*, 3370.

(11)   Hu, Y.-S.; Adelhelm, P.; Smarsly, B. M.; Maier, J. *Chemsuschem* **2010**, *3*, 231.

(12)   Wang, W.; Datta, M. K.; Kumta, P. N. *Journal of Materials Chemistry* **2007**, *17*, 3229.

(13)   Wang, W.; Kumta, P. N. *ACS Nano* **2010**, *4*, 2233.

(14)   Baggetto, L.; Hensen, E. J. M.; Notten, P. H. L. *Electrochim. Acta* **2010**, *55*, 7074.

(15)   Baggetto, L.; Notten, P. H. L. *Journal of the Electrochemical Society* **2009**, *156*, A169.

(16)   Graetz, J.; Ahn, C. C.; Yazami, R.; Fultz, B. *Electrochemical and Solid State Letters* **2003**, *6*, A194.

(17)   Laforge, B.; Levan-Jodin, L.; Salot, R.; Billard, A. *Journal of the Electrochemical Society* **2008**, *155*, A181.

(18)   Maranchi, J. P.; Kumta, P. N.; Hepp, A. F. In *Developments in Solid Oxide Fuel Cells and Lithium Ion Batteries*; Manithiram, A., Kumta, P. N., Sundaram, S. K., Chan, S. W., Eds. 2005; Vol. 161, p 121.

(19)   Rong, J. P.; Masarapu, C.; Ni, J.; Zhang, Z. J.; Wei, B. Q. *ACS Nano* **2010**, *4*, 4683.

(20)   Yao, Y.; McDowell, M. T.; Ryu, I.; Wu, H.; Liu, N. A.; Hu, L. B.; Nix, W. D.; Cui, Y. *Nano Letters* **2011**, *11*, 2949.

(21)   Chan, C. K.; Patel, R. N.; O'Connell, M. J.; Korgel, B. A.; Cui, Y. *ACS Nano* **2010**, *4*, 1443.

(22)   Chan, C. K.; Ruffo, R.; Hong, S. S.; Huggins, R. A.; Cui, Y. *J. Power Sources* **2009**, *189*, 34.

(23)   Hu, L. B.; Wu, H.; La Mantia, F.; Yang, Y. A.; Cui, Y. *ACS Nano* **2010**, *4*, 5843.

(24)   Huang, R.; Zhu, J. *Materials Chemistry and Physics* **2010**, *121*, 519.

(25)   Teh, L. K.; Choi, W. K.; Bera, L. K.; Chim, W. K. *Solid-State Electronics* **2001**, *45*, 1963.

(26)   Ferrari, A. C. *Solid State Communications* **2007**, *143*, 47.

(27)   Ferrari, A. C.; Robertson, J. *Physical Review B* **2000**, *61*, 14095.

(28)   Chockla, A. M.; Harris, J. T.; Akhavan, V. A.; Bogart, T. D.; Holmberg, V. C.; Steinhagen, C.; Mullins, C. B.; Stevenson, K. J.; Korgel, B. A. *J. Am. Chem. Soc.* **2011**, *133*, 20914.

Chapter 5: Synthesis of Bi Nanoparticles and SLS Growth Applications[§]

5.1 INTRODUCTION

Nanoparticles are of great interest due to their unique size and shape dependent optical, magnetic, and catalytic properties.[1-4] They have been shown to display significantly different properties than their bulk counterparts. Many metallic nanoparticles are also used as seeds for the SLS[5-7] and SFLS[8,9] growth of nanowires previously discussed. Of particular interest are Au and Bi nanoparticles. Au nanoparticles are well understood and extensively studied elsewhere.[10,11] Bi, however, is very interesting. Bulk Bi is a semimetal[12] with unique properties including large Fermi wavelengths, high magnetoresistance, and strong diamagnetism.[13-16] Its semimetal structure means that it has a small overlap between the valence and conduction bands, a highly anisotropic Fermi surface, long electron mean free path, low carrier density (10^5 times smaller than conventional metals at 4.2 K), and a small electron effective mass. These properties make the optical, photonic, and electronic properties strongly dependent on particle size and shape due to quantum confinement. Quantum confinement induces a semimetal to semiconductor phase transition that has been observed with features as large as 50 nm in thin films, nanotubes, nanoarrays, nanopipes, and nanoparticles.[17-20]

Xia *et al.* reported the synthesis of monodisperse Bi dots in the diameter range of 100-600 nm, which are not generally useful for SLS growth.[21] Foos *et al.* and Fanfair *et al.* reported the synthesis of Au-Bi and Bi nanoparticles as seeds for III-V semiconductor nanowires, but they had high polydispersity and were not easily isolated.[22,23] In 2008, Buhro and coworkers developed a method utilizing a polymeric capping ligand with high control over size and shape of Bi nanoparticles at high monodispersity.[24] Unfortunately,

---

[§] Portions of this chapter appear in *Chemistry of Materials*, **2010**, *23*, 1964-1970 and *ACS Applied Material Interfaces*, **2011**, *3*, 1781-1785.

shortly after publication the polymer they reported was discontinued, rendering the synthesis unusable. In this report, a suitable alternative to the discontinued polymer was discovered and the synthesis was reworked to provide high quality Bi nanocrystals for use in SLS growth of semiconductor nanorods and nanowires. By adjusting reaction parameters, moderate control over Bi size was obtained. SLS growth shows a strong dependence between initial seed size and wire diameter,[25] so varying initial Bi seed size gave control over rod/wire diameter. Specifically, Bi nanocrystals were used to grow Ge nanorods[26] and copper indium selenide ($CuInSe_2$) nanowires.[27]

5.2 EXPERIMENTAL DETAILS

5.2.1 Reagents

Sodium bis(trimethylsilyl)amide ($NaN[SiMe_3]_2$, Sigma Aldrich, 1.0 M in tetrahydrofuran), bismuth(III) chloride ($BiCl_3$, Sigma Aldrich, ɡ 98%), diphenyl ether (DPE, Sigma Aldrich, 99%), trioctylphosphine oxide (TOPO, Sigma Aldrich, 99%), anhydrous tetrahydrofuran (THF, Sigma Aldrich, 99.9%), anhydrous toluene (Sigma Aldrich, 99.8%), anhydrous hexane (Sigma Aldrich, 95%), diphenylgermane (DPG, Gelest, >95%) copper(I) acetate (Sigma Aldrich 97%), indium(III) acetate (Sigma Aldrich, 99.99%), indium(III) chloride ($InCl_3$, Sigma Aldrich, 99.999%), elemental selenium (Se, Sigma Aldrich, 99.99%), trioctylphosphine (TOP, Sigma Aldrich, 90%), oleic acid (OA, Sigma Aldrich 99%), squalane (99%), and 1-hexadecylamine (HDA, Sigma Aldrich, 90%) were purchased and used without further purification. Poly(vinylpyrrolidinone)-hexadecene (PVP/HDE) copolymer (Ganex V-216,MW= 7300 g/mol, product ID 72289D) was obtained from ISP Technologies, Inc. and used without further purification.

5.2.2 Synthesis of Bi[N(SiMe$_3$)$_2$]$_3$ Precursor

Bi[N(SiMe$_3$)$_2$]$_3$ was prepared according to literature methods.[28] In a typical procedure, 10 mL of 1.0 M NaN(SiMe$_3$)$_2$ (10 mmol of Na) in THF is added to a three-neck roundbottom flask in a nitrogen-filled glovebox. The flask is sealed, removed from the glovebox and connected to a Schlenk line. THF is evaporated under a vacuum to leave a yellow powder. The flask is blanketed with nitrogen and 20 mL anhydrous toluene is added. The solution is chilled to 0 °C by an ice bath. Separately, in a glovebox, 1.06 g BiCl$_3$ (3.35 mmol of Bi) is dissolved in 3 mL THF. 15 mL of toluene is then added to this solution and the entire mixture is transferred by syringe to the Schlenk flask containing the NaN(SiMe$_3$)$_2$/toluene mixture. The ice bath is removed and the reaction mixture is stirred for 1 h at room temperature. The solvent is then evaporated under vacuum and blanketed with nitrogen. 10 mL of anhydrous hexane is added to dissolve the product. The flask is sealed and brought into a nitrogen filled glovebox. The solution is transferred to a vial that is wrapped with paraffin film and electrical tape to avoid oxygen exposure. The vial is placed in a centrifuge tube, removed from the glovebox, and centrifuged. After centrifugation, the tube is returned to the glovebox and the vial is removed. The supernatant is collected and filtered using a Millipore 0.22 μm hydrophobic Durapore membrane syringe filter (Fisher Scientific). The filtrate is an optically clear, yellow solution, which is transferred to a three-neck flask, removed from the glovebox and placed on the Schlenk line. The solvent is evaporated under vacuum leaving the Bi[N(SiMe$_3$)$_2$]$_3$ product, which is dissolved in anhydrous THF to a concentration of 0.25 M. The product was used without further purification and was stored in a glovebox.

5.2.4 Synthesis of Bi Nanocrystals

Five grams of Ganex V216 and 15 g of diphenyl ether were combined in a 100 mL three neck flask. The flask was attached to a Schlenk line, placed under vacuum, heated to 70 $^{\circ}$C, and allowed to degas for 1.5 h while stirring. In parallel, 0.5 mL of Bi[N(SiMe$_3$)$_2$]$_3$/THF was mixed with 2.0 mL of 1 M NaN(SiMe$_3$)$_2$ in THF and placed into a syringe. After the Ganex V216 and diphenyl ether solution was degassed, the flask was refilled with N$_2$ and the temperature was increased to 180 $^{\circ}$C. At 180 $^{\circ}$C, the Bi precursor solution was quickly injected into the hot solution and reacted for 30 min. After 30 min, the mixture was cooled to 60 $^{\circ}$C and 15 mL of room-temperature toluene was added. Bi nanocrystals were isolated by centrifuging the reaction product for 3 min at 5000 rpm. The supernatant was collected, and the precipitate was discarded. Thirty milliliters of MeOH was added to the supernatant and centrifuged for 5 min at 10000 rpm. The supernatant was discarded. The precipitate was dispersed in 10 mL of toluene. This process was repeated several times, and the final precipitate was dispersed and stored in toluene at a concentration of 5 mg/mL.

5.2.4 Synthesis of Ge Nanorods

Ge nanorods were synthesized by first generating a reagent solution of Bi nanocrystals, followed by the addition of the Ge reactant solution. This process of using a crude reaction mixture of Bi nanocrystals—as opposed to purified Bi nanocrystals as a reagent—was found to provide the most reliable and reproducible results. The reagent solution of Bi nanocrystals was first prepared as just described, without the final isolation and purification steps.

After stirring the as synthesized Bi nanocrystal reactant mixture for 30 min at 180°C, 2 g of TOPO dissolved in 5 mL of toluene and 4 mL of squalane were added by syringe. The temperature was lowered to 150°C, and placed under a vacuum for 60 min

to evaporate most of the more volatile DPE and raise the boiling temperature of the reaction mixture. The flask was then blanketed in nitrogen and heated to 350°C.

Under vigorous stirring, a Ge reactant solution of 18 μL of DPG (95 μmol, which corresponds to a Ge:Bi molar ratio of 20:1 in the reaction mixture) dissolved in 500 μL of squalane was rapidly injected into the hot Bi nanocrystal mixture. The heating mantle was removed 5 min later to allow the reaction mixture to cool to room temperature.

Once the temperature fell to 100°C, 10 mL of toluene was injected to prevent the solidification of TOPO. After cooling to room temperature, 10 mL of ethanol was added and the mixture was centrifuged at 10,000 rpm for 5 min to precipitate the nanorods. The supernatant was discarded. The precipitate was resuspended in 5 mL of chloroform and 5 mL of ethanol, followed by another centrifugation. The supernatant was again discarded. The precipitate was redispersed in chloroform and stored in air. A typical reaction produces 10−15 mg of Ge nanorods.

5.2.5 Synthesis of CuInSe$_2$ Nanowires

For a typical reaction, 1 M stock solution of Se in TOP (TOP/Se) was made by dissolving 1.58 g of Se powder in 20 mL of TOP. This solution was made in a glovebox under an inert atmosphere, stirred overnight to ensure that the Se was completely dissolved, and stored in the same glovebox.

Copper acetate (30.6 mg, 0.25 mmol), 70.3 mg of indium acetate (0.25 mmol), 0.25 mL of OA, and 4 mL of TOP were combined in a 25 mL three-neck flask. The flask was attached to a Schlenk line and degassed while heating to 100 °C. After reaching 100 °C, the solution was held under vacuum for 15 min and stirred vigorously. The flask was then filled with N$_2$ and cooled to room temperature under N$_2$ flow.

In a separate 50 mL three-neck flask, 8.5 mL of TOP was added, attached to the Schlenk line, and degassed under vacuum at room temperature for 5 min. The TOP was heated to 360 °C under N_2 flow.

The Cu and In precursor solution was then combined with 0.5 mL of the 1 M TOP/Se stock solution and placed in a syringe. To initiate the reaction, 0.25 mL of a 5 mg/mL solution of Bi nanocrystals in toluene was swiftly injected into the hot TOP, followed immediately by the Cu, In, and Se precursor solution. The reaction mixture immediately turned from a light yellow color to dark brown with some black precipitate forming. The reaction proceeded for 5 min followed by removal of the heating mantle, allowing the products to cool to 50 °C.

Ten milliliters of toluene was then injected into the flask, after which this solution was removed from the Schlenk line. To separate and clean the products, this mixture was centrifuged at 4000 rpm for 5 min. The supernatant was discarded, and the precipitate was redispersed in 30 mL of toluene. This cleaning procedure was repeated three times, and the final product was redispersed in 10 mL of toluene. Tens of milligrams of CIS nanowires are obtained from typical reactions.

5.2.6 Materials Characterization

SEM images were obtained using a Zeiss Supra 40 VP SEM operated at 5 keV. The particles were suspended in chloroform and deposited by evaporation on Si substrates and imaged. Size distributions were determined by counting 300 particles for each sample imaged from random areas of the substrate.

TEM images were obtained using a Phillips 208 TEM operated at 80 keV for general imaging, or a JEOL 2010F TEM operated at 200 keV. Particles were dispersed

in chloroform at 2.5 mg/mL concentration, and 5 μL of the mixture was dropped onto carbon-coated 200 mesh copper TEM grids (Electron Microscopy Sciences).

X-ray diffraction (XRD) was carried out using a Rigaku R-Axis Spider Diffractometer with Image plate detector with Cu-kα (λ = 1.542 Å) radiation operated at 40 kV and 40 mA. Measurements were taken on particles suspended on a 0.5 mm nylon loop. Samples were scanned for 10 min while rotating at 10° per minute at 298 K in ambient atmosphere. The resulting radial data was integrated over 10-90° 2θ and plotted. Background scattering from the nylon loop was subtracted from the sample measurement.

Simultaneous thermal gravimetric analysis (TGA) and differential scanning calorimetry (DSC) measurements were performed on a Mettler-Toledo TGA/DSC1. 5-10 mL of each sample were loaded in 70 μL alumina crucibles by dropcasting from chloroform and dried in ambient atmosphere. Samples were heated from 25°C to 800°C at 5°C/min under a nitrogen atmosphere with an 80 mL/min purge.

Mass spectroscopy was analyzed on a Finnigan TSQ-700 triple quadrupole mass spectrometer by negative desorption chemical ionization (DCI) using methane as the reagent gas. A 1 mg/mL solution of Bi[N(SiMe$_3$)$_2$]$_3$ in hexane was placed in a glass NMR tube for analysis.

5.3 RESULTS AND DISCUSSION

5.3.1 Bismuth Nanocrystals

Bi[N(SiMe$_3$)$_2$]$_3$ precursor was synthesized at high purities and with good yield. A typical preparation yields 1.0-1.25 g of Bi[N(SiMe$_3$)$_2$]$_3$. Figure 5.1 shows a mass spectrum of the product. The spectrum is clean and shows only the desired product. The M/Z ratio of (a) 689 corresponds to the Bi[N(SiMe$_3$)$_2$]$_3$$^-$ ion. The Si(CH$_3$)$_3$ group is easily removed, leaving corresponding gaps of 73 in the spectrum. (b) 616, (c) 543, and (d) 470 are the

M/Z for the total molecule less one, two, and three $Si(CH_3)_3$ leaving groups, respectively. (a'-c') are spaced by 16 from the neighboring peaks, indicating CH_4 group attachments from the methane gas.
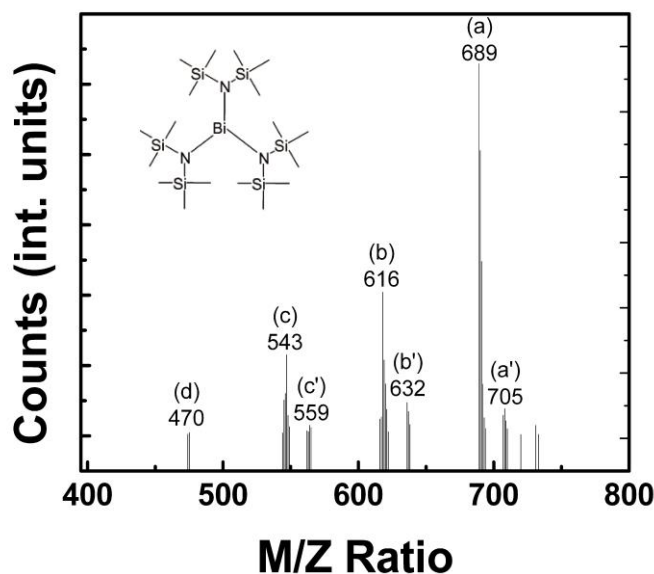
Figure 5.1: Mass spectrometry of $Bi[N(SiMe_3)_2]_3$. $Bi[N(SiMe_3)_2]_3$ was deposited from a 1 mg/mL solution in hexane and analyzed on a Finnigan TSQ-700 triple quadrupole mass spectrometer by negative desorption chemical ionization (DCI) using methane as the reagent gas. A M/Z ratio of (a) 689 corresponds to the $Bi[N(SiMe_3)_2]_3^-$ ion, (b) 616 corresponds to the ion less a $Si(CH_3)_3$ group, (c) 543 corresponds to the ion less two $Si(CH_3)_3$ groups, and (d) 470 corresponds to the ion less three $Si(CH_3)_3$ groups. (a'-c') CH_4 group attachments are also observed with each ion.

Using the pure $Bi[N(SiMe_3)_2]_3$, high quality bismuth nanocrystals were synthesized. Figure 5.2 shows Bi nanocrystals with varying Na:Bi ratios. Moderate size control was obtained by varying the ratio of $NaN(SiMe_3)_2$ to $Bi[N(SiMe_3)_2]_3$ in the reaction, from diameters of 7.9 nm up to 13.9 nm. When the $Bi[N(SiMe_3)_2]_3$ thermally decomposes, the $N(SiMe_3)_2$ groups self reduce by forming $(SiMe_3)_2N-N(SiMe_3)_2$ bond pairs. By adding excess $-N(SiMe_3)_2$ in the form of $NaN(SiMe_3)_2$, the decomposition is

accelerated and more nucleation sites are formed. This leads to smaller particle sizes. The initial polymer concentration showed little effect over size or shape control. As seen in Figure 5.2D, the particles are highly crystalline. This is confirmed by XRD in Figure 5.3.
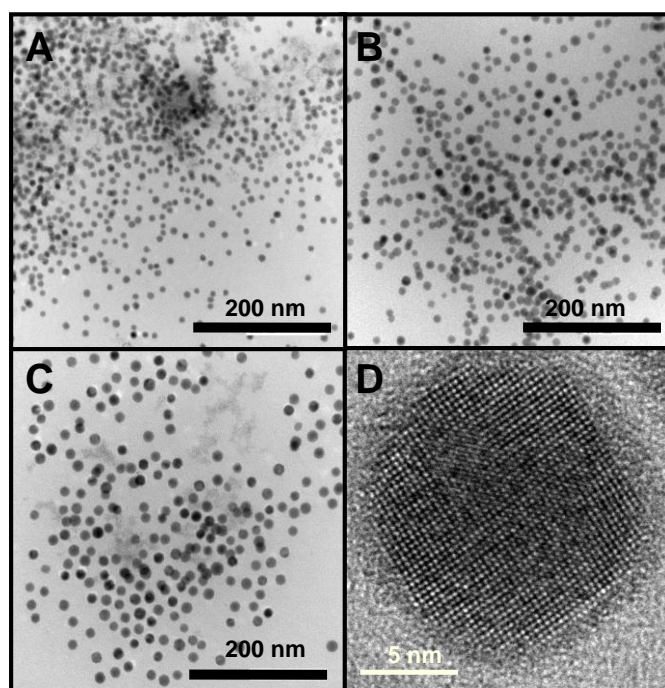
Figure 5.2: TEM images of Bi nanocrystals synthesized with Na:Bi ratios of (A) 16:1 (d = 7.9 ± 1.0 nm), (B) 8:1 (d = 10.7 ± 1.7 nm), and (C) 4:1 (d = 13.9 ± 1.0 nm). (D) High resolution TEM image of a Bi nanocrystal showing lattice fringes and high crystallinity.

Figure 5.3 show an XRD spectrum for the Bi nanocrystals. The Bi is single crystalline and in the expected rhombohedral phase. A slight broadening of the peaks is observed in (b) vs (a), corroborating TEM evidence that (b) were smaller particles.
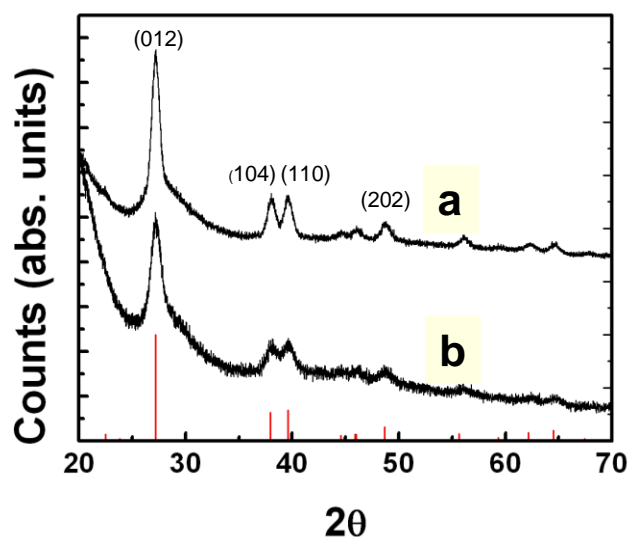
Figure 5.4: XRD spectra of Bi nanocrystals. Peaks are indexed to the rhomboheral phase of Bi. (a) 13.9 nm and (b) 7.9 nm Bi nanocrystals.

After isolating and attempting to purify the Bi nanocrystals, a large amount of polymer remained in the system. The Ganex V-216 proved extremely difficult to remove, and when following seemingly the exact same procedure inconsistent results were obtained. Figure 5.5 shows TGA analysis of three separate Bi samples. Each sample was synthesized with a 12.5% polymer/DPE initial concentration and a Na:Bi ratio of 4:1. They were each washed five times to remove as much excess polymer as possible. The resulting TGA data were vastly different. (A) was the cleanest at 20.9% Bi, (B) was next at 9.8% Bi, and (C) was the dirtiest at only 4.8% Bi! Control over final Bi/polymer ratio was never obtained. This complicates all SLS growth, as the amount of initial Bi seeds would always be variable. To circumvent this, the seeds can be used in their raw, or uncleaned, state and never removed from the initial reaction flask. This guarantees that a known mass of Bi seeds are used.
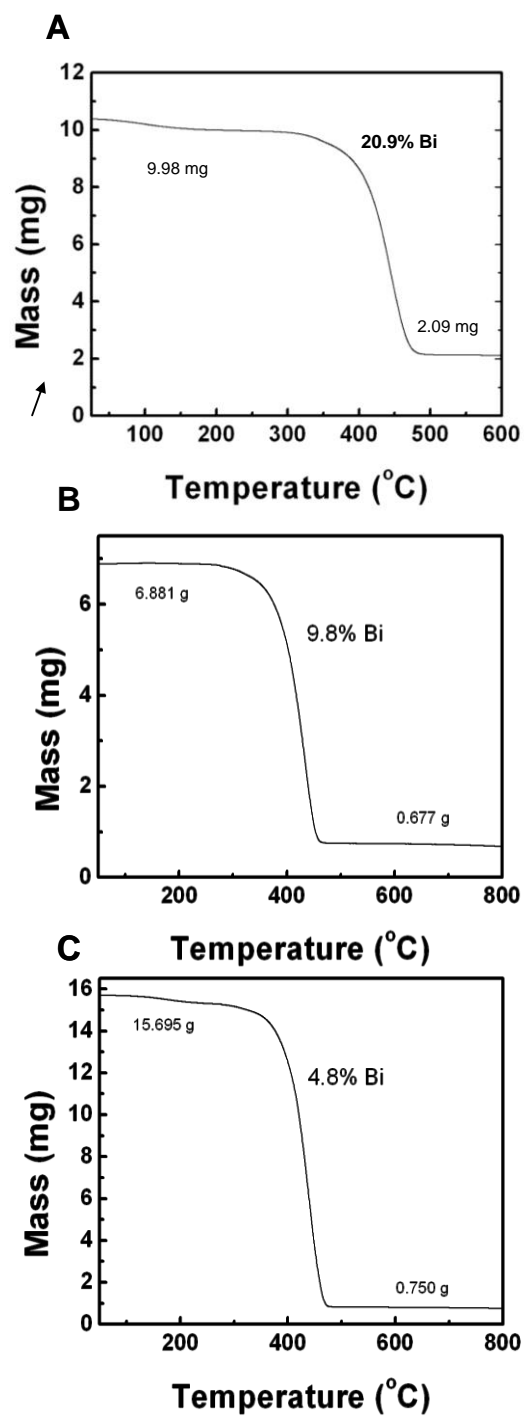
Figure 5.4: TGA of a typical Bi nanocrystal reaction after isolation of product. Samples were heated from 25°C to 800°C at 5°C/min under a nitrogen atmosphere with an 80 mL/min purge.

116

5.3.1.1 Seeding of Germanium Nanorods

Figure 5.6 shows TEM images of Ge nanorods synthesized by decomposing DPG at 350 °C in squalane in the presence of TOPO and Bi nanocrystals at a Ge:Bi molar ratio of 20:1. These nanorods had an average length of 170 ± 20 nm and diameter of 11.4 ± 1.9 nm. High resolution TEM images (Figure 5.7) confirmed that they are crystalline and composed of diamond cubic Ge. TEM also showed that nearly all of the nanorods had Bi nanocrystals at their tips. Additionally, Ge nanorods did not form when reactions were carried out in the absence of Bi nanocrystals, thus confirming that nanorod growth occurred by the SLS mechanism.
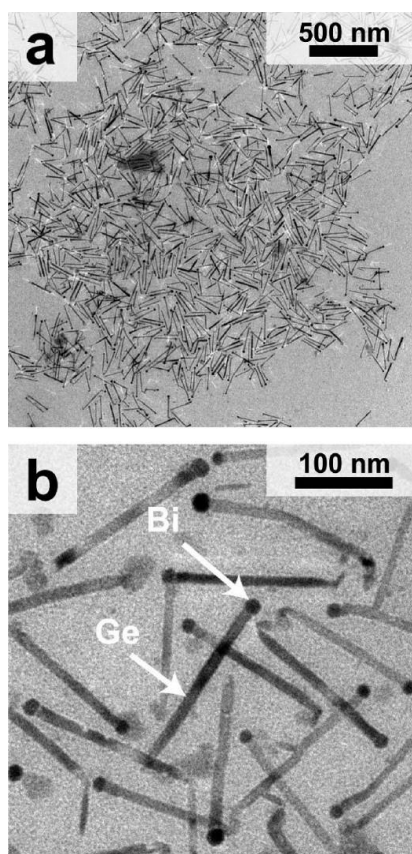
Figure 5.6: TEM images of Ge nanorods grown with a Ge:Bi molar ratio of 20:1. Most nanorods have a Bi particle at their tips, as indicated in (b).
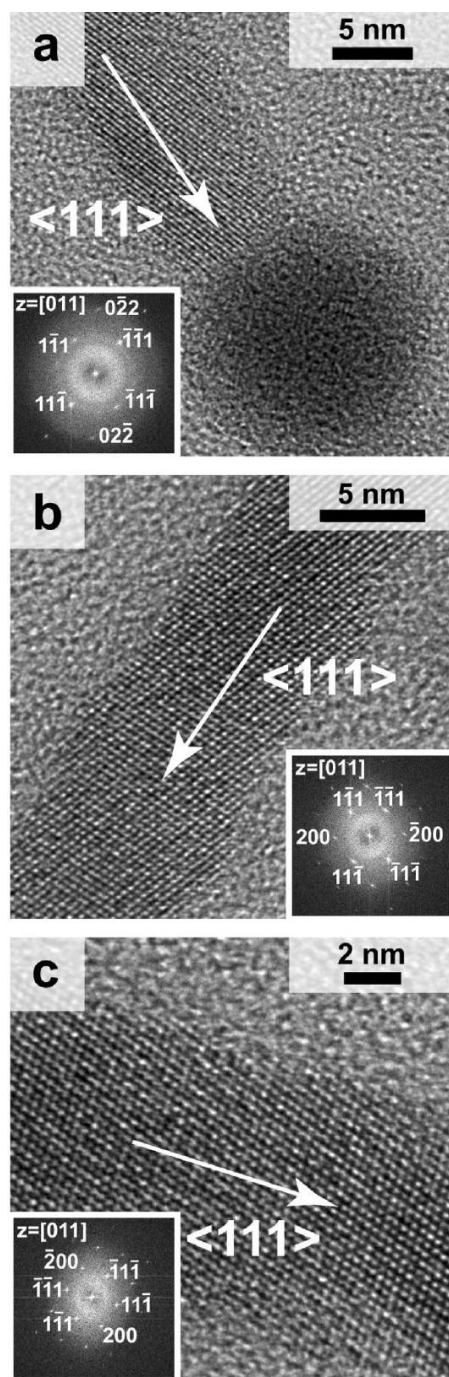
Figure 5.7: High-resolution TEM images of the Ge nanorods with their corresponding FFTs in the insets. Indexing of the FFTs is consistent with diamond cubic Ge, with each nanorod being imaged down the [011] zone axis, as indicated. The growth direction of these nanorods is <111>. A Bi particle is attached to the end of the nanorod in (a).

118

The nanorods typically grew in the <111> crystallographic direction, like those shown in Figure 5.7: of 20 nanorods that were inspected by high-resolution TEM imaging to obtain the growth direction, all 20 had <111> growth direction.

TOPO serves as a capping ligand that prevents aggregation and helps control nanorod growth. Reactions carried out without TOPO led to reaction product that was heavily aggregated and very polydisperse. The PVP/HDE polymer stabilizes the Bi nanocrystals during nanorod growth and helps prevent aggregation of the seeds during growth. When Bi nanocrystals were first synthesized and purified prior to nanorod growth, very inconsistent results were obtained due to inconsistent polymer concentrations in the final reaction. Using the crude Bi nanocrystal solution was much more consistent. The Bi nanocrystals observed at the tips of the Ge nanorods were found to have similar diameter as the nanocrystals prior to nanorod growth, indicating that there is little agglomeration of the seed particles during the reaction.

5.3.1.2 Seeding of Copper Indium Selenide Nanowires

All reactions were carried out by dispersing Bi nanocrystals in toluene and adding them to a flask of hot TOP at 360 °C in an oxygen-free atmosphere, followed by immediate injection of a reactant solution of indium acetate, copper acetate, and selenium in trioctylphosphine (TOP). After 5 min of reaction time, the nanowires have reached several micrometers in length, with an average diameter of around 20 nm. Most nanowires had Bi particles at their tips, as in Figure 5.8b, and reactions carried out without Bi nanocrystals did not yield nanowires, confirming that Bi nanocrystals were indeed seeding nanowire formation. The nanowires are crystalline, as confirmed by TEM. Elemental analysis by energy-dispersive X-ray spectroscopy (EDS) showed that the

nanowires were deficient in In, with an average composition of $Cu_{1.0}In_{0.6}Se_{2.0}$. The CIS nanowires made by this SLS process always tended to be In deficient.
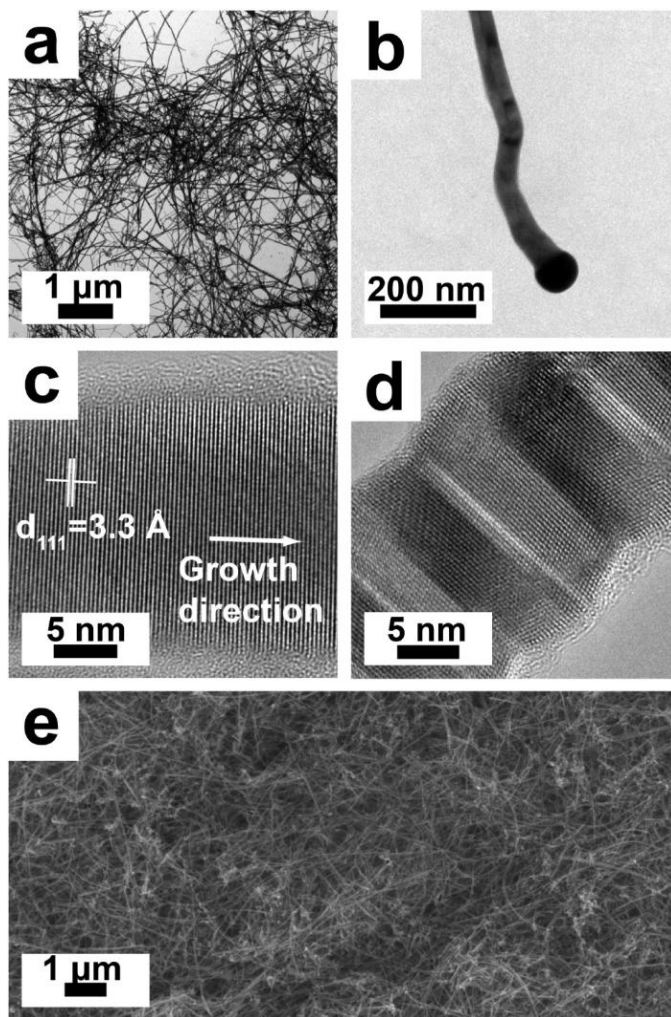
Figure 5.7: (a-d) TEM and (e) SEM images in $CuInSe_2$ (CIS) nanowires.

5.4 SUMMARY

Monodisperse, single crystalline Bi nanocrystals were synthesized using colloidal methods. A suitable polymeric replacement, Ganex V-216, was found to replace the polymer utilized in the previously published Buhro synthesis.[24] Nanocrystal size was

controlled by varying the Na:Bi ratio in the reaction mixture. Polymer concentration in "clean" nanocrystals was highly variable and seemingly independent of initial polymer quantity.

The Bi nanocrystals were used as seeds for the growth of Ge nanorods and CuInSe$_2$ nanowires. The particles were well capped and did not agglomerate during SLS growth, so wire size was controlled by varying initial Bi seed size. Consistent size control results for Ge nanorods were obtained by using "dirty" Bi; SLS growth was initiated in situ upon completion of the Bi reaction without cleaning the product first. No quantum confinement was observed on the Ge nanorods because the rods were not narrow enough. Smaller Bi seeds are needed to achieve this goal.

5.5 REFERENCES

(1)   Murray, C.B.; Kagan, C.R.; Bawendi, M.G. *Annual Review of Materials Science* **2000**, *30,* Future.

(2)   El-Sayed, M.A. *Acc. Chem. Res.* **2001**, 34, 257-264.

(3)   Sun, S.; Fullerton, E.E.; Weller, D.; Folks, L.; Moser, A. *Science* **2000**, *287,* 1989-1992.

(4)   Puntes, V.; Krishnan, K.M.; Alivisatos, A.P. *Science* **2001**, *291*, 2115-2117.

(5)   Dong, A.; Wang, F.; Daulton, T.L.; Buhro, W.E. *Nano Letters* **2007**, *7,* 1308-1313.

(6)   Wang, F.; Buhro, W.E. *J. Am. Chem. Soc.* **2007**, *129,* 14381-14387.

(7)   Fanfair, D.D.; Korgel, B.A. *Crystal Growth and Design* **2005**, *5*, 1971-1976.

(8)   Holmes, J.D.; Johnston, K.P.; Doty, R.C.; Korgel, B.A. *Science* **2000**, *287,* 1471.

(9)   Hanrath, T.; Korgel, B.A. *J. Am. Chem. Soc.* **2002**, *124*, 1424-1429.

(10)   Brust, M.; Walker, M.; Bethell, D.; Schiffrin, D.J.; Whyman, R. *J. of the Amer. Chem. Soc. – Chem. Comm.* **1994**, *7*, 801-802.

(11)   Collier, C.P.; Vossmeyer, T.; Heath, J.R. *Annual Rev. of Phys. Chem.* **1998**, *49*, 371-404.

(12)   Jezequel, G.; Thomas, J. *Phys. Rev. B* **1997**, *56*, 6620.

(13)   Liu, K.; Chien, C.L. *Phys. Rev. B* **1998**, *58*, 681-684.

(14)   Heremans, J.; Thrush, C.M.; Zhang, Z.; Sun, X.; Dresselhaus, M.S.; Ying, J.Y.; Morelli, D.T. *Phys Rev. B* **1998**, *58*, 91-95

(15)   Heremans, J.; Thrush, C.M.; Lin, Y.M.; Chroin, S.; Zhang, Z.; Dresselhaus, M.S.; Mansfield, J.F. *Phys. Rev. B* **2000**, *61*, 2921-2930

(16)   Lin, Y.M.; Sun, X.; Dresselhaus, M.S. *Phys Rev. B* **2000**, *62*, 4610-4623.

(17)   Chu, H.T.; Zhang, W.J. *J. Phys. Chem. Solids* **1992**, *53*, 1059-1065.

(18)   Zhou, G.; Li, L.; Li, G.H. *J. Appl. Phys.* **2011**, *109*, 114311-114318.

(19)   Lee, S.; Ham, J.; Jeon, K.; Noh, J.S. Lee, W. *Nanotechnology* **2010**, *21*, 405701-405706.

(20)   Qi, J.; Shi, D.; Jiang, X. *Chem. Phys. Lett.* **2008**, 4*60*, 266-271.

(21)   Wang, Y.; Xia, Y. *Nano Letters* **2004**, *4*, 2047-2050.

(22)   Foos, E.E.; Stroud, R.M.; Berry, A.D.; Snow, A.W.; Armistead, J.P. *J. Am. Chem. Soc.* **2000**, *122*, 7114-7115.

(23)   Fanfair, D.D.; Korgel, B.A. *Chem. Mater.* **2007**, *19*, 4943-4948.

(24)   Wang, F.; Tang, R.; Yu, H.; Gibbons, P.C.; Buhro, W.E. *Chem. Mater.* **2008**, *20*, 3656-3662.

(25)   Gudiksen, M.S.; Lieber, C.M. *J. Am. Chem. Soc.* **2000**, *122*, 8801-8802.

(26)   Chockla, A.M.; Harris, J.T.; Korgel, B.A. *Chem. Mater.* **2011**, *23*, 1964-1970.

(27)   Steinhagen, C.; Akhavan, V.A.; Goodfellow, B.W.; Panthani, M.G.; Harris, J.T.; Holmberg, V.C.; Korgel, B.A. *ACS Appl. Mater. Interfaces* **2011**, *3*, 1781-1785.

(28)   Cowley, A. H. In Inorganic Syntheses; John Wiley & Sons: New York, NY, 1997; p 100.

Chapter 6: Unique Magnetic Properties of Au Nanoparticles

6.1 INTRODUCTION

As demands for smaller and faster electronics continue to increase, metallic nanoparticles have been a focus of research due to their unique properties. Their small size gives the nanoparticles properties different from their bulk counterparts, both from the large surface to volume ratio and discretization of the energy spectrum.[1] Nanoscale size also affects the magnetic properties of materials. A phenomenon called superparamagnetism has been known for years to develop in ferromagnetic materials when the particle size is below that of the bulk magnetic domain,[2,13] but in the last decade it has even been shown that diamagnetic materials can exhibit para- and even ferromagnetic characteristics when reduced to the nanoparticle regime.[3] In fact, it is now believed to be a universal feature of inorganic nanoparticles.[4] This effect is different than the superparamagnetic effect, which is a "size effect." The magnetic moment per atom results from both spin and orbital contributions. The large proportion of surface atoms in nanocrystals can significantly increase the orbital magnetic moment per atom, resulting in significant differences in magnetic properties from the bulk.[5] Increased orbital magnetic moments in nanocrystals can be particularly influential for nanocrystals of metals like Au and Pt that are not ferromagnetic in the bulk. The physics behind this transition, however, is up for debate.

Currently, there are multiple theories in regard to the magnetism of Au nanoparticles. Yamamoto, et. al. propose that Au nanoparticles display superparamagnetism due to surface magnetization and that it is quenched by the addition of ligands to the surface.[6] By this mechanism, even bulk Au has a small ferromagnetic contribution from surface states that are overpowered by the diamagnetic core, and thus

123

undetectable by bulk characterization techniques. The nature of the ligand-metal bond has also been shown to be important, apparently influencing the spin-orbit coupling.[7-10] Crespo, et. al. propose that Au nanoparticles actually display ferromagnetism but only when capped by thiols.[7] They reported room temperature ferromagnetism from 1.4 nm diameter Au nanocrystals capped with dodecanethiol and proposed that strong Au-thiol bonding was responsible. Consistent with this hypothesis, they found that Au nanocrystals coated with the weaker bonding ligand tetraoctylammonium bromide were not ferromagnetic.[7,10] They attribute this characteristic to hole localization near the Au-S bonds, giving rise to permanent magnetism. Gonzalez et al.[11] recently calculated the magnetic properties expected for a 13 atom Au nanocluster chemisorbed to a thiol or amine, which supported the findings of Crespo et al.[7] Magnetic measurements performed by Hori and co-workers on similar Au nanocrystals did not exhibit ferromagnetism, but did show paramagnetism.[8] These competing theories illustrate the need for a comprehensive model to predict the magnetic properties of metallic nanocrystals. Hori and coworkers have also reported enhanced paramagnetism in Pt and Pd[12] nanocrystals smaller than 2.5 nm.

In this chapter, the size dependence of the magnetic properties of thiol-capped gold nanocrystals was studied. Thiol-capped gold nanocrystals were synthesized using colloidal methods with diameters under 2 nm. The magnetic susceptibility of the nanocrystals was measured using a superconducting quantum interference device (SQUID) at room temperature and 5 Kelvin (K).[14] The thiol-coated gold nanocrystals did not exhibit ferromagnetism, but did display paramagnetism.

124

6.2 EXPERIMENTAL DETAILS

6.2.1 Reagents

Dodecanethiol ($C_{12}H_{25}SH$, ≥98%), gold tetrachloroaurate trihydrate ($HAuCl_4 \cdot 3H_2O$, 99.9+%), sodium borohydride ($NaBH_4$, 98+%), tetraoctylammonium bromide ($C_{32}H_{68}BrN$, TOAB, 98%), toluene (C_7H_8, ACS grade), ethanol (C_2H_5OH, ACS grade), methanol (CH_3OH, ACS grade), and chloroform ($CHCl_3$, ACS grade) were purchased from Sigma-Aldrich. Triply distilled deionized water (DI-H_2O) filtered with an 18.2 MΩ-cm resistance Barnstead E-pure unit was used for all aqueous preparations. All chemicals were used as received.

6.2.2 Synthesis of Au Nanoparticles

2 nm diameter dodecanethiol-coated Au nanocrystals were synthesized by modifying a previously described literature method.[15] In a typical procedure, 2.188 g (4 mmol) of tetraoctylammonium bromide (TOAB) was dissolved in 80 mL of toluene in a 125 mL Erlenmeyer flask. In a separate Erlenmeyer flask, 305.8 mg (0.77 mmol) of tetrachloroaurate trihydrate was dissolved into 30 mL of DI-H_2O. The TOAB solution was placed on a stir plate and a ¾" cylindrical Teflon stir bar was added to the Erlenmeyer flask. The solution was stirred moderately at a rate of 600 RPM. The aqueous tetrachloroaurate solution was added with the stirring organic TOAB solution and an emulsion was formed. After 1 hour, the mixture was poured into a 250 mL separatory funnel and the aqueous and organic phases separated within 1 minute. The organic layer was collected in a clean 125 mL Erlenmeyer flask. The aqueous layer was discarded. The toluene solution containing gold chloride ions was placed back on the stir plate and stirred moderately. 0.201 mL (0.84 mmol) of dodecanethiol was added to the gold chloride solution and stirred for 5 minutes. In a 50 mL Erlenmeyer flask, 378.0 mg

(10 mmol) of sodium borohydride was dissolved in 25 mL of DI-H_2O and slowly added to the gold chloride solution. The solution immediately turned dark red/purple/black, indicating the formation of 2 nm Au nanocrystal. This mixture was stirred for 3 hours and poured into a 250 mL separatory funnel. The aqueous phase was discarded and the organic Au nanocrystal dispersion was collected in 3-50 mL centrifuge tubes for purification. The Au nanocrystal dispersion was centrifuged at 8,000 RPM (8228g RCF) for 5 minutes at room temperature to precipitate poorly capped nanocrystals and any solid byproducts. The precipitate was discarded and the supernatant was collected in centrifuge tubes. 20 mL of methanol was added to each centrifuge tube, followed by centrifugation at 10,000 RPM (12857g RCF) for 5 minutes at 10 °C to precipitate the Au nanocrystals. The nanocrystals collected as a pellet on the sidewall of the centrifuge tube. The supernatant was discarded. The Au nanocrystals were redispersed in 5 mL of chloroform and transferred to a centrifuge tube. 10 mL of methanol was added and the solution was centrifuged again at 10000 RPM for 5 minutes at 10 °C. The supernatant was discarded. The Au nanocrystals were redispersed in 1 mL of chloroform and transferred to a glass vial. Approximately 150 mg of 2 nm diameter Au nanocrystals were obtained.

6.2.3 Materials Characterization

The Au nanocrystals were characterized using transmission electron microscopy (TEM), small angle X-ray scattering (SAXS), and Superconducting Quantum Interference Device (SQUID) magnetometry techniques. TEM samples were prepared by dropcasting 5 μL of Au nanocrystal dispersions in chloroform onto copper 200 mesh carbon TEM grids (Electron Microscopy Sciences). TEM images were acquired digitally

on a Phillips EM208 TEM with 80 kV accelerating voltage on an AMT Advantage HR 1 MB digital camera.

XRD was performed on a Bruker-Nonius D8 Advance Diffractometer using Cu K_α radiation (λ=1.5418 Å) with samples on quartz substrates. Samples were rotated while scanning for ~10 hrs at 12°/min in 0.02° increments between 10–90° 2θ.

SAXS was performed on a home built system using a rotating copper-anode generator (Bruker Nonius) operated at 3.0 kW in vacuum. Scattered photons were collected on a multiwire gas-filled detector (Molecular Metrology, Inc.). The scattering angle was calibrated using silver behenate standard and all experimental data was corrected for background scattering. A Kapton liquid cell filled with dilute dispersions of Au nanocrystals in hexane was used to obtain the solution phase SAXS data.

Magnetic properties were measured with a SQUID (Quantum Design) magnetometer.[13] 90 - 150 mg of Au nanocrystals were transferred into gelatin capsules (Capsuline #4). The remaining volume in the capsule was filled with cotton. The magnetization measured in units of emu/g was converted to magnetization in units of Bohr magnetons per Au nanocrystal (μ_B/Au nanocrystal) by multiplying the weight of the sample by the conversion factor 1.08 x 10^{20} μ_B/emu and dividing by the estimated weight of an individual nanocrystal. The weight of a Au nanocrystal was estimated from the Au core diameter determined by TEM and SAXS and an estimated dodecanethiol capping ligand coverage of 78.5% with a footprint of 0.2 nm^2 as previously reported.[16] The Au density was taken as 19.32 g/cm^3.

Au nanocrystals were also investigated with inductively coupled plasma mass spectrometry (ICP-MS), inductively coupled plasma atomic emission spectroscopy (ICP-AES), atomic absorption spectroscopy (AAS) to determine if trace magnetic impurities were present. Immediately after a SQUID measurement, the whole gelatin capsule with

Au nanocrystals and cotton were digested in pure high-grade nitric acid and hydrochloric acid. The digestion took approximately 3-5 days and the residual cotton was strained from the solution. The digestion solution was then diluted with DI-H_2O to an average Au concentration of 0.001 mg/mL. Iron, nickel, cobalt, and manganese standards were prepared in a similar fashion for comparison. A method of standard additions was used to deduce any Fe, Ni, Co, and Mn magnetic impurities in the Au nanocrystal sample.

6.3 RESULTS AND DISCUSSION

6.3.1 Synthesis of Au Nanocrystals

Au nanocrystals below 2 nm in diameter were synthesized with high monodispersity and high selectivity using the Brust method.[15] Figure 6.1 shows a TEM image and SAXS data of 1.6 nm Au nanocrystals. TEM shows the nanocrystals are not aggregated and form a monolayer. The included histogram shows a Gaussian distribution of particle sizes with an average diameter of 1.61 ± 0.42 nm. The shown SAXS data was taken of Au nanocrystals in hexane. The data was fitted to a spherical form factor model using a Gaussian distribution. The best model fit was found at 1.60 ± 0.41 nm, confirming the TEM particle count.
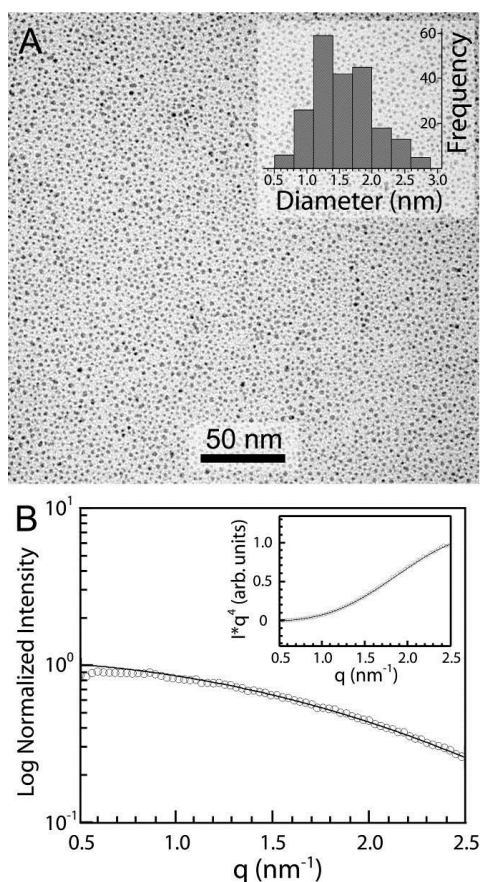
Figure 6.1: (A) TEM image of dodecanethiol-capped Au nanocrystals. The inset shows a histogram of the nanocrystal diameter distribution with average diameter of 1.61 ± 0.42 nm determined by measuring over 300 within the TEM image. (B) Small angle x-ray scattering of the Au nanocrystals dispersed in toluene (1 mg/mL). The Porod plot of the data is shown in the inset. The (○) data was best fitted to a (—) spherical form factor model with Gaussian size distribution and average diameter of 1.60 ± 0.41 nm

Figure 6.2 shows a TEM image and SAXS data of smaller, 1.4 nm Au nanocrystals. TEM shows the nanocrystals are not aggregated and form a monolayer. The included histogram shows a Gaussian distribution of particle sizes with an average diameter of 1.42 ± 0.41 nm. The shown SAXS data was taken of Au nanocrystals in hexane. The data was fitted to a spherical form factor model using a Gaussian distribution. The best model fit was found at 1.30 ± 0.34 nm, smaller than found by the

129

TEM particle count. The fit is not as good as in the 1.6 nm Au nanoparticles because it is pushing the lower limit for size detection, but both TEM count and SAXS confirm that the particles are smaller than 1.6 nm Au.
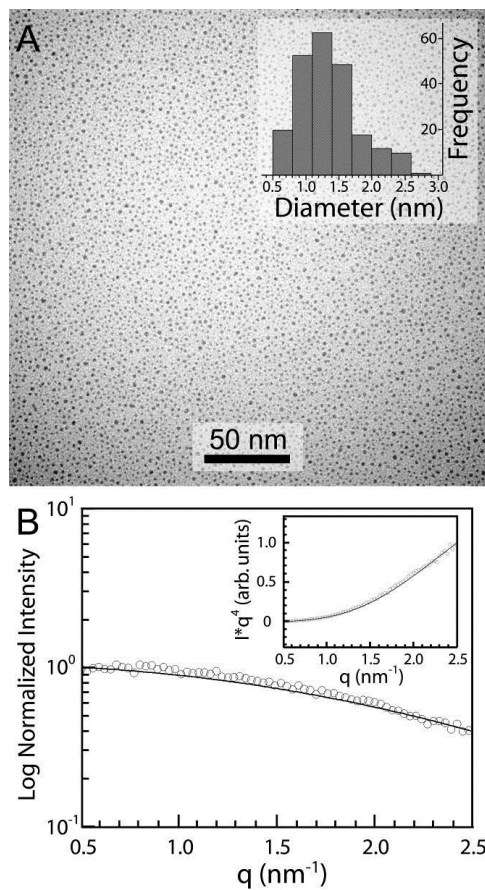
Figure 6.2: (A) TEM image of dodecanethiol-capped Au nanocrystals. The inset shows a histogram of the nanocrystal diameter distribution with average diameter of 1.42 ± 0.41 nm determined by measuring over 300 in the TEM image. (B) Small angle x-ray scattering (SAXS) of the Au nanocrystals dispersed in toluene (1 mg/mL). A porod plot is shown in the inset. The ($\circ$) data was best fitted to a (—) spherical form factor model with gaussian size distribution and average diameter of 1.30 ± 0.34 nm.

6.3.2 Magnetic Properties of Au Nanocrystals

The magnetic properties of 1.6 nm and 1.3 nm Au nanocrystals were investigated using a SQUID magnetometer. Both field-dependent and temperature-dependent sweeps were run for the samples. Figure 6.3 shows the results for the 1.6 nm Au nanocrystals.
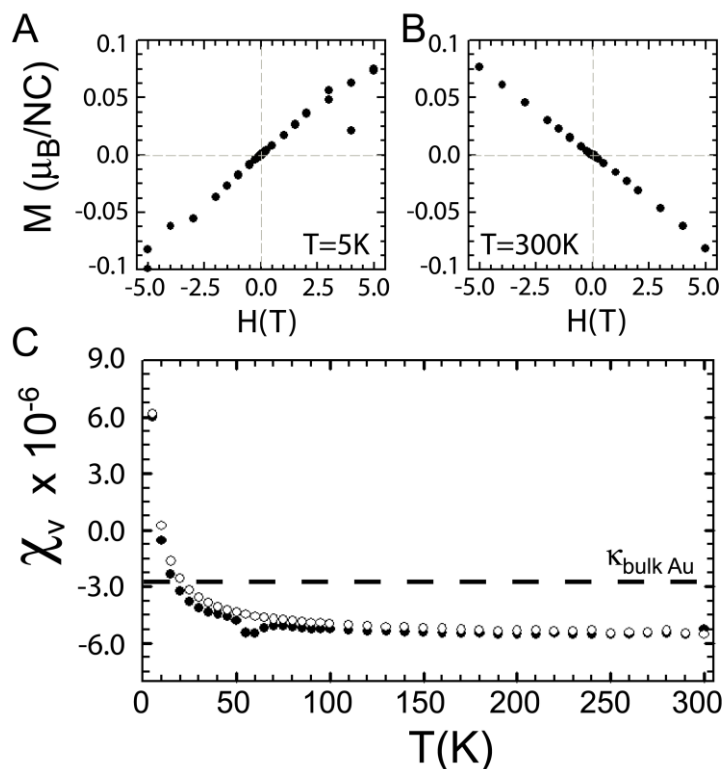
Figure 6.3: Field-dependent magnetization of the 1.60 ± 0.41 nm diameter dodecanethiol coated Au nanocrystals measured at (A) 5K and (B) 300K. (C) The temperature-dependent ($\circ$) zero field cooled (ZFC) and ($\bullet$) field-cooled (FC) susceptibility (0.1T applied field) of the nanocrystals. The dashed line represents the diamagnetic susceptibility of bulk Au. The magnetic data is corrected for the capping ligand weight, assuming 78.5% surface coverage.

The field-dependent sweeps were taken at temperatures of 5 K and 300 K. At 5 K, the 1.6 nm Au nanocrystals show a positive correlation between resulting magnetization and applied field. The 5 K sweep also shows no hysteresis. This indicates that the nanocrystals are paramagnetic. Even at 5.0 T applied field, the magnetization never

131

saturates though a slight flattening of the slope is observed, reaching a maximum of 0.08 Bohr magnetons per nanocrystal (μ_B/NC). The 300 K sweep shows a negative correlation between magnetization and applied field, indicating that the nanocrystals are diamagnetic at room temperature. The temperature-dependent scans tell the same story. Both the FC and ZFC scans show negative susceptibility, even lower than bulk gold, for most of the scan. At temperatures below 10 K, the samples have positive magnetic susceptibility. The FC and ZFC scans never deviate from one another, again confirming paramagnetic behavior rather than ferromagnetic or superparamagnetic behavior. Figure 6.4 shows the results for the 1.3 nm Au nanocrystals.
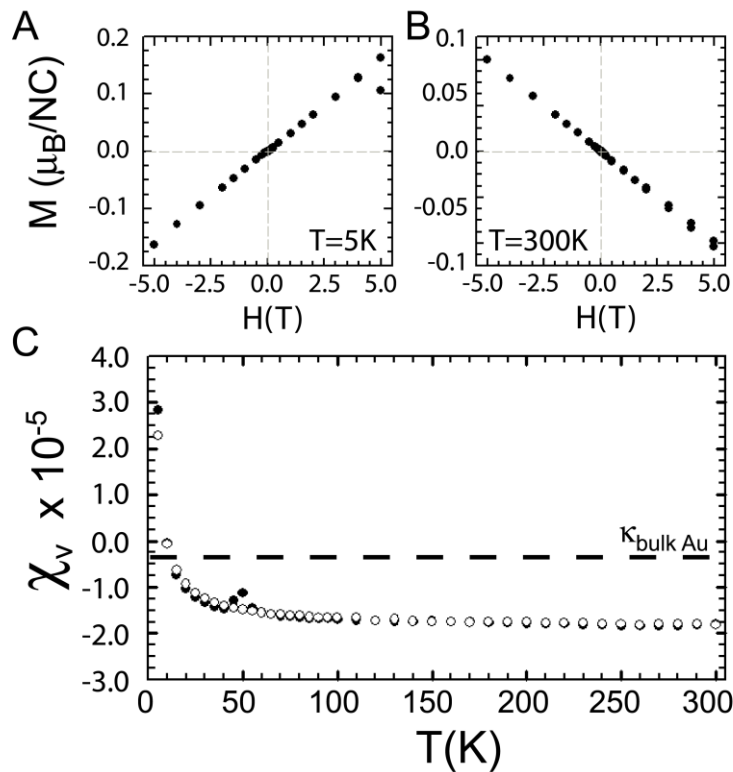
Figure 6.4: Field-dependent magnetization of the 1.30 ± 0.34 nm diameter dodecanethiol coated Au nanocrystals measured at (A) 5K and (B) 300K. (C) The temperature-dependent (○) zero field cooled (ZFC) and (●) field-cooled (FC) susceptibility (0.1T applied field) of the nanocrystals. The dashed line represents the diamagnetic susceptibility of bulk Au. The magnetic data is corrected for the capping ligand weight, assuming 78.5% surface coverage.

The field-dependent sweeps were again taken at temperatures of 5 K and 300 K. At 5 K, the 1.3 nm Au nanocrystals show a positive correlation between resulting magnetization and applied field. The 5 K sweep also shows no hysteresis. This indicates that the nanocrystals are paramagnetic. Even at 5.0 T applied field, the magnetization never saturates though a slight flattening of the slope is observed, reaching a maximum of 0.18 μ_B/NC. The 300 K sweep shows a negative correlation between magnetization and applied field, indicating that the nanocrystals are diamagnetic at room temperature. The temperature-dependent scans tell the same story. Both the FC and ZFC scans show negative susceptibility, even lower than bulk gold, for most of the scan. At temperatures below 10 K, the samples have positive magnetic susceptibility. The FC and ZFC scans never deviate from one another, again confirming paramagnetic behavior rather than ferromagnetic or superparamagnetic behavior. Though both samples were paramagnetic, there were noticeable differences between the two sizes. The 1.6 nm Au nanocrystals showed a maximum susceptibility of 0.08 μ_B/NC while the 1.3 nm Au nanocrystals had a maximum of 0.18 μ_B/NC. This increase of over two-fold is attributed to the decreased size of the nanocrystals.

To insure there are no potential magnetic impurities, both samples were analyzed by mass spectroscopy. Crespo, *et al.* showed that Fe impurities actually reduce the ferromagnetic in Au nanocrystals, which is counterintuitive.[17] The results for the 1.6 nm and 1.3 nm samples are shown in Table 6.1 and Table 6.2, respectively. Neither Fe nor Ni

was detectable via ICP-MS, but statistical analysis determined that the lower detection limit of Ni was 1.2 ppb and Fe was 95.7 ppb. Further analysis was therefore necessary to rule out Fe and Ni as magnetic impurities. ICP-AES and AA spectroscopy were used to do this. Corroborating the ICP-MS data, ICP-AES did not detect Mn or Co. Additionally, Ni was not detectable eliminating these elements as possible impurities (The lower detection limit for the ICP-AES was 1 ppb). However, trace amounts of Fe were detected using ICP-AES. To determine the specific concentration of Fe, AA spectroscopy was used. AA spectroscopy found that less than 0.018 Fe atoms were associated with each 1.6 nm Au nanocrystal and less than 0.034 Fe atoms per 1.3 nm Au nanocrystal. Assuming Mn, Fe, Co, and Ni atoms can contribute 3, 4, 3, 2 Bohr magnetons/atom respectively, the mass spec and spectroscopy confirms that magnetic impurities do not contribute to the magnetic data as seen in Figure 6.3 and Figure 6.4. The values marked with an (*) are the lower detection limit for the respective trace impurity analysis. All impurities must have a concentration lower than the value seen below. Additionally, ICP-Ms is notorious for its inability to detect Fe. Therefore, having such a high lower limit is not so surprising. It is preferred to use ICP-AES or AA to conclude Fe impurity.

	ICP-MS determined Atomic impurity per Au nanocrystal	ICP-AES determined atomic impurity per Au nanocrystal	AA determined atomic impurity per Au nanocrystal
Mn	0.005	< 0.006*	-
Fe	<5.465*	0.007	0.018
Co	0.002	<0.005*	-
Ni	<0.064*	<0.002*	-

Table 6.1: Trace magnetic impurities (atomic basis) per Au nanocrystal determined by ICP-MS, ICP-AES, and AA. Each nanocrystal has approximately 68 Au atoms assuming the average diameter is 1.3 nm, the density of Au is 19.3g/cm^3, and the nanocrystal is spherical.

	ICP-MS determined Atomic impurity per Au nanocrystal	ICP-AES determined atomic impurity per Au nanocrystal	AA determined atomic impurity per Au nanocrystal
Mn	0.005	< 0.005	-
Fe	<5.465*	0.007	0.034
Co	0.001	<0.005	-
Ni	<0.056	<0.005	-

Table 6.2: Trace magnetic impurities (atomic basis) per Au nanocrystal determined by ICP-MS, ICP-AES, and AA. Each nanocrystal has approximately 127 Au atoms assuming the average diameter is 1.6 nm, the density of Au is 19.3g/cm^3, and the nanocrystal is spherical.

6.4 SUMMARY AND CONCLUSIONS

Small Au nanocrystals were investigated with regards to their size dependent magnetic properties. Dodecanethiol capped Au nanocrystals with diameters of 1.4 nm and 1.6 nm both showed paramagnetic characteristics at low temperatures, which is unexpected as bulk gold is diamagnetic. Both sets of Au nanocrystals only displayed paramagnetic behavior at temperatures < 10 K, confirmed by FC, ZFC, and field-dependent scans at 300 K and 5 K. These nanocrystals were tested with a variety of mass spectroscopy techniques to determine that no appreciable magnetic impurities were present. Contrary to previous studies, the Au displayed no ferromagnetism. The 1.6 nm Au nanocrystals had a maximum magnetic susceptibility or 0.08 μ_B/NC while the smaller 1.3 nm particles displayed 0.18 μ_B/NC – more than a two-fold increase. It is still undetermined whether this is a pure surface effect or due quantization of spin states.

6.5 REFERENCES

(1) Volokitin, Y.; Sinzig, J.; deJongh, L.J.; Schmid, G.; Vargaftik, M.N.; Moiseev, I.I. *Nature.* **1996,** *384*, 621-623.

(2) Gittleman, J. I.; Abeles, B.; Bozowski, S. *Phys. Rev. B.* **1974**, *9*, 3891-3897.

(3) Hori, H.; Teranishi, T.; Nakae, Y.; Seino, Y.; Miyake, M.; Yamada, S. *Phys. Lett. A.* **1999,** *263,* 4-6.

(4) Sundaresan, A.; Rao,C. *Nanotoday.* **2009,** *4,* 96.

(5)   Nealon, G.L.; Donnio, B.; Greget, R.; Kappler, J.P.; Terazzi, E.; Gallani, J.L. *Nanoscale*. **2012**, *4*, 5244-5258.

(6)   Yamamoto, Y.; Miura, T.; Suzuki, M.; Kawamura, N.; Miyagawa, H.; Nakamura, T.; Kobayashi, K.; Teranishi, T.; Hori, H. *Phys. Rev. Lett.* **2004**, *93*, 116801.

(7)   Crespo, P. ; Litran, R. ; Rojas, T.C. ; Multigner, M. ; de la Fuente, J.M. ; Sanchez-Lopez, J.C. ; Garcia, M.A. ; Hernando, A. ; Penades, S. ; Fernandez, A. Phys. *Rev. Lett.* **2004**, *93*, 087204.

(8)   Nunomora, N.; Hori, H.; Teranishi, T.; Miyake, M.; Yamada, S. **1998**, *249*, 5-6.

(9)   Ayuela, A.; Crespo, P.; Garcia, M.A.; Hernando, A.; Echenique, P.M. *New Journal of Physics*. **2012**, *14*, 013064.

(10)   Garitaonandia, J.S.; Insausti, M.; Goikolea, E.; Suzuki, M.; Cashion, J.D.; Kawamura, N.; Ohsawa, H.; de Muro, I.G.; Suzuki, K.; Plazaola, F.; Rojo, T. *Nano Letters.* **2008**, *8*, 661-667.

(11)   Gonzalez, C. ; Simon-Manso, Y. ; Marquez, M. ; Mujica, V. *J. of Phys. Chem. B*. **2006**, *110*, 687-691.

(12)   Hori, H. ; Yamamoto, Y. ; Iwamoto, T. ; Miura, T. ; Teranishi, T. ; Miyake, M. *Phys. Rev. B*. **2004**, *69*, 174411.

(13)   Billas, I.M.L. ; Becker, J.A. ; Chatelain, A. ; Deheer, W.A. *Phys. Rev. Lett.* **1993**, *71*, 4067-4070.

(14)   M. Bode, *Rep. Prog. Phys.* **2003**, *66*, 523

(15)   Brust, M.; Walker, M.; Bethell, D.; Schiffrin, D.J.; Whyman, R. *J. of the Amer. Chem. Soc. – Chem. Comm.* **1994**, *7*, 801-802.

(16)   Daniel, M.C. ; Astruc, D. *Chemical Reviews*. **2004**, *104*, 293-346.

(17)   Crespo, P. ; Garcia, M.A. ; Pinel, E.F. ; Multigner, M. ; Alcantara, D. ; de la Fuente, J.M. ; Penades, S. ; Hernando, A. *Phys. Rev. Lett.* **2006**, *97*, 177203.

Chapter 7: Conclusion and Future Research Directions

7.1 CONCLUSIONS

7.1.1 Hydrogenated Amorphous Silicon (a-Si:H) Colloids

Colloidal a-Si:H particles can be produced by Si_3H_8 decomposition in sc-hexane with a fairly wide range of size, hydrogen content and structural order, depending on the synthesis temperature, pressure and reactant concentration. Higher temperature reactions produced particles with more structural order and less associated hydrogen. Particles made at 450^oC or higher were also slightly agglomerated. Raman spectroscopy was used as a sensitive probe to examine structural differences in the particles made at different temperature. The excitation laser used for Raman spectroscopy had enough power to crystallize particles that were synthesized at temperatures higher than 380^oC due to the presence of intermediate order networks randomly distributed and small 1-2 nm ordered Si clusters that act as seeds for further crystallization. As far as we are aware, the reported method is the only available solution-phase approach to a-Si:H particles. Future work now involves examining their properties, including electrochemical studies on the potential of a-Si particles as a recipient for Li^+ implantation and the effects of hydrogen content on this process. The high hydrogen contents will also be tested for ease of removal and potential cyclability.

7.1.2 Enhanced Lithiation of Si Nanostructures Through Increased Surface Conductivity

Cycle life and lithiation capacity of Si nanostructures can be greatly improved by enhancing their surface conductivity. Two methods for enhancing this conductivity were presented. a-Si:H particles initially showed low capacity for lithiation as an anode material. A unique chemical process to coat Cu over pre synthesized a-Si:H particles has

been developed. Cu nanoparticles were synthesized on the surface of the a-Si:H particles by a hydrogen enhanced reduction of Cu acetate. The lithiation capacity of a-Si:H particles increased from 84 mA h/g to 600 mA h/g, a seven-fold increase, after addition of Cu nanoparticles,. The presence of Cu helps to suppress the solvent decomposition and enhance electrical wiring between the particles. *In situ* Raman measurements elucidate the fundamental nature of the lithiation/delithiation process taking place in a-Si:H particles and the role of the Cu layer in these processes. This chemical approach of coating Cu over a-Si:H particles shows great potential towards developing materials for lithium ion batteries. Though still not near the theoretical maximum capacity of Si, the large increase seen after increasing the surface conductivity of the particles is promising and applicable to other systems.

A non-woven fabric of Si nanowires is also reported. The fabric has the look and feel of tissue paper, yet is composed entirely of crystalline Si. Annealing the nanowire fabric at 900°C under reducing atmosphere (forming gas) led to good performance as an anode in a Li ion battery without adding carbon binder due to increased surface conductivity. This increased the lithiation capacity of the wires after 20 cycles from 8 mA h/g (unannealed) to 804 mA h/g (900 ^{o}C anneal) – an amazing 100-fold capacity increase. The key to their good performance is the presence of a thin electrically conductive carbon layer on the nanowires from reduction of the polyphenylsilane shell. When the nanowires were annealed above 900 ^{o}C, the battery performance diminished due to the formation of a surface barrier layer of SiO_2 and SiC under the conducting carbonaceous coating that prevented efficient lithiation and delithiation. These two studies shows that surface composition of Si nanostructures plays a critical role in their effectiveness as an anode material in a LIB.

138

7.1.3 Amorphous Silicon Coated Germanium Core-Shell Nanowires

Though Si offers higher theoretical capacities than Ge, in practice Si suffers from poor conductivity and pulverization of the anode material. Ge offers higher conductivities and isotropic expansion. a-Si also exhibits isotropic expansion and less pulverization that its crystalline counterpart. The best of both systems is realized through the use of heterostructure. By coating Ge nanowires with a-Si, the a-Si has support of a more conductive matrix and decreased lithium ion diffusion lengths. a-Si coated Ge nanowires were successfully synthesized through a post-reaction decomposition of trisilane on the surface of the wires. The thickness of the a-Si shell was controlled by varying the ratio of Si to Ge in the reaction. Shells were grown up to 40 nm thick with even and complete coverage of the nanowire surfaces. The a-Si shells enhanced the lithiation capacity of the wires while maintaining high reversibility. With a 40 nm shell, a lithiation capacity of 1800 mA h/g after 20 cycles was maintained – higher than the theoretical capacity of Ge alone.

Monophenylsilane was also used to coat the Ge nanowires with significantly different results. Despite various MPS treatments, little variation in coating was noticed. HRTEM did identify a thin amorphous shell on the nanowire surface, and Raman identified a small carbonaceous coating. After incubation, capacity of the Ge NWs increased due to reduction of the coating to conductive carbon. Attempts to anneal the NW paper were unsuccessful.

7.1.4 Synthesis of Bi Nanoparticles and SLS Growth Applications

Monodisperse, single crystalline Bi nanocrystals were synthesized using colloidal methods. A suitable polymeric replacement, Ganex V-216, was found to replace the polymer utilized in the previously published Buhro synthesis.[24] Nanocrystal size was controlled by varying the Na:Bi ratio in the reaction mixture. Polymer concentration in

"clean" nanocrystals was highly variable and seemingly independent of initial polymer quantity.

The Bi nanocrystals were used as seeds for the growth of Ge nanorods and CuInSe$_2$ nanowires. The particles were well capped and did not agglomerate during SLS growth, so wire size was controlled by varying initial Bi seed size. Consistent size control results for Ge nanorods were obtained by using "dirty" Bi; SLS growth was initiated in situ upon completion of the Bi reaction without cleaning the product first. No quantum confinement was observed on the Ge nanorods because the rods were not narrow enough. Smaller Bi seeds are needed to achieve this goal.

7.1.5 Unique Magnetic Properties of Au Nanoparticles

Small Au nanocrystals were investigated with regards to their size dependent magnetic properties. Dodecanethiol capped Au nanocrystals with diameters of 1.4 nm and 1.6 nm both showed paramagnetic characteristics at low temperatures, which is unexpected as bulk gold is diamagnetic. Both sets of Au nanocrystals only displayed paramagnetic behavior at temperatures < 10 K, confirmed by FC, ZFC, and field-dependent scans at 300 K and 5 K. These nanocrystals were tested with a variety of mass spectroscopy techniques to determine that no appreciable magnetic impurities were present. Contrary to previous studies, the Au displayed no ferromagnetism. The 1.6 nm Au nanocrystals had a maximum magnetic susceptibility or 0.08 μ_B/NC while the smaller 1.3 nm particles displayed 0.18 μ_B/NC – more than a two-fold increase. It is still undetermined whether this is a pure surface effect or due quantization of spin states.

7.2 FUTURE RESEARCH DIRECTIONS

7.2.1 Additional Application of a-Si:H Colloids

Currently, research on a-Si:H colloids is limited due to low throughput on the reaction. The batch reactor only holds 10 mL, and depending on the size of particles desired can yield as low as 1 mg per reaction with the maximum yield (of size controlled particles) at 30 mg per reaction. To get any appreciable product, the smallest particles possible are 240 nm. Theoretically, the process is fully scalable and a 100 mL batch reactor has been ordered. The larger reactor would allow larger batches in general, and would potentially allow access to particles smaller than 240 nm. Smaller particles could yield higher lithiation capacities due to higher surface accessibility.

Highly monodisperse a-Si:H particles can be coaxed to form superlattices. These superlattices have a large number of nanocavities that lead to a much largre refractive index than bulk Si. A huge magnetic and electric response in the NIR region results from the high refractive index value. This allows a bottom up approach for developing a 2D silicon colloidal crystal with strong magnetic response in the NIR, opening the door for developing new three dimensional metamaterials - fully artificial mixtures of materials, unlike any found in nature, composed of structured building blocks with strong magnetic resonance whose geometry size is much smaller than the light wavelength - through colloidal self assembly methods. The strong magnetic response of MMs allows fascinating new phenomena and applications, such as negative refraction,[1] perfect lenses[2] and even optical cloaking.[3] Figure 7.1 shows some preliminary results from a collaboration with Dr. Francisco Meseguer's group in Spain. The a-Si:H particles can be easily assembled and annealed to form large nanocavities with a high refractive index.

141
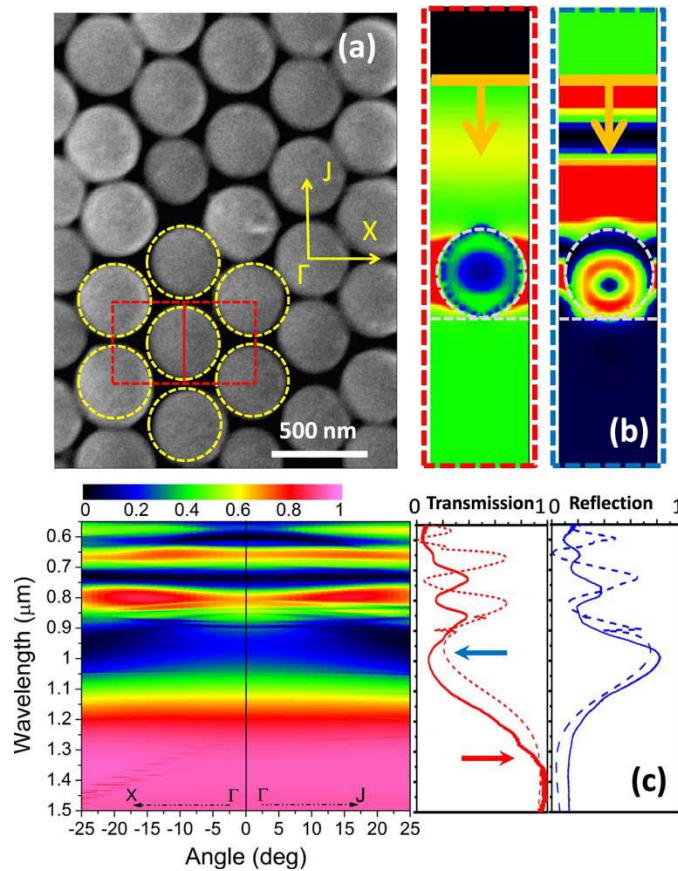
Figure 7.1: The SEM image and the optical properties of a 2D-SiPCS. a, SEM image of a 2D-SiPCS after 600 oC annealing. The yellow dash lines show the FDTD simulated structure being 380 nm the nanocavity diameter with a periodicity value of 430 nm. The red dash lines correspond to the simulated single cell, and the red solid line corresponds to the cut plane of the electric field map plot shown in Fig. 3b. b, Electric field distributions across the red solid line (shown in Fig. 3a) when the light is impinging on the sample from the top side. The field plots framed in red and blue dash lines correspond to the transmission peak and dip highlighted with red and blue arrows in Fig. 3c. The orange solid lines and arrows show the position of the light source in the simulation. c, Left panel: Transmittance map plot of a 2D-SiPCS as a function of the incident angle of the light and its wavelength value as obtained from the FDTD simulation. Middle and right panels: Transmission (middle panel) and reflection (right panel) spectra at Γ point (zero degrees case) obtained from both the experiment (colored solid lines) and the FDTD simulation (colored dash lines).

7.2.2 Improving Lithium Ion Batteries

7.2.2.1 Increasing Volumetric Capacity

Future research needs to focus on understanding cycling durability and the factors that limit performance, including the formation and stability of the solid-electrolyte interface (SEI) layer. Another issue that requires further consideration is the influence of the nanowire density on performance. Since the nanowire fabric has 90% void volume, the volumetric capacity of the nanowire fabric is relatively low. The specific capacity of 800 mA h/g corresponds to 186 mA h/cm^3, which is significantly lower than the volumetric capacity for graphite of 777–867 mA h/cm^3. However, the volumetric capacities of the nanowire fabric can be increased by densifying the films, with pressure for example. The maximum volumetric capacities of a densified Si nanowire fabric looks quite compelling with a maximum of 1864 mA h/cm^3—more than a factor of 2 higher than graphite. The influence of volumetric expansion and contraction upon lithiation and delithiation on cycling stability, however, will still need to be understood.

7.2.2.2 Growing Si and Ge Anodes Directly on Current Collectors

As previously discussed, one of the largest problems with Si and Ge anodes is pulverization and loss of contact with the current collector over repeated lithiation/delithiation cycles.[4,5] Conductive carbons, buffer materials, and polymeric binders have to be used to circumvent this problem and maintain cyclability.[6-8] Solving this problem is the primary goal. While one set of solutions lies with our nanowire paper anodes,[9] another could be found by chemically connecting the anode to the current collector. Chemical attachment is more robust than any physisorption and could potentially withstand the strains of repeated cycling. CVD methods have utilized this for years, though remain expensive and difficult to scale. Recently, there were reports of high

143

density Ge nanowires grown directly off of Cu foil suspended above a high boiling point solvent.[10] Though the wires grew in the vapor phase, it raised the possibility of doing the same in a supercritical system.

This theory was tested by running a standard SFLS Ge NW synthesis where the Au nanoparticle seeds were simply replaced by a sheet of Cu foil that would act as seed for growth. The foil substrate was first washed with a 1.0 M solution on nitric acid, thoroughly rinsed with DI water, ethanol, toluene, and chloroform. The preliminary results can be seen in Figure 7.2.
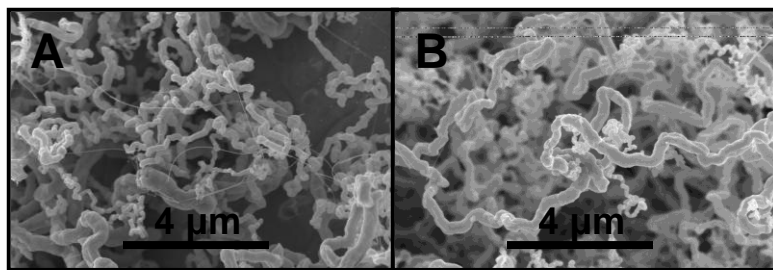
Figure 7.2:   SEM images of Ge NWs grown without Au seeds directly off of (A) thermally evaporated Au on Cu foil and (B) bare Cu foil

The syntheses were clearly successes. The wires grown off of Au coated Cu foil (A) were smaller in diameter, with a few pristine wires found on the substrate. The wires grown directly on Cu foil (B) were larger in diameter and highly kinked, but wires nonetheless. One drawback from the synthesis is difficulty with obtaining an accurate weight of nanowires after the reaction. Thus the following discharge capacity data, shown in Figure 7.3, must be taken with ±20% accuracy.
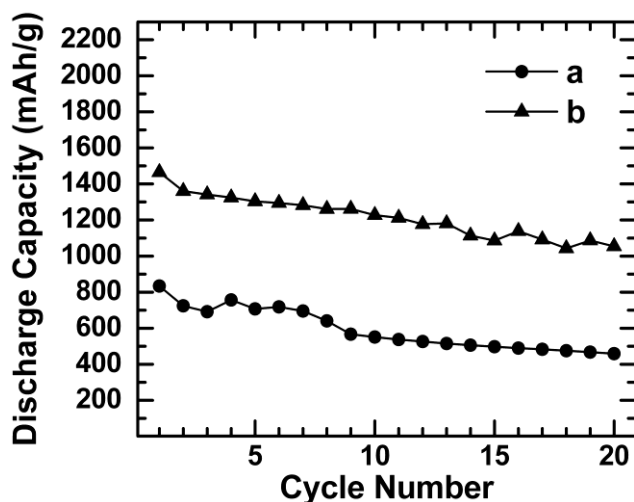
Figure 7.3: Plot of discharge capacity versus cycle number in a lithium ion battery cycling at C/20 for (a) Ge NW paper anode and (b) Ge NW grown directly off the Cu foil current collector.

By growing the Ge NWs directly off the Cu foil, a capacity of 1400 mA h/g was obtained in the second cycle with 83% cycle retention after 20 cycles. Though cycle retention can be improved, the capacity was near the theoretical maximum for Ge of 1624 mA h/g without utilizing any binder or conductive additive and the project should be pursued. While CVD methods may achieve better wires, this method is potentially scalable and relatively cheap.

A few attempts have been made to translate this to a Si NW system, as yet to no avail. A plethora of metals could be tried as potential current collectors, including but not limited to Sn, Ni, Cu, and Au. Full characterization of the nanowire foils needs to be conducted, including XRD, Raman spectroscopy, and SEM of the wire systems. After cycling the batteries should be reexamined by all techniques to observe any pulverization or lack thereof. A more consistent method for obtaining sample weights is also required to obtain consistent, reliable results.

145

7.2.2.3 Synthesis of Lithium Sulfide Nanowires

While this dissertation focused on anode materials, cathodes in lithium ion batteries are actually further behind. $LiCoO_2$, the current standard for commercial LIB anodes, has a working capacity below 200 mA h/g. Much work is focused on improving various lithium containing metal oxides, but there are many other materials with high capacity potentials that do not have a natural Li source, such as sulfur. Sulfur has a lithiation capacity of 1673 mA h/g and a moderate working potential (2.2 V vs. Li/Li^+), making it a good cathode candidate.[14] Unfortunately, it must be pre-lithiated or an anode with a Li source must be coupled with it. Another option is the synthesis of Li_xSi_{1-x} or Li_xGe_{1-x} nanowires. A lithium ion source could be added to the SFLS reactant mixture to modify the growth process and potentially grown Li-(Si,Ge) alloyed nanowires.

7.2.3 Studying Au and Bi Nanomagnetism at the Atomic Level

Due to their small size, in the past the magnetic characteristics have been calculated by measuring large ensembles of nanoparticles.[11] This technique is not sufficient when attempting to determine the reason behind the magnetic properties, as it is only an average over a wide range of nanoparticle sizes and compositions. Through the combination of first principle calculations and SP-STM, the local magnetization of individual nanoparticles can be probed and a model derived, providing important insight to the basic physics behind these transitions.

Preliminary research has already been conducted on Au and Bi nanocrystals. Nanocrystals of various sizes and with different capping ligands have been synthesized and tested for their magnetic properties with a SQUID magnetometer, but this only reveals ensemble characteristics. Preliminary results indicate that with small enough nanocrystals, the naturally diamagnetic materials give way to paramagnetism. Other researchers have observed this as well, but the mechanism is highly debated. SP-STM

can be used to characterize the magnetic properties of single nanocrystals. SP-STM allows probing for polarized spins within individual nanoparticles. This will show whether the unpaired spins are localized surface states or located throughout. Likewise, it will allow mapping of the LDOS at the core and surfaces of the nanoparticles, including ligand contributions. This data can be coupled with models to determine the theoretical magnetization and electronic band structure of individual particles. By utilizing density functional theory (DFT) in conjunction with the multiple-scattering Korringa-Kohn-Rostoker (KKR) Green's function method[12] the local density of states (LDOS) can be calculated with spatial resolution.[13] The local spin density approximation (LSDA) can alsobe used in modeling the local energy levels.

7.3 REFERENCES

(1) Shelby R. A.;Smith D. R.; Schultz S. *Science* **292**, 77-79 (2001).

(2) Zhang X.; Liu Z. *Nat. Mater.* **7**, 435-441 (2008).

(3) Schurig D.; Mock J. J.; Justice B. J.; Cummer S. A.; Pendry J. B.; Starr A. F.; Smith D. R. *Science* **314**, 977-980 (2006).

(4) Boukamp, B. A.; Lesh, G. C.; Huggins, R. A. *Journal of the Electrochemical Society* **1981**, *128*, 725.

(5) Xu, Y. H.; Yin, G. P.; Zuo, P. J. *Electrochim. Acta* **2008**, *54*, 341.

(6) Lee, J. K.; Smith, K. B.; Hayner, C. M.; Kung, H. H. *Chem. Commun.* **2010**, *46*, 2025.

(7) Lee, J.-K.; Kung, M. C.; Trahey, L.; Missaghi, M. N.; Kung, H. H. *Chem. Mat.* **2009**, *21*, 6.

(8) DiLeo, R. A.; Frisco, S.; Ganter, M. J.; Rogers, R. E.; Raffaelle, R. P.; Landi, B. J. *Journal of Physical Chemistry C* **2011**, *115*, 22609.

(9) Chockla, A. M.; Harris, J. T.; Akhavan, V. A.; Bogart, T. D.; Holmberg, V. C.; Steinhagen, C.; Mullins, C. B.; Stevenson, K. J.; Korgel, B. A. *J. Am. Chem. Soc.* **2011**, *133*, 20914.

(10) Geaney, H.; Dickinson, C.; Barrett, C. A.; Ryan, K. M. *Chem. Mat.* **2011**, *23*, 4838.

(11) Bode,M;. *Rep. Prog. Phys.* **2003**, *66*, 523.

147

(12)   Wildberger, K. *et. al.*, *Phys. Rev. Lett.* **1995**, *75*, 509.

(13)   H. Oka *et. al.*, *Science* **2010**, *327*, 843.

(14)   Zheng, G.; Yang, Y.; Cha, J. J.; Hong, S. S.; Cui, Y. *Nano Lett.* **2011,** *11,* 4462-4467.

Bibliography

Alcantara, R.; Lavela, P.; Tirado, J. L.; Stoyanova, R.; Zhecheva, E. *Journal of Solid State Chemistry* **1997**, *134*, 265.

Armand, M.; Tarascon, J. M. *Nature* **2008**, *451*, 652.

Ashby, M.F.; Schodek, D.L.; Ferreira, P.J.S.G. *Nanomaterials, Nanotechnologies, and Design*. Butterworth-Heinemann: 2009.

Ayuela, A.; Crespo, P.; Garcia, M.A.; Hernando, A.; Echenique, P.M. *New Journal of Physics*. **2012**, *14*, 013064.

Baggetto, L.; Hensen, E. J. M.; Notten, P. H. L. *Electrochim. Acta* **2010**, *55*, 7074.

Baggetto, L.; Notten, P. H. L. *Journal of the Electrochemical Society* **2009**, *156*, A169.

Baranchugov, V.; Markevich, E.; Salitra, G.; Aurbach, D.; Semrau, G.; Schmidt, M. A. *J Electrochem Soc* **2008**, *155* (3), A217-A227

Basu, S.; Zeller, C.; Flanders, P. J.; Fuerst, C. D.; Johnson, W. D.; Fischer, J. E. *Materials Science and Engineering* **1979**, *38*, 275.

Beuvier, T.; Richard-Plouet, M.; Mancini-Le Granvalet, M.; Brousse, T.; Crosnier, O.; Brohan, L. *Inorg Chem* **2010,** *49* (18), 8457-8464.

Besenhard, J. O.; Eichinger, G. *Journal of Electroanalytical Chemistry* **1976**, *68*, 1.

Billas, I.M.L. ; Becker, J.A. ; Chatelain, A. ; Deheer, W.A. *Phys. Rev. Lett.* **1993**, *71,* 4067-4070.

Bley, R. A.; Kauzlarich, S. M. *J. Am. Chem. Soc.* **1996**, *118*, 12461-12462.

Bode, M. *Rep. Prog. Phys.* **2003**, *66*, 523

Borodko, Y.; Habas, S. E.; Koebel, M.; Yang, P.; Frei, H.; Somorjai, G. A. *The Journal of Physical Chemistry B* **2006,** *110* (46), 23052-23059.

Boukamp, B. A.; Lesh, G. C.; Huggins, R. A. *J Electrochem Soc* **1981,** *128* (4), 725-729.

Bradley, J. S.; Hill, E. W.; Chaudret, B.; Duteil, A. *Langmuir* **1995,** *11* (3), 693-695.

Brenner, S.S. *Acta Metal*. **1956**, *4*, 62-63.

Bridel, J. S.; Azais, T.; Morcrette, M.; Tarascon, J. M.; Larcher, D. *Chem Mater* **2010,** *22* (3), 1229-1241;

Brust, M.; Walker, M.; Bethell, D.; Schiffrin, D.J.; Whyman, R. *J. of the Amer. Chem. Soc. – Chem. Comm.* **1994**, *7*, 801-802.

Campbell, I. H.; Fauchet, P. M. *Solid State Commun.* **1986**, *58*, 739-741.

Canaria, C. A.; Huang, M.; Cho, Y.; Heinrich, J. L.; Lee, L. I.; Shane, M. J.; Smith, R. C.; Sailor, M. J.; Miskelly, G. M. *Adv. Funct. Mater.* **2002**, *12*, 495-500.

Carlson, D. E.; Wronski, C. R. *Appl. Phys. Lett.* **1976**, *28*, 671-673.

Chan, C.K.; Patel, R.N.; O'Connell, M.J.; Korgel, B.A.; Cui, Y. *ACS Nano* **2010**, *4*, 1443-1450.

Chan, C. K.; Peng, H.; Liu, G.; McIlwrath, K.; Zhang, X. F.; Huggins, R. A.; Cui, Y. *Nat Nano* **2008**, *3*, 31.

Chan, C. K.; Ruffo, R.; Hong, S. S.; Huggins, R. A.; Cui, Y. *J. Power Sources* **2009**, *189*, 34.

Chang, C. C.; Scarr, N.; Kumta, P. N. *Solid State Ion.* **1998**, *112*, 329.

Chockla, A.M. *University of Texas at Austin Dissertations*, 2012

Chockla, A.M.; Harris, J.T.; Korgel, B.A. *Chem Mater.*, **2010**, *23*, 1964-1970.

Chockla, A. M.; Harris, J. T.; Akhavan, V. A.; Bogart, T. D.; Holmberg, V. C.; Steinhagen, C.; Mullins, C. B.; Stevenson, K. J.; Korgel, B. A. *J. Am. Chem. Soc.* **2011**, *133*, 20914.

Chockla, A.M; Korgel, B.A. *J. Mater. Chem.* **2009**, *19*, 996.

Choi, H. S., Park, C. R. *InTech*, **2010,** ISBN 978-953-307-058-2 Available from: http://www.intechopen.com/articles/show/title/towards-high-performance-anodes-with-fast-charge-discharge-rate-for-lib-based-electrical-vehicles

Choi, J. W.; Hu, L.; Cui, L.; McDonough, J. R.; Cui, Y., *J. Power Sources* **2010***, 195*, 8311.

Chu, H.T.; Zhang, W.J. *J. Phys. Chem. Solids* **1992**, *53*, 1059-1065.

Cody, G. D.; Tiedje, T.; Abeles, B.; Brooks, B.; Goldstein, Y. *Phys. Rev. Lett.* **1981**, *47*, 1480-1483.

Collier, C.P.; Vossmeyer, T.; Heath, J.R. *Annual Rev. of Phys. Chem.* **1998**, *49*, 371-404.

Cowley, A. H. In Inorganic Syntheses; John Wiley & Sons: New York, NY, 1997; p 100.

Crespo, P. ; Garcia, M.A. ; Pinel, E.F. ; Multigner, M. ; Alcantara, D. ; de la Fuente, J.M. ; Penades, S. ; Hernando, A. *Phys. Rev. Lett.* **2006**, *97*, 177203.

Crespo, P. ; Litran, R. ; Rojas, T.C. ; Multigner, M. ; de la Fuente, J.M. ; Sanchez-Lopez, J.C. ; Garcia, M.A. ; Hernando, A. ; Penades, S. ; Fernandez, A. Phys. *Rev. Lett.* **2004**, *93*, 087204.

Cui, L.-F.; Hu, L.; Wu, H.; Choi, J. W.; Cui, Y. *Journal of the Electrochemical Society* **2011**, *158*, A592.

Cui, L. F.; Ruffo, R.; Chan, C. K.; Peng, H. L.; Cui, Y. *Nano Letters* **2009**, *9*, 491.

Cui, L.-F.; Yang, Y.; Hsu, C.-M.; Cui, Y. *Nano Letters* **2009**, *9*, 3370.

Cui, Y.; Lieber, C.M. *Science* **2001**, *291*, 851-853.

Dahn, J. R.; Zheng, T.; Liu, Y. H.; Xue, J. S. *Science* **1995**, *270*, 590.

Daniel, M.C. ; Astruc, D. *Chemical Reviews*. **2004**, *104*, 293-346.

de Heer, W. A.; Bacsa, W. S.; Châtelain, A.; Gerfin, T.; Humphrey-Baker, R.; Forro, L.; Ugarte, D. *Science* **1995**, *268*, 845.

DiLeo, R. A.; Frisco, S.; Ganter, M. J.; Rogers, R. E.; Raffaelle, R. P.; Landi, B. J. *Journal of Physical Chemistry C* **2011**, *115*, 22609.

Dimov, N.; Kugino, S.; Yoshio, M. *Electrochim Acta* **2003,** *48* (11), 1579-1587.

Dong, A.; Wang, F.; Daulton, T.L.; Buhro, W.E. *Nano Letters* **2007**, *7*, 1308-1313.

Duan, X.; Huang, Y.; Agarwal, M.; Lieber, C.M. *Nature* **2003**, *421*, 241-245.

Duan, X.; Huang, Y.; Lieber, C.M. *Nano Lett*. **2002**, *2*, 487-490.

Dulaurent, O.; Courtois, X.; Perrichon, V.; Bianchi, D. *The Journal of Physical Chemistry B* **2000,** *104* (25), 6001-6011;

Eichinger, G.; Besenhard, J. O. *Journal of Electroanalytical Chemistry* **1976**, *72*, 1.

El-Sayed, M.A. *Acc. Chem. Res.* **2001**, *34,* 257-264.

Endo, M.; Muramatsu, H.; Hayashi, T.; Kim, Y. A.; Terrones, M.; Dresselhaus, M. S. *Nature* **2005**, *433*, 476.

Erker, L. *Treatise on Ores and Assaying*; 2nd ed.; University of Chicago, 1951.

Fanfair, D.D.; Korgel, B.A. *Chem. Mater.* **2007**, *19*, 4943-4948.

Fanfair, D.D.; Korgel, B.A. *Crystal Growth and Design* **2005**, *5*, 1971-1976.

Farjas, J.; Das, D.; Fort, J.; Roura, P.; Bertran, E. *Phys. Rev. B* **2002**, *65*, 115403

Ferrari, A. C. *Solid State Commun.* **2007**, *143*, 47.

Ferrari, A. C.; Robertson, J. *Phys. Rev. B* **2000**, *61*, 14095.

Fievet, F.; Fievetvincent, F.; Lagier, J. P.; Dumont, B.; Figlarz, M. *J Mater Chem* **1993,** *3* (6), 627-632

Fichtner, M. *Adv. Eng. Mater.* **2005**, *7*, 443-455.

Foos, E.E.; Stroud, R.M.; Berry, A.D.; Snow, A.W.; Armistead, J.P. *J. Am. Chem. Soc.* **2000**, *122*, 7114-7115.

Franks, J. *Nature* **1956**, *177*, 984.

Freknel, J.; Dorfman, J., *Nature* **1930**, *126*, 274.

Friedrichs, O.; Aguey-Zinsou, F.; Fernandez, J. R. A.; Sanchez-Lopez, J. C.; Justo, A.; Klassen, T.; Bormann, R.; Fernandez, A. *Acta Materialia* **2006**, *54*, 105-110.

Fukutani, K.; Kanbe, M.; Futako, W.; Kaplan, B.; Kamiya, T.; Fortmann, C. M.; Shimizu, I. *J. Non-Cryst. Solids* **1998**, *227*, 63-67.

Fuller, C. S.; Severiens, J. C. *Phys. Rev.* **1954,** *96,* 21-24.

Gaisler, S. V.; Semenova, O. I.; Sharafutdinov, R. G.; Kolesov, B. A. *Phys Solid State+* **2004,** *46* (8), 1528-1532.

Gajovic, A.; Gracin, D.; Juraic, K.; Sancho-Parramon, J.; Ceh, M. *Thin Solid Films* **2009**, *517*, 5453-5458.

Galeener, F. L.; Mikkelsen Jr, J. C. *Solid State Commun.* **1981**, *37*, 719.

Garitaonandia, J.S.; Insausti, M.; Goikolea, E.; Suzuki, M.; Cashion, J.D.; Kawamura, N.; Ohsawa, H.; de Muro, I.G.; Suzuki, K.; Plazaola, F.; Rojo, T. *Nano Letters.* **2008**, *8*, 661-667.

Gao, B.; Sinha, S.; Fleming, L.; Zhou, O. *Advanced Materials* **2001**, *13*, 816.

Gao, J. H.; Gu, H. W.; Xu, B., *Accounts of Chemical Research* **2009**, *42*, 1097.

Gittleman, J. I.; Abeles, B.; Bozowski, S. *Phys. Rev. B.* **1974**, *9*, 3891-3897.

Gonsalves, A. *Intel 32 nm Processor Headed for Production* http://www.informationweek.com/news/hardware/processors/showArticle.jhtml?articleID=224400257&subSection=All+Stories (May 11, 2010)

Gonzalez, C. ; Simon-Manso, Y. ; Marquez, M. ; Mujica, V. *J. of Phys. Chem. B*. **2006**, *110*, 687-691.

Graetz, J.; Ahn, C. C.; Yazami, R.; Fultz, B. *Electrochemical and Solid State Letters* **2003**, *6*, A194.

Graetz, J.; Ahn, C. C.; Yazami, R.; Fultz, B. *Journal of the Electrochemical Society* **2004**, *151*, A698.

Gudiksen, M.S.; Lieber, C.M. *J. Am. Chem. Soc.* **2000**, *122*, 8801-8802.

Guha, S.; Yang, J.; Williamson, D. L.; Lubianiker, Y.; Cohen, J. D.; Mahan, A. H. *Appl. Phys. Lett.* **1999**, *74*, 1860-1862.

Harris, J. T.; Hueso, J. L.; Korgel, B. A. *Chem. Mat.* **2010**, *22*, 6378.

Han, G. B.; Lee, J. N.; Choi, J. W.; Park, J. K. *Electrochim. Acta* **2011**, *56*, 8997.

Han, J. T.; Liu, D. Q.; Song, S. H.; Kim, Y.; Goodenough, J. B. *Chem. Mat.* **2009**, *21*, 4753.

Hanrath, T.; Korgel, B.A. *Adv. Mater*. **2003**, *15*, 437.

Hanrath, T.; Korgel, B.A. *J. Am. Chem. Soc*. **2002**, *124*, 1424.

Hardwick, L. J.; Ruch, P. W.; Hahn, M.; Scheifele, W.; Kötz, R.; Novák, P. *J Phys Chem Solids 69* (5-6), 1232-1237.

Harris, J. T.; Hueso, J. L.; Korgel, B. A. *Chem Mater* **2010,** *22* (23), 6378-6383

Hatchard, T. D.; Dahn, J. R. *Journal of the Electrochemical Society* **2004**, *151*, A838.

Heitsch, A. T.; Akhavan, V. A.; Korgel, B. A. *Chem. Mat.* **2011**, *23*, 2697.

Heitsch, A. T.; Fanfair, D. D.; Tuan, H. Y.; Korgel, B. A. *J. Am. Chem. Soc.* **2008**, *130*, 5436.

Heitsch, A. T.; Hessel, C. M.; Akhavan, V. A.; Korgel, B. A. *Nano Letters* **2009**, *9*, 3042.

Heremans, J.; Thrush, C.M.; Lin, Y.M.; Chroin, S.; Zhang, Z.; Dresselhaus, M.S.; Mansfield, J.F. *Phys. Rev. B* **2000**, *61*, 2921-2930

Holmberg, V. C.; Patel, R. N.; Korgel, B. A. *J. Mater. Res.* **2011**, *26*, 2305.

Holmes, J. D.; Johnston, K. P.; Doty, R. C.; Korgel, B. A. *Science* **2000**, *287*, 1471.

Holzapfel, M.; Buqa, H.; Scheifele, W.; Novak, P.; Petrat, F. M. *Chem. Commun.* **2005**, 1566-1568.

Hori, H.; Teranishi, T.; Nakae, Y.; Seino, Y.; Miyake, M.; Yamada, S. *Phys. Lett. A.* **1999***, 263,* 4-6.

Hori, H. ; Yamamoto, Y. ; Iwamoto, T. ; Miura, T. ; Teranishi, T. ; Miyake, M. *Phys. Rev. B.* **2004**, *69*, 174411.

Hu, L. B.; Wu, H.; La Mantia, F.; Yang, Y. A.; Cui, Y. *ACS Nano* **2010**, *4*, 5843.

Hu, Y.-S.; Adelhelm, P.; Smarsly, B. M.; Maier, J. *Chemsuschem* **2010**, *3*, 231.

Huang, R.; Fan, X.; Shen, W.; Zhu, J. *App. Phys. Lett.* **2009**, *95*, 133119.

Huang, R.; Zhu, J. *Materials Chemistry and Physics* **2010**, *121*, 519.

Huang, Y.; Duan, X.; Cui, Y.; Lauhon, L.J.; Kim, K.H.; Lieber, C.M. *Science*, **2001**, *294*, 1313-1317

Hwang, C. M.; Park, J. W. *Thin Solid Films* **2010**, *518*, 6590.

Jezequel, G.; Thomas, J. *Phys. Rev. B* **1997**, *56*, 6620.

Johnson, D. C.; Mosby, J. M.; Riha, S. C.; Prieto, A. L. *Journal of Materials Chemistry* **2010**, *20*, 1993.

Johnson, E.R.; Amick, J.A. *J. Appl. Phys*. **1954**, *25*, 1204-1208.

Jose-Yacaman, M.; Rendon, L.; Arenas, J.; Serra Puche, M.C. *Science* **1996**, *273*, 223-225.

Kasavajjula, U.; Wang, C. S.; Appleby, A. J. *J. Power Sources* **2007**, *163*, 1003-1039.

Kim, J. B.; Lee, H. Y.; Lee, K. S.; Lim, S. H.; Lee, S. M. *Electrochem Commun* **2003,** *5* (7), 544-548.

Kim, J. W.; Ryu, J. H.; Lee, K. T.; Oh, S. M. *J Power Sources* **2005,** *147* (1-2), 227-233

Korgel, B.A.; Monbouquette, H.G. *J. Phys. Chem.* **1996**, *100*, 346-351.

Krishnan, R.; Lu, T.-M.; Koratkar, N. *Nano Lett.* **2011,** *11*, 377-384.

Kruangam, D.; Toyama, T.; Hattori, Y.; Deguchi, M.; Okamoto, H.; Hamakawa, Y. *J. Non-Cryst. Solids* **1987**, *97-8*, 293-296.

Laforge, B.; Levan-Jodin, L.; Salot, R.; Billard, A. *Journal of the Electrochemical Society* **2008**, *155*, A181.

Lecomber, P. G.; Owen, A. E.; Spear, W. E.; Hajto, J.; Snell, A. J.; Choi, W. K.; Rose, M. J.; Reynolds, S. *J. Non-Cryst. Solids* **1985**, *77-8*, 1373-1382.

Lee, D. C.; Smith, D. K.; Heitsch, A. T.; Korgel, B. A., *Annual Reports on the Progress of Chemistry, Section C: Physical Chemistry* **2007**, *103*, 351.

Lee, J.-K.; Kung, M. C.; Trahey, L.; Missaghi, M. N.; Kung, H. H. *Chem. Mat.* **2009**, *21*, 6.

Lee, J. K.; Smith, K. B.; Hayner, C. M.; Kung, H. H. *Chem. Commun.* **2010**, *46*, 2025.

Lee, S.; Ham, J.; Jeon, K.; Noh, J.S. Lee, W. *Nanotechnology* **2010**, *21*, 405701-405706.

Lee, Y. M.; Lee, J. Y.; Shim, H.-T.; Lee, J. K.; Park, J.-K. *J Electrochem Soc* **2007,** *154* (6), A515-A519.

Lespade, P.; Al-Jishi, R.; Dresselhaus, M. S. *Carbon* **1982**, *20*, 427.

Li, H.; Huang, X. J.; Chen, L. Q.; Wu, Z. G.; Liang, Y. *Electrochem. Solid State Lett.* **1999**, *2*, 547-549.

Li, H.; Huang, X. J.; Chen, L. Q.; Zhou, G. W.; Zhang, Z.; Yu, D. P.; Mo, Y. J.; Pei, N. *Solid State Ion.* **2000**, *135*, 181.

Li, J.; Dahn, J. R. *Journal of the Electrochemical Society* **2007**, *154*, A156.

Limthongkul, P.; Jang, Y. I.; Dudney, N. J.; Chiang, Y. M. *Acta Materialia* **2003**, *51*, 1103.

Lin, Y.M.; Sun, X.; Dresselhaus, M.S. *Phys Rev. B* **2000**, *62*, 4610-4623.

Liu, K.; Chien, C.L. *Phys. Rev. B* **1998**, *58*, 681-684.

Liu, G. Q.; Zeng, C. L.; Yang, K. *Electrochim. Acta* **2002**, *47*, 3239.

Lucovsky, G.; Nemanich, R. J.; Knights, J. C. *Phys. Rev. B* **1979**, *19*, 2064-2073.

Magasinski, A.; Dixon, P.; Hertzberg, B.; Kvit, A.; Ayala, J.; Yushin, G. *Nat Mater* **2010,** *9* (4), 353-358.

Mahan, A. H.; Yang, J.; Guha, S.; Williamson, D. L. *Phys. Rev. B* **2000**, *61*, 1677-1680.

Mamiya, M.; Takei, H.; Kikuchi, M.; Uyeda, C. *J. Cryst. Growth* **2001**, *229*, 457-461.

Maranchi, J. P.; Kumta, P. N.; Hepp, A. F. In *Developments in Solid Oxide Fuel Cells and Lithium Ion Batteries*; Manithiram, A., Kumta, P. N., Sundaram, S. K., Chan, S. W., Eds. 2005; Vol. 161, p 121.

Mauron, P.; Buchter, F.; Friedrichs, O.; Remhof, A.; Bielmann, M.; Zwicky, C. N.; Zuttel, A. *J. Phys. Chem. B* **2008**, *112*, 906-910.

McAlpine, M.C.; Ahmad, H.; Wang, D.; Heath, J.R. *Nat. Mater*. **2007**, *6*, 379-384.

Mizushima, K.; Jones, P. C.; Wiseman, P. J.; Goodenough, J. B. *Materials Research Bulletin* **1980**, *15*, 783.

Mizushima, K.; Jones, P. C.; Wiseman, P. J.; Goodenough, J. B. *Solid State Ion.* **1981**, *3-4*, 171.

Mohri, M.; Yanagisawa, N.; Tajima, Y.; Tanaka, H.; Mitate, T.; Nakajima, S.; Yoshida, M.; Yoshimoto, Y.; Suzuki, T.; Wada, H. *J. Power Sources* **1989**, *26*, 545.

Monika, W.;Wang, Y. ; Zerda, T. W*J. Phys. Condens. Matter* **2005**, *17*, 2387.

Murphy, D. W.; Carides, J. N. *Journal of the Electrochemical Society* **1979**, *126*, 349.

Murphy, D. W.; Christian, P. A.; Disalvo, F. J.; Carides, J. N. *Journal of the Electrochemical Society* **1979**, *126*, 497.

Murray, C.B.; Kagan, C.R.; Bawendi, M.G. *Annual Review of Materials Science* **2000**, *30*, Future.

Murugesan, S.; Harris, J.T.; Korgel, B.A.; Stevenson, K.P. *Chem. Mater.* **2012**, *24*, 1306-1315.

Nanda, J.; Datta, M. K.; Remillard, J. T.; O'Neill, A.; Kumta, P. N. *Electrochem Commun* **2009,** *11* (1), 235-237.

Nealon, G.L.; Donnio, B.; Greget, R.; Kappler, J.P.; Terazzi, E.; Gallani, J.L. *Nanoscale.* **2012**, *4*, 5244-5258.

Neiner, D.; Kauzlarich, S. M. *Chem. Mat.* **2010**, *22*, 487-493.

Ng, S. H.; Wang, J.; Guo, Z. P.; Chen, J.; Wang, G. X.; Liu, H. K. *Electrochim. Acta* **2005**, *51*, 23.

Nunomora, N.; Hori, H.; Teranishi, T.; Miyake, M.; Yamada, S. **1998**, *249*, 5-6.

Obrovac, M. N.; Christensen, L., *Electrochem. Solid-State Lett.* **2004**, *7*, A93.

Odden, J. O.; Egeberg, P. K.; Kjekshus, A. *Sol. Energ. Mat. Sol. C.* **2005**, *86*, 165-176.

Ohzuku, T.; Kitagawa, M.; Hirai, T. *Journal of the Electrochemical Society* **1990**, *137*, 769.

Onischuk, A. A.; Strunin, V. P.; Samoilova, R. I.; Nosov, A. V.; Ushakova, M. A.; Panfilov, V. N. *J. Aerosol Sci.* **1997**, *28*, 1425-1441.

Onischuk, A. A.; Strunin, V. P.; Ushakova, M. A.; Panfilov, V. N. *Khimicheskaya Fizika* **1994**, *13*, 129-138.

Oumellal, Y.; Delpuech, N.; Mazouzi, D.; Dupre, N.; Gaubicher, J.; Moreau, P.; Soudan, P.; Lestriez, B.; Guyomard, D. *J Mater Chem* **2011,** *21* (17), 6201-6208.

Owen, A. E.; Lecomber, P. G.; Spear, W. E.; Hajto, J. *J. Non-Cryst. Solids* **1983**, *59-6*, 1273-1280.

Ozin, G.A.; Arsenault, A.C. *Nanochemistry: A Chemical Approach to Nanomaterials*; RSC Publishing, 2005

Padhi, A. K.; Nanjundaswamy, K. S.; Goodenough, J. B. *Journal of the Electrochemical Society* **1997**, *144*, 1188.

Park, B. K.; Jeong, S.; Kim, D.; Moon, J.; Lim, S.; Kim, J. S. *J Colloid Interf Sci* **2007,** *311* (2), 417-424; (b) Anzlovar, A.; Orel, Z. C.; Zigon, M. *J Nanosci Nanotechno* **2008,** *8* (7), 3516-3525

Park, M.-H.; Cho, Y.; Kim, K.; Kim, J.; Liu, M.; Cho, J. *Angew. Chem. Int. Ed.* **2011,** *50,* 9647-9650.

Park, M. H.; Kim, M. G.; Joo, J.; Kim, K.; Kim, J.; Ahn, S.; Cui, Y.; Cho, J. *Nano Lett* **2009,** *9* (11), 3844-3847.

Pell, L. E.; Schricker, A. D.; Mikulec, F. V.; Korgel, B. A. *Langmuir* **2004**, *20*, 6546.

Peng, Z.A.; Peng, X.G. *J. of the Am. Chem. Soc.* **2002**, *124*, 3343-3353.

Peng, Z.A.; Xi, P. *J of the Am. Chem. Soc.* **2001**, *123*, 1389-1395.

Pollak, E.; Salitra, G.; Baranchugov, V.; Aurbach, D. *The Journal of Physical Chemistry C* **2007,** *111* (30), 11437-11444.

Puntes, V.; Krishnan, K.M.; Alivisatos, A.P. *Science* **2001**, *291*, 2115-2117.

Qi, J.; Shi, D.; Jiang, X. *Chem. Phys. Lett.* **2008**, 4*60*, 266-271.

Rabideau, B. D.; Pell, L. E.; Bonnecaze, R. T.; Korgel, B. A. *Langmuir* **2007**, *23*, 1270.

Richter, H.; Wang, Z. P.; Ley, L. *Solid State Commun.* **1981**, *39*, 625-629.

Rong, J. P.; Masarapu, C.; Ni, J.; Zhang, Z. J.; Wei, B. Q. *ACS Nano* **2010**, *4*, 4683.

Roura, P.; Farjas, J.; Rath, C.; Serra-Miralles, J.; Bertran, E.; Cabarrocas, P. R. I. *Phys. Rev. B* **2006**, *73*, 085203.

Saunders, A. E.; Sigman, M. B.; Korgel, B. A. *J. Phys. Chem. B* **2004**, *108*, 193.

Sears, G.W. *Acta Metal.* **1955**, *3*, 361-365

Sethuraman, V. A.; Kowolik, K.; Srinivasan, V. *J. Power Sources* **2011**, *196*, 393.

Shah, P.S.; Husain, S.; Johnston, K.P.; Korgel, B.A. *J. of Phys. Chem. B* **2001**, *105*, 9433.

Smith, D. A.; Holmberg, V. C.; Korgel, B. A. *ACS Nano* **2010**, *4*, 2356.

Snell, A. J.; Mackenzie, K. D.; Spear, W. E.; Lecomber, P. G.; Hughes, A. J. *Appl. Phys.* **1981**, *24*, 357-362.

Sokolov, A. P.; Shebanin, A. P.; Golikova, O. A.; Mezdrogina, M. M. *J. Phys.-Condes. Matter* **1991**, *3*, 9887-9894.

Son, S. U.; Park, I. K.; Park, J.; Hyeon, T. *Chemical Communications* **2004,** (7), 778-779.

Song, H.; Rioux, R. M.; Hoefelmeyer, J. D.; Komor, R.; Niesz, K.; Grass, M.; Yang, P.; Somorjai, G. A. *J Am Chem Soc* **2006,** *128* (9), 3027-3037

Song, T.; Xia, J. L.; Lee, J. H.; Lee, D. H.; Kwon, M. S.; Choi, J. M.; Wu, J.; Doo, S. K.; Chang, H.; Il Park, W.; Zang, D. S.; Kim, H.; Huang, Y. G.; Hwang, K. C.; Rogers, J. A.; Paik, U. *Nano Lett* **2010,** *10* (5), 1710-1716.

Span, R.; Springer: Berlin, 2000, p 367.

Spinella, C.; Lombardo, S.; Priolo, F. *J. App. Phys.* **1998**, *84*, 5383-5414.

Steinhagen, C.; Akhavan, V.A.; Goodfellow, B.W.; Panthani, M.G.; Harris, J.T.; Holmberg, V.C.; Korgel, B.A. *ACS Appl. Mater. Interfaces* **2011**, *3*, 1781-1785.

Sun, S.; Fullerton, E.E.; Weller, D.; Folks, L.; Moser, A. *Science* **2000**, *287*, 1989-1992.

Sun, S.H.; Murray, C.B. *J. Appl. Phys.* **1999**, *85*, 4325-4330.

Tarascon, J. M.; Armand, M. *Nature* **2001,** *414* (6861), 359-367

Teh, L. K.; Choi, W. K.; Bera, L. K.; Chim, W. K. *Solid-State Electronics* **2001**, *45*, 1963.

Tian, B.; Zheng, X.; Kempa, T.J.; Fang, Y.; Yu, N.; Yu, G.; Huang, J.; Lieber, C.M. *Nature* **2007,** *449*, 885-889

Timmons; A; Todd; A. D, W.; Mead; S, D.; Carey; Graham, H.; Sanderson; R, J.; Mar; R, E.; Dahn; J, R. *Electrochem. Soc.* **2007,** *154.*

Tsu, D. V. ; Chao, B. S. ; Jones, S. J. *Sol. Energ. Mat. Sol. C.* **2003**, *78*, 115-141.

Tuan, H.-Y.; Korgel, B. A. *Chem. Mat.* **2008**, *20*, 1239.

Tuinstra, F.; Koenig, J. L. *J. Chem. Phys.* **1970**, *53*, 1126.

Vandewalle, C. G.; Street, R. A. *Phys. Rev. B* **1995**, *51*, 10615-10618.

Viera, G.; Huet, S.; Boufendi, L. *J. Appl. Phys.* **2001**, *90*, 4175-4183.

Volokitin, Y.; Sinzig, J.; deJongh, L.J.; Schmid, G.; Vargaftik, M.N.; Moiseev, I.I. *Nature.* **1996,** *384*, 621-623.

Wagner, R.S.; Ellis, W.C. *Appl. Phys. Lett.* **1964**, *4*, 89-90.

Wakihara, M. *Materials Science & Engineering R-Reports* **2001**, *33*, 109.

Wang, F.; Buhro, W.E. *J. Am. Chem. Soc.* **2007**, *129,* 14381-14387.

Wang, F.; Tang, R.; Yu, H.; Gibbons, P.C.; Buhro, W.E. *Chem. Mater.* **2008**, *20*, 3656-3662.

Wang, J.-Z.; Zhong, C.; Chou, S.-L.; Liu, H.-K. *Electrochem. Commun.* **2010,** *12*, 1467.

Wang, W.; Datta, M. K.; Kumta, P. N. *Journal of Materials Chemistry* **2007**, *17*, 3229.

Wang, W.; Kumta, P. N. *ACS Nano* **2010**, *4*, 2233.

Wang, Y.; Xia, Y. *Nano Letters* **2004**, *4*, 2047-2050.

Webb, J. D.; Gedvilas, L. M.; Crandall, R. S.; Iwaniczko, E.; Nelson, B. P.; Mahan, A. H.; Reedy, R.; Matson, R. J. *Mater. Res. Soc. Symp. P.* **1999,** *557*, 311-316.

Weller, D.; Doerner, M. F., *Annual Review of Materials Science* **2000**, *30*, 611.

Wen, C. J.; Huggins, R. A. *J Solid State Chem* **1981,** *37* (3), 271-278.

Weydanz, W. J.; Wohlfahrt-Mehrens, M.; Huggins, R. A. *J. Power Sources* **1999**, *81*, 237.

Whittingham, M. S. *Science* **1976**, *192*, 1126.

Williamson, D. L. *Sol. Energ. Mat. Sol. C.* **2003**, *78*, 41-84.

Xiao, J.; Xu, W.; Wang, D. Y.; Choi, D. W.; Wang, W.; Li, X. L.; Graff, G. L.; Liu, J.; Zhang, J. G. *J Electrochem Soc* **2010,** *157* (10), A1047-A1051.

Xu, Y. H.; Yin, G. P.; Zuo, P. J. *Electrochim. Acta* **2008**, *54*, 341.

Yamamoto, Y.; Miura, T.; Suzuki, M.; Kawamura, N.; Miyagawa, H.; Nakamura, T.; Kobayashi, K.; Teranishi, T.; Hori, H. *Phys. Rev. Lett.* **2004**, *93*, 116801.

Yang, X. L.; Wen, Z. Y.; Huang, S. H.; Zhu, X. J.; Zhang, X. F. *Solid State Ionics* **2006,** *177* (26-32), 2807-2810.

Yao, Y.; McDowell, M. T.; Ryu, I.; Wu, H.; Liu, N. A.; Hu, L. B.; Nix, W. D.; Cui, Y. *Nano Letters* **2011**, *11*, 2949.

Yaws, C. L. *Handbook of Thermodynamic Properties*; Gulf Publishing Company: Houston, TX, 1996; Vol. 2.

Yoon, S.; Park, C. M.; Sohn, H. J. *Electrochemical and Solid State Letters* **2008**, *11*, A42.

Yu, H.; Buhro, W.E. *Adv. Mater*. **2003**, *15*, 416-420.

Yu, Y.; Gu, L.; Zhu, C. B.; Tsukimoto, S.; van Aken, P. A.; Maier, J. *Adv Mater* **2010,** *22* (20), 2247-+.

Yuan, J.; Liu, X.; Akbulut, O.; Hu, J.; Suib, S. L.; Kong, J.; Stellacci, F. *Nature Nanotech.* **2008**, *3*, 332.

Zhao, Y.; Zhu, J. J.; Hong, J. M.; Bian, N. S.; Chen, H. Y. *Eur J Inorg Chem* **2004,** (20), 4072-4080.

Zhou, G.; Li, L.; Li, G.H. *J. Appl. Phys.* **2011**, *109*, 114311-114318.

Zhou, S.; Liu, X. H.; Wang, D. W. *Nano Lett* **2010,** *10* (3), 860-863.

Zi, J.; Buscher, H.; Falter, C.; Ludwig, W.; Zhang, K. M.; Xie, X. D. *Appl. Phys. Lett*.

Vita

Justin Thomas Harris, the eldest of two children, was born in California on November 4, 1985, to Jeffrey and Debra Harris. After graduating as Valedictorian from Havelock High School in 2003, he enrolled at North Carolina State University. During his time there he performed Undergraduate Research under Dr. Jan Genzer before graduating summa cum laude in 2007 with dual B.S. degrees in Chemical Engineering and Chemistry. In 2007, he entered graduate school at the University of Texas at Austin in the Department of Chemical Engineering and pursued his Ph.D. under the supervision of Dr. Brian A. Korgel researching metallic nanoparticles, silicon and germanium nanostructures, and lithium ion battery anodes

Permanent address: 100 Barden Dr., Havelock, NC 28532

This dissertation was typed by the author.